이학박사학위논문

Interfacial engineering of organic light-emitting diodes with NaCl-incorporated anodic buffers

염화나트륨이 함유된 산화전극 완충층을 이용한 유기발광소자 계면엔지니어링

2014 년 2 월

서울대학교 대학원

화학부 물리화학전공

김정호

Ph. D Dissertation

Interfacial engineering of organic light-emitting diodes with NaCl-incorporated anodic buffers

Supervisor: Prof. Heon Kang

Major: Physical Chemistry

February 2014

By Jeongho Kim

Department of Chemistry

Graduate School of

Seoul National University

Abstract

Interfacial engineering of organic light-emitting diodes with NaCl-incorporated anodic buffers

Jeongho Kim
Department of Chemistry
The Graduate School
Seoul National University

Power efficiency and device stability of organic light-emitting diodes (OLEDs) are crucial factors for practical applications such as displays and lightings. Many efforts have been made to improve the external quantum efficiency of OLEDs in various aspects such as synthesis of phosphorescent materials and design of device architecture. In this thesis, the driving voltages and device lifetimes are improved through the interfacial engineering at anodic side by introducing a new interlayer of NaCl:organic composite. The mechanistic origins of the improved efficiency are investigated with ultraviolet photoemission spectroscopy and atomic force microscope. Because metal halides have been widely applied at the interface of cathode and organic layer, the application of NaCl-incorporated organic composite at anode/organic interface implies simpler fabrication of highly efficient OLEDs by introducing the same metal halide for both electron and hole injection efficiency.

In chapter I, the physics of OLED device is briefly introduced to give background information for understanding and analyzing the experimental results for the electrical characteristics of OLED devices. Power efficiency and device degradation mechanisms are mentioned based on the previous reports. Then, the electrode/organic interfacial engineering approaches for enhancing device performance are reviewed to support the importance of current study.

In chapter II, the effects of ultraviolet-ozone (UVO) and O_2-plasma surface treatments of indium tin oxide (ITO) anode surface are compared for OLED performance. While the OLED device with UVO-treated ITO anode shows a lower drive voltage than that of O_2-plasma treated ITO device during device operation, the lifetime is shorter. Through photoelectron emission spectroscopy measurements, decrease in tin (Sn) concentration was observed after the UVO treatment, which is attributed to the increased work function of ITO and to the decrease in surface conductivity, resulting in a lowered drive voltage. The shorter lifetime of the hole injection-efficient device is attributed to larger charge imbalance and more carbon contaminants.

In chapter III, we show that the composite buffer layers of N,N'-bis(naphthalene-1-yl)-N,N'-bis(phenyl)benzidine (NPB) and NaCl at the anode/organic interface are very effective for improving both hole injection efficiency and device stability. Furthermore, two maxima of current injection are observed with compositional variation of the buffer, implying that there exist multiple charge injection mechanisms such as tunneling effect via insulating property of NaCl and interfacial energetics.

In chapter IV, we suggest the mechanistic origins of the improved OLED

performance upon the use of a NaCl-containing organic interlayer between the ITO anode and NPB through the studies with ultraviolet photoelectron spectroscopy and atomic force microscopy. While a pure NaCl interlayer has a high hole-injection barrier (1.40 eV), the NPB:NaCl composite layer exhibits a substantially lower barrier (0.84 eV), which is comparable to the value at bare ITO/NPB interface. Furthermore, the wettability of the composite onto ITO is enhanced due to significant adhesive interactions of NaCl with both ITO and NPB (work-of-adhesions of 252 mJ/m^2 and 168 mJ/m^2, respectively), leading to effective electrical contacts. The two key factors of the plausible hole-injection barrier and the better wettability of the NPB:NaCl composite contribute to the improved hole injection efficiency and life time.

Keywords: OLEDs, NaCl:organic composite, hole injection efficiency, device life time, photoelectron spectroscopy, wettability.

Student number: 2007-30765

Contents

List of Figures and Tables

FIG. 1-4. Exciton recombination mechanisms in the host/dopant system: (a) charge-trapping model and (b) energy transfer model.

FIG. 1-5. (a) Light emission modes of a typical OLED device: dashed arrows denote the partial reflection on the cathode surface from non-radiative loss through light-absorption of the metal electrode. (b) Substrate mode coupled out deduced from the roughened surface of the substrate, (c) substrate mode coupled out through enhanced surface scattering from microspheres and (d) substrate mode coupled out through hemisphere micro-lenses [Ref. 43,44].

FIG. 1-6. (a) Micro-cavity effect; d is a effective cavity length, and z_1 and z_2 are distances from the emission zone to dominant reflective surfaces. Constructive interference condition for z is expressed with m, m' (m, m' = 0, 1, …) and λ (wavelength). As an example, a wave form is illustrated for the case of m = 1 and m' = 0. Micro-cavities with (b) semitransparent metal and reflective metal oxide, (c) capping layer, and (d) DBR 1-D photonic crystal structure; T, R, and DBR are the transparency, reflectivity, distributed Bragg reflector, reflectivity [Ref. 49,52,53].

FIG. 1-7. Schematic diagrams for device degradation mechanisms. (a) Concentrated electric field at protruded tips of the rough electrode surface, (b)

migration of metallic components of the electrodes, showing their accumulation in the emission zone and some species deposited on the opposite electrode, (c) aggregation/crystallization of an organic material at its interface with the anode, (d) oxidation of the organics or electrode surface at cathode/organic interface through up-taking oxygen or moisture, and (e) excess charges causing unstable chemical species in the electron and hole transport materials, respectively, or immobile charges causing stable effective exciton quenchers.

FIG. 1-8. Summary of the degradation factors and modes. Extrinsic factors have been solved through the encapsulation process and particle control in the clean room for fabrication except for the heat and electric field factors. The solutions for the intrinsic factors are intensively related to the interfacial engineering.

FIG. 1-9. Schematic electronic structures of the anodic side (a) without an interlayer between the anode and organic hole transport layer, (b) with a (semi-) conductive interlayer with a higher work function, (c) with an insulating interlayer under forward bias, and (d) with an interfacial dipole layer.

TABLE I-1. Prevailing conditions for each charge injection or transport mechanism in organic semiconductors. Prevailing or dominant conditions are relatively described. For example, with increasing temperature, both ICLC (injected-charge

limited current) and SCLC (space-charge limited current) increase. But ICLC increases at a slower rate, thus, ICLC becomes dominant or a limiting mechanism at high temperature. See text for the abbreviations and symbols.

TABLE I-2. Estimated underlying mechanisms related to the metal halides as electron injection buffer materials; origins of the HOMO level shift and gap-state formation of an adjacent electron transport material, and dissociation of the metal halides. Note: Al-deposition of Alq3 induces destructive interaction and no gap-state formation.

TABLE I-3. Estimated origins of hole-injection enhancement related to various hole injection layer (HIL) materials.

FIG. 2-1. (a) Chemical species of as-cleaned ITO surface, and (b) the chemical modification of the surface hydroxyl group through reduction with Ar^+ bombardment and oxidation with UVO or O_2 plasma treatment [Ref. 1 and 2] where M denotes In or Sn.

FIG. 2-2. Schematic diagram of OLED fabrication system. Vacuum systems only related to the deposition and UVO/plasma treatment are briefly depicted; Cryo, RP,

RV, HV, FV, and TMP denotes the Cryo-pump, rotary pump, roughing valve, high-vacuum valve, fore-line valve, and turbo-molecular pump, respectively. Positions of source materials in the deposition chamber are displayed in the lower part arrowed from the chamber; HTL, HIL, EML, and EIL means the hole transport layer, hole injection layer, emitting layer, and the electron injection layer, respectively.

FIG. 2-3. Chemical structure of (a) Alq3 and (b) NPB, (c) schematic of partial cross-sectional view of an OLED device (PI: abbreviation of polyimide), and (d) a sample (30 x 40 mm^2) with eight active patterns of an area of 2 x 2 mm^2.

FIG. 2-4. Electron energy diagrams for a (a) conductive or insulating (b) sample surface, and electron energy spectrometer, and variation of the kinetic energy of the photoelectron, which is generated by ultraviolet or X-ray irradiation of its energy *hv,* during the drift from the sample surface to the detector of the spectrometer. Here, for example, the photoelectron originating from 1*s* orbital is illustrated. E_{vac}, E_F, E_{1s}, ϕ_{sample}, $\phi_{\text{spec.}}$, E_b (1*s*), E_k (1*s*), E_k'(1*s*), and E_{ch} correspond to the vacuum level, Fermi level, electronic energy level of 1*s* orbital, work function of the sample, work function of the detector of the spectrometer, binding energy of the 1*s* orbital, kinetic energy of the photoelectron positioned at the sample surface, kinetic energy of the photoelectron positioned at the detector surface, and the surface charge energy, respectively. The kinetic energy of the photoelectron can be calculated with

the Einstein equation: $E_k' = h\nu - E_b - \phi_{spec.}$ for conductive samples and $E_k' = h\nu - E_b - \phi_{spec.} - E_{ch}$ for insulating surfaces.

FIG. 2-5. Electron energy diagram for a conductive sample biased negatively and the electron energy spectrometer (left) and the corresponding electron emission spectroscopy obtained through ultraviolet irradiation with energy $h\nu$ (right). E_{vac}, E_F, E_{SCO}, ϕ_{sample}, and $\phi_{spec.}$ correspond to the vacuum level, Fermi level, secondary cut-off level, work function of the sample, and work function of the detector of the spectrometer, respectively. $E_{k,\,F}'$, and $E_{k,\,SCO}'$ are the kinetic energies of the photoelectrons detected at the spectrometer, originating from the Fermi level and secondary cut- off level of the sample, respectively. E_{bias} is the applied bias energy.

FIG. 2-6. Current density-voltage and (b) luminance-current density characteristics of OLEDs with the ITO anodes treated with UVO and O_2 plasma.

FIG. 2-7. (a) Luminance and (b) voltage changes measured in time at a constant current density of 50 mA/cm^2, as a reflection of operational stabilities for the OLED devices.

FIG. 2-8. Full range of UPS spectra from the Fermi level to the secondary cutoff

regions of the ITOs surface-treated with UVO or O_2 plasma, and the no-treated ITO which is a wet-cleaned control sample before the surface treatments.

FIG. 2-9. Degree of charge balance vs. N_h/N_e ratio, where N_h and N_e are the number of holes and electrons reached the electroluminescent center, started from the anode and cathode, respectively.

FIG. 2-10. Plausible factors for generation of the interfacial dipoles [Ref. 31]. (a) charge transfer across the interface, (b) image force leading to the positive charging of the vacuum side, (c) Reduction of the electron tailing into vacuum through repulsive interaction between the electron clouds of the adsorbate and metallic surface, (d) rearrangements of the electron cloud and molecular/surface geometries through a strong chemical interaction, (e) formation of the interface states, and (f) adsorption of the polar molecules. E_{vac} corresponds to the vacuum level. Dipole moment is denoted as cross-bar/arrow.

FIG. 2-11. Schematic diagram of electronic structures of the ITO/NPB interfaces with various ITO surfaces: (*a*) as-cleaned ITO, (*b*) hydrocarbon-contaminated ITO, and (*c*) oxidized ITO. E_{vac}, E_F, M, and HC correspond to the vacuum level, Fermi level, metal elements (Sn or In) of ITO, and hydrocarbon contaminants, respectively.

FIG. 2-12. (a) Band structure of ITO based on the Ref. 21 and (b) schematic of hole injection barrier change from ITO to NPB with the downward shift of ITO Fermi level (E_F). E_c and E_v denote the conduction band edge and valence band edge, respectively.

FIG. 2-13. Schematic illustration of the NPB/ITO interface (a) before and (b) after de-lamination and their corresponding simple equivalent electric circuits under an applied constant current source.

FIG. 2-14. Cycle of device degradation based on the NPB aggregation- or crystallization-induced disruption of the ITO/NPB contact.

FIG. 2-15. Charge balance breakdown by heat.

FIG. 2-16. Schematic energy level diagram of the ITO/NPB/Alq3/LiF/Al based on the common vacuum level alignment (a) without applied bias and (*b*) with applied bias voltage exceeding the built-in voltage. E_{vac}, E_F, E_c, Φ_{bi}, qV', and qV correspond to the vacuum level, Fermi level, conduction band edge, built-in potential, effective potential, and applied potential between the electrodes,

respectively. Work functions of the ITO and Al, and LUMOs and HOMOs of organics are referenced to reported values [4, and therein]. Details in interface states and the energy levels of LiF are missed for brevity.

TABLE II-1. Summary of the driving voltages, luminance, current efficiencies, power efficiencies, external quantum efficiencies, and 60% lifetimes of devices A, B, and C, operated at a constant current density of 50 mA/cm^2.

TABLE II-2. Work function (ϕ) and atomic concentration for the ITOs treated with the UVO and O_2 plasma surface treatments. The values in ( ) are the ratios without carbon.

FIG. 3-1. Current density (J)-voltage (V) characteristics of OLEDs with different NPB:NaCl compositions [1:y wt %, y's of 0.5 (a), 2 (b), 8 (c), 15 (d), 30 (e), and 45 (f)] and various thicknesses of the composite buffer layer.

FIG. 3-2. Each J-V curve displayed along with different NPB:NaCl compositions from J-V characteristics of Fig. 3-1 for the different buffer layer thicknesses, 1 nm (a), 4 nm (b), 8 nm (c) and 16 (d).

FIG. 3-3. Current density versus NPB:NaCl concentration ratio at 5.6 V in the *J-V* curves of OLEDs for four different buffer layer thicknesses (a), of which the first peak is magnified in a corresponding *x*-axis for clear view (b).

FIG. 3-4. Current density (*J*)-voltage (*V*)-Luminance (*L*) characteristics for ITO/NPB:NaCl [1:*y* wt %, *y* = 2 (a) and *y* = 30 (b)] with various thickness values. Reference device architectures are ITO/NPB/Alq_3/LiF/Al (no-buffer layer) and ITO/CuPc (16 nm)/NPB/Alq_3/LiF/Al.

FIG. 3-5. Luminance-current density characteristics of OLEDs with NPB:NaCl [1:*y* wt %, *y* = 2 (a) and *y* = 30 (b)] anodic buffer layers in various thickness values. Reference device architectures are ITO/NPB/Alq_3/LiF/Al (no-buffer layer) and ITO/CuPc (16 nm)/NPB/Alq_3/LiF/Al.

FIG. 3-6. Current and power efficiency vs. current density for OLEDs with NPB:NaCl [1:*y* wt %, *y* = 2 (a) and *y* = 30 (b)] anodic buffer layers in various thickness values. Reference device architectures are ITO/NPB/Alq_3/LiF/Al (no-buffer layer) and ITO/CuPc (16 nm)/NPB/Alq_3/LiF/Al.

FIG. 3-7. Driving voltage, current efficiency, and power efficiency for OLEDs with

different thicknesses of NPB:NaCl [1:y wt %, y = 2 (a) and y = 30 (b)] anodic buffer layers. Reference device architectures are ITO/NPB/Alq_3/LiF/Al (no-buffer) and ITO/CuPc (16 nm)/NPB/Alq_3/LiF/Al (CuPc). The data in the upper- and lower-panels were obtained at a current density of 50 mA/cm^2 and at a luminance of 1000 nit, respectively.

FIG. 3-8. Driving voltage and luminance changes measured in time at a constant current density of 50 mA/cm^2, as a reflection of operational stabilities for OLED devices with 4 nm thickness of NPB:NaCl (1:y wt %, y = 15, 30, and 45) buffer layers. Reference device architectures are ITO/NPB/Alq_3/LiF/Al (no-buffer layer) and ITO/CuPc (16 nm)/NPB/Alq_3/LiF/Al.

TABLE III-1. Summary of the driving voltages, luminance, current efficiencies, power efficiencies, and 70% lifetimes of devices A, B, C, D), and E shown in Fig. 8, operated at a constant current density of 50 mA/cm^2. The life time values in parentheses are calculated at an initial luminance of 1000 nit by assuming the scalable law of Coulombic degradation ($L_0\tau$ = constant, where τ is lifetime).

FIG. 4-1. Schematic diagram of the photoelectron measurement system. The deposition chamber is attached to the analysis chamber for in-situ interface analysis and UVO surface treatment apparatus connected to the loading chamber for

cleaning the sample surfaces.

FIG. 4-2. UPS spectra collected near the Fermi level and secondary cutoff region during the step-by-step layer deposition of NPB on the ITO substrate. The HOMO features correspond mainly to the central biphenyl unit shown through the molecular orbital simulation shown in the right side of the UPS data whereas the LUMO levels are attributed to the naphthyl units of NPB (NPB was optimized using B3LYP density functional and 6-31G* basis set in DFT level).

FIG. 4-3(a). UPS spectra collected near the Fermi level and secondary cutoff region during the step-by-step layer deposition of NaCl, followed by NPB, on the ITO substrate.

FIG. 4-3(b). UPS spectra collected near the Fermi level and secondary cutoff region during the step-by-step layer deposition of NPB:NaCl, followed by NPB, on the ITO substrate.

FIG. 4-4. Changes of workfunction and ionization potential versus NPB (a), NPB/NaCl (b), and NPB:NaCl composite (c) layer thickness, respectively. HOMO edge shifts in the NPB (b), NPB/NaCl (d), and NPB:NaCl composite, respectively.

FIG. 4-5. Schematic energy diagram of (a) the adiabatic ionization energy and electron affinity (possible in the gas-phase molecule), (b) HOMO-LUMO gap measured with UPS/IPES (a distance between the centroids of the HOMO and LUMO peaks), (c) surface transport gap, (d) (bulk) transport gap, and (e) optical gap for the neutral excited molecule. P_- and P_+ denote the polarization energy during the generation of negative and positive polarons, respectively. E_{vac}, E_p^- and E_p^+ correspond to the vacuum level, negative polaron level, and positive polaron level, respectively.

FIG. 4-6. Variation of the polarization from the interface of metal/semiconductor to the film surface because of image charges of the metallic substrate during the photoionization process; (a) when only the image charge is effective, and when the ground-state (b) LUMO- and (c) HOMO-derived levels are pinned near the Fermi level of the metal by charge transfer. E_{vac} and E_F correspond to the vacuum level, and Fermi level, respectively. Measurable energy levels by UPS/IPES are represented by broad solid lines, and broad dashed lines (vacuum levels). $HOMO^{(UPS)}$ and $LUMO^{(IPES)}$ represent final states of N–1 and N+1 electrons, respectively, which would be achieved from onsets of the obtained spectra. HOMO and LUMO levels represent ground states of N electrons (dashed lines).

FIG. 4-7. Energy level diagram of the (a) NPB/ITO, (b) NPB/NaCl/ITO, and (c) NPB/NPB:NaCl/ITO. E_{vac}, E_F, eD, and Φ_h correspond to the vacuum level, Fermi level, interface dipole, and hole injection barrier, respectively.

FIG. 4-8. Schematic band diagram: (a) without and (b) with the NPB:NaCl buffer layer. Energy level changes with an applied bias are shown in the left part of the diagram. The shaded area denotes the approximate tunnelling barriers under the bias voltage.

FIG. 4-9. Schematic illustrations of (a) the film growth modes on the uniform surface free energy. A qualitative criterion for the growth modes is denoted with $\Delta\gamma$ ($\Delta\gamma = \gamma_{AB} + \gamma_A - \gamma_B$, where $\gamma_{A/B}$ is the interfacial free energy of A/B interface, γ_A is the surface free energy of adsorbate A, and γ_B is the surface free energy of substrate surface B), and (b) the work of adhesion ($W^A_{A/B}$) and spreading coefficient ($S_{A/B}$) of A on surface B.

FIG. 4-10. AFM images (2×2 μm^2) of (a) the bare ITO, and the 4 nm thickness of (b) NPB, (c) NaCl, and (d) NPB:NaCl , and the 8 nm thickness of (e) NPB, and (f) NPB:NaCl. The thin films were deposited on the O_2 plasma pretreated-ITO surfaces. Root-mean-square roughness (RMS) values in nm are 2.62, 5.13, 4.09, 4.17, 6.06, and 6.86 for (a), (b), (c), (d), (e), and (f), respectively.

FIG. 4-11. Schematic diagram of the wetting mechanism, and its analogy with an anchored boat.

FIG. 4-12. Raman spectra of the pure NPB film (50 nm) and NPB:NaCl composite thin films (100 nm, 1:x v/v, x = 1, 2, and 3) on the ITO substrates.

TABLE IV-1. Calculated values of interfacial free energy ($\gamma_{A/B}$), work of adhesion ($W^{A}_{A/B}$), and spreading coefficient ($S_{A/B}$) in mJ/m^2. Each surface free energy of NPB, NaCl, and ITO is referenced from literature, 31.1, 227, and 70.1 mJ/m^2, respectively [54-56].

Chapter I

Introduction

Organic light emitting diode (OLED) technology is very promising for flat panel display applications because of its many advantages such as wide viewing angle, fast response time, high brightness, extreme thinness, lightweight as well as potential mechanical flexibility for flexible displays compared to other display technologies, liquid crystal displays and plasma display panels. During the last decade, OLEDs have been studied both academically and industrially. However, power efficiency and device life time are still crucial issues for practical applications.

In addition to the development of robust organic materials with intrinsic high luminous efficiency and (electro-) chemical stability, further improvements are needed for lowering the driving voltage and enhancing the luminous efficiency and organic/electrode interfacial stability. The driving voltage and luminous efficiency are strongly affected by charge injection properties from an electrode to a charge transport layer. For effective electron injection, thin insulating materials such as LiF, NaCl, alkali metal acetates and sodium stearate have been introduced between cathodes and organic electron transport layers (ETLs), acting as electron injection layers (EILs) [1–7]. Several mechanistic reasons for the enhanced

electron injection with those insulating thin films have been suggested, mainly based on interfacial dipole formation, tunneling model, and alkali metal liberation from the halides forming low work function contact with relatively high work function cathode materials like Al, Mg:Ag, or Ca/Mg. On the other hand, many efforts have also been carried out to improve the hole injection from the indium tin oxide (ITO) anode to the hole transporting layers (HTLs). Various kinds of surface treatments for ITO have been tried to lower the hole injection energy barrier from the anode into the organic layers [8,9]. However, the surface treatment alone is not enough to overcome the barrier effectively. Therefore, an interlayer to improve hole injection, acting as hole injection layers (HILs), has been inserted between the ITO anode and the HTL, using various materials such as metals and metal oxides with high work functions, and organic materials (e.g., star-burst amines and copper phthalocyanine (CuPc)) [10–15]. Thus, materials for enhancing the charge injection interlayer have been selected, based on whether the interlayer is for hole injection or for electron injection.

In this thesis, enhancement and characterization of the hole injection properties at the HIL/ITO interface are mainly focused on. First, an introduction of the basic concepts on device physics in OLEDs and organic/electrode interfacial engineering are given in chapter I as well as briefly raising current issues in the rational design of OLED device architecture and practical applications. In chapter II, comparative investigations of ultraviolet-ozone (UVO) and O_2-plasma treatments, which are the most popularly adopted surface-pretreatments for cleaning and improved electronic properties of the ITO surface, show that hole

injection efficiency and device stability do not always have a direct correlation with each other. Chapter III discusses how enhancements for both hole injection efficiency and device lifetime can be achieved by introducing a halide/organic composite buffer layer between the ITO and HTL, whereas halides have been usually applied on the cathode sides and rarely on the anodic sides. Finally, in chapter IV, the mechanism behind the enhanced performance are partially clarified with a combined experimental approach using ultraviolet photoemission spectroscopy (UPS) and atomic force microscopy (AFM) which showed that both the interfacial electronic structure and surface wettability play significant roles in charge injection and device stability.

I-1. Device physics of OLEDs

A typical structure of OLEDs consists of a transparent ITO anode, an organic HTL, an EML, an ETL, and a metal cathode (e.g., LiF/Al) shown in Fig. 1(a). The total thickness of the organic layers is typically 100 to 200 nm. ITO has been widely used because of its transparency, low resistivity, and high work function (Φ) whereas alkaline or alkaline earth metals with low work function for cathode materials. One of the aromatic diamines, N,N'-(2-napthyl)-(1,1'-phenyl)-4,4'-diamine (NPB) has been used as a typical HTL material, because of its excellent hole injection and transport properties and good electron blocking capability at the ETL/EML boundary. Good HTL materials should satisfy one or more of the general requirements – morphological stability, small solid state ionization potential, high hole mobility, and small solid state electron affinity. On the other

hand, tris(quinolin-8-olato) aluminum (Alq3) is known to be one of the most robust ETL materials. The holes and electrons are injected into the HTL and ETL, respectively, under forward bias voltages, generating excitons in the EML. When the recombination of holes and electrons (annihilation of excitons) occurs, light emission (i.e., electroluminescence) appears.

Electroluminescence in organic solids involves several steps: charge injection, transport, generation of excitons, and exciton recombination to yield visible light output (Fig. 1(b)). The organic molecular energy levels are described in band-like fashion for simplicity, although the organic semiconductors are disordered without a well-defined band structure. Polaronic effects (i.e., a structural relaxation of energy levels of charged molecules or polarons) are also omitted. It is noteworthy that the necessity of different work function electrodes (i.e., high work function for the anode and lower work function for the cathode) to obtain double-carrier injection leads to the presence of non-trivial built-in potential (Φ_{bi}), more common term as a diffusion potential in p-n junctions, across the organic layer. The physical importance of Φ_{bi} is the reduction of the externally applied potential, qV (here, q and V are elementary charge and external voltage, respectively.); a net forward current is only achievable if qV exceeds Φ_{bi}, and thus, Φ_{bi} corresponds to the turn-on or flat-band voltage of the OLEDs [16]. Neglecting energy level shifts from interface dipoles, Φ_{bi} is equal to the contact-potential difference of the cathode and anode.

I-1-1. Charge injection and transport mechanisms

Organic materials used in OLEDs have wide energy band gaps of 2–3 eV or more, where the intrinsic thermally-generated carrier density is generally negligible (< 10^{10} cm^{-3}). They are not normally doped, and have large tails of density of states corresponding to a high density of localized states in amorphous phase, meaning that no charge carrier exists at room temperature and the materials can be considered more as insulators than as semiconductors, shown in Fig. 2(a). Because of the absence of extended delocalization, charge transport is typically not a coherent motion in energy bands but a stochastic motion through hopping between the localized states with a low carrier mobility (typically 10^{-5} – 1 cm^2/Vs for holes, and two orders of magnitude less for electrons) [17]. Unlike in inorganic semiconductors, impurities usually act as traps rather than charge carrier sources with some exceptions in polymer OLEDs [18]. Thus, much care for fabrication of OLEDs is necessary.

Charge carrier injection into an inorganic semiconductor is usually understandable with Richardson-Schottky (R-S) thermionic emission and Fowler-Nordheim (F-N) tunneling [19], shown in Fig. 2(b). The former is based on lowering of the image potential, in which an electron leaving a metallic electrode see an image force pulling it back, by the external field $E = V/d$ (namely, field-enhanced thermionic emission):

$$J_{R-S} = A^* T^2 \exp\left(-\frac{\left(\Phi_B - \beta_{R-S}\sqrt{E}\right)}{kT} \right), \qquad (1)$$

with the Richardson constant $A^* = 4\pi q m^* k^2/h^3 = 120(m^*/m_0)$ [$A/cm^2/K^2$], the zero-field injection barrier Φ_B, and $\beta_{R\text{-}S} = (q/4\pi\varepsilon\varepsilon_0)^{1/2}$ (q: elementary charge, m^*:

effective electron mass, m_0: free electron mass, k: Boltzmann's constant, h: Plank's constant, ε: relative dielectric constant, ε_0: vacuum permittivity). The F-N tunneling considers mere tunneling through a triangular barrier into continuum states without Coulombic effects:

$$J_{F-N} = \frac{A^* q^2 E^2}{\Phi_B \alpha^2 k^2} \exp\left(-\frac{2\alpha \Phi_B^{3/2}}{3qE} \right), \quad (2)$$

with $\alpha = 4\pi(2\ m^*)^{1/2}/h$. The R-S thermionic emission is usually appeared under an electric field less than 10^6 V/cm in the inorganic semiconductors with extended band states and large mean free path (or hopping distance) whereas the F-N tunneling apparently occurs at an higher electric filed larger than 10^7 V/cm. However, in organic semiconductors, additional random energy barrier caused by amorphous disorder (and short mean free path or hopping distance in the order of the molecular distances, ~1 nm) exists, and hence, causing an enhanced backflow of the injected carriers into the electrode. The charge carriers are speculated to be injected into the localized trap sites of the organic and transported by hopping mechanism between the organic molecules [20]. Based on the hopping system with the possibility of backflow, the injection process seems to qualitatively resemble R-S thermionic emission from the simulation data [21], while F-N injection has been shown to hold in PLED (polymer LED) at a high electric field [22].

Whereas charge carriers in small-molecule layers can only hop between the molecules adjacent to each other, the transport properties of conjugated polymers are a combination of motion through the delocalized orbital and hopping between the polymer chains. The mobility of carriers is normally field-dependent

because of a decreased hopping barrier under the electric filed. *J-V* characteristics of the organic semiconductors could be schematically displayed as shown in Fig. 2(c). At a reverse bias voltage, ohmic behavior of the current is deduced from the intrinsic carriers and unwanted leakage, which makes an upper limit of the intrinsic carrier density estimated. Because of the very low intrinsic carrier densities of the organic semiconductors used in OLEDs, the organic layers are usually fully depleted and will not show band bending effects. At an initial forward bias voltage, ohmic conduction ($J \sim V/d$) deduced from thermally generated free charge carriers is expected to dominate the injected charge contribution:

$$J_{ohmic} = \frac{q\mu_{n,p} n_0 V}{d}, \tag{3}$$

where q is the electronic charge, $\mu_{n,p}$ is the electron or hole mobility, n_0 is the thermally generated background free charge density, V is the applied voltage, and d is the ETL or HTL thickness. In the case of negligible n_0 compared to the injected charge density and negligible trapped charges, the current is limited by the space-charge present in the organic film, as previously formulated for the space-charge-limited current (SCLC, $J_{SCLC} \sim V^2/d^3$) in insulators (i.e., Mott-Gurney formula) [23]:

$$J_{SCL} = \frac{9\mu_n \varepsilon_0 \varepsilon_r V^2}{8d^3}. \tag{4}$$

Here, V is the applied voltage, ε_0 is the permittivity of the free space, and ε_r is the relative dielectric constant. Thus, the charge carriers would be transported by shallow-trap hopping SCLC process (namely, "*shallow-trap SCLC*"). The space

charge (here, for electron) will accumulate at the cathode/organic interface, leading to band-bending, as illustrated in Fig. 2(d). In comparison between the ohmic current ($\propto V/d$) and SCLC ($\propto V^2/d^3$), the former is expected to dominate at lower voltages and for thicker films shown in a previous report [20]. On the other hand, the carrier mobility is normally field-dependent in hopping system because the hopping barrier is lowered under the electric field. Thus, the SCLC can be sophisticated through the incorporation of the field dependence of the carrier mobility such as Poole-Frenkel (PF) mobility, $\mu(E) = \mu_0 \exp(\beta E^{1/2})$ [24], or a power law $\mu(E) = \mu_0 (E/E_0)^n$ [25]:

$$J_{SCL(PF)} \approx \frac{9\mu_0 \varepsilon_0 \varepsilon_r V^2}{8d^3} \exp\left(0.89\beta \left(\frac{V}{d} \right)^{1/2} \right) \tag{5}$$

and

$$J_{SCL(PL)} = \mu_0 \varepsilon_0 \varepsilon_r \frac{\left(1/(n+3)\right)^{n+2}}{E_0{}^n (n+2)} \frac{V^{n+2}}{d^{n+3}}, \tag{6}$$

respectively. Additionally, the temperature dependence of $\mu_0 = \mu_0(T)$ could be also considered for more consistent device model [16].

The SCLC theory is extended to include the effects of charges trapped in either shallow or deep levels, leading to the trapped-charge-limited current (TCLC) concept (i.e., "*extended SCLC*", or for convenience, "*deep-trap SCLC*"). With an increase in the bias voltage, the TCLC becomes dominant through filling the traps [20]. The trap energies (here, given for *electrons*) are frequently assumed to be distributed exponentially as follows [23]:

$$N_t(E) = \frac{N_t}{kT_t}\exp\left(\frac{E - E_{LUMO}}{kT_t}\right), \tag{7}$$

where N_t is the total trap density, k is the Boltzmann's constant, T_t is the characteristic temperature (i.e., $T_t = E_t/k$, where E_t is the characteristic trap or decay energy), and E_{LUMO} is the LUMO band energy. The filling of the traps below the quasi-Fermi level (i.e., in a thermodynamically non-equilibrium condition) results in the current governed by the density and the trap energy distribution [26]. At the initial low voltages in TCLC, from charge-capture in traps, the carrier mobility is very low while, at relatively high voltages, the increased charge injection reduces the empty traps and causes a rapid increase in the effective carrier mobility, hence rapid and power-law increase in current ($J_{\mathrm{TCL}} \sim \frac{V^{m+1}}{d^{2m+1}}$):

$$J_{TCL} = N_{LUMO}\mu_n q^{1-m}\left(\frac{\varepsilon_0\varepsilon_r m}{N_t(m+1)}\right)^m\left(\frac{2m+1}{m+1}\right)^{m+1}\frac{V^{m+1}}{d^{2m+1}} \tag{8}$$

where N_{LUMO} is the density of states in the LUMO band and $m=T_t/T$. Thus, based on the value, m, obtained from the experimental J-V characteristics with fits to the power law $J \propto V^{m+1}$, one can evaluate the trap energy (i.e., trap depth) and density. Here, the temperature dependence of the electron mobility also must be considered. Depending on the nature of conduction between the deep trapping events, the conduction in a (narrow) band follows a temperature dependence of $\mu_n(T) \approx T^{-k}$, where k varies from 0 to 3 [27]. On the other hand, hopping conductivity follows $\mu_n(T) \approx \exp(-\Delta E_{ac}/kT)$, where ΔE_{ac} is the activation energy [26]. In Fig. 2(d), the trapped charge density is expressed upon the exponential distribution of traps,

showing a decreasing charge-density with distance from the cathode and corresponding electron quasi-Fermi level in a dotted line.

The charge injected into the organic layer produces an electric field and the total local field at any point is a summation of both internally and externally applied fields. At sufficiently high voltages (i.e., high charge injection levels thus, no empty traps), the internal electric field would almost cancel the applied electric field at the injection point of the electrode/organic interface from trap-filled limit, and the injection contact would becomes ohmic-like. Thus, the current is limited by the space-charge present in the organic film again, following the SCLC formulation ($J \sim V^2/d^3$), namely "*trap-filled SCLC*". The trap-free (or trap-filled) SCLC ranks a maximum possible unipolar current region shown in Fig. 2(c). Although the high current region is frequently not so practically applicable to OLED products due to rapid degradation of the OLED devices, the trap-filled SCLC can be easily reached with thin (i.e., less than about 100 nm) organic films through the filling of all traps already at a relatively small voltage above the built-in voltage [16].

Because the charge current flows serially from the injection contact to the organic bulk, ICLC (injected-charge-limited current, i.e., injection mechanism from the contact) and SCLC (i.e., charge transport in the bulk) can be a bottleneck (i.e., a limiting factor or a dominant current mechanism) against each other. Here, ohmic current induced from the intrinsic charge carrier in the organic bulk is not considered because of its non-contribution to the light emission. At zero-field contact barriers higher than 0.25–0.30 eV, the current in organic devices is normally believed to be dominant (i.e., limited) by ICLC [28] and expected to be

by SCLC at lower barriers. However, rather counter intuitively, Arkhipov *et al.* showed a comparative investigation of hopping ICLC vs. hopping SCLC that the former is a limiting current at higher temperatures even if the injection barrier is relatively low, because of much steeper increase in SCLC with the increase in temperature, and further, the injection barrier as high as 1 eV can be an ohmic contact at low temperatures providing conditions for the hopping SCLC. Therefore, R-S thermionic emission is expected to be a dominant (i.e., limiting) current and well-fit to the experimental data at a high temperature and a low applied field while F-N tunneling is a limiting current at a high temperature and a high applied field, whereas the SCLC is a limiting factor at a low temperature even if the injection barrier is relatively high, as summarized in Table I. However, Burrows *et al.* argued that the injection mechanisms (i.e., R-S thermionic emission and F-N tunneling) do not fit to their experimental results [20]. One more criterion to discriminate between the ICLC and SCLC (including TCLC) is thickness dependence of the *J-V* characteristics because the pure ICLC could be expressed as a function of the electric field alone without an explicit thickness dependence while the SCLC obeys a power law of $J \propto V^{m+1}/d^{2m+1} = E^{m+1}/d^{m}$ in the case of trap-charge limited transport, or $J \propto V^2/d^3 = E^2/d$ for trap-free transport. For example, in thin NPB (d < 100 nm)/ITO anode system, ICLC is the current limiting factor, whereas thicker films display SCLC [16]. In the case of Alq3/Al cathode, both ICLC and SCLC are working depending on the film thickness of Alq3 (qualitatively similar to the case of NPB), but mostly with the dominance of SCLC. By introducing LiF between Alq3and Al, ohmic contact can be achieved and SCLC was demonstrated

for thick Alq3 (d > 200 nm) [29], whereas a Mg:Ag cathode leads to the R-S type ICLC behavior [30]. More practically, in double-carrier injection system, concomitant space-charge neutralization increases the demand for carriers to be supplied by the contact, causing more contribution of ICLC in the bipolar current.

As described above, *I-V* characteristics are significantly dependent on the field and temperature dependent charge carrier mobility. Aromatic amines like TPD and NPB or its derivatives show a hole mobility of around 10^{-3} cm^2/Vs at room temperature with a very weak dependence on the electric field [31]. For Alq3, the electron mobility is much lower (~10^{-5} cm^2/Vs) and displays a large increase with the electric field, as typically observed for dispersive hopping transport, which also makes the electron mobility dependent on experimental parameters like thickness of the sample. Hole mobility of Alq3 is still much lower by almost three orders of magnitude at low fields but higher dependence on the electric field, even if hole transport is non-dispersive, makes the mobility difference of both charge carrier types smaller with the increase in the electric field [16,32]. Thus, the hole transport in Alq3 is not generally negligible in OLEDs.

On the other hand, the efficiency of OLEDs has often been successfully interpreted in the context of energy band conduction mechanism rather than hopping [33]. Therefore, the mechanisms of charge transport in organic materials of OLEDs lie somewhere between the extremes of stochastic hopping motion and typical semiconductor-like band motion.

I-1-2. Exciton formation and recombination

Electron-hole formation in organic materials is thought to follow the Langevin bimolecular recombination process:

$$R = \gamma n_e n_p, \tag{9}$$

and

$$\gamma = \frac{e(\mu_n + \mu_p)}{\varepsilon}, \tag{10}$$

where R is the recombination current from the bipolar equilibrium carrier densities n_e and n_p with mobilities μ_n and μ_p, and γ is the Langevin recombination coefficient. The Langevin model is valid if the average mean free path (i.e., hopping distance) of the carrier is much less than the Coulombic capture of one carrier by the other. This condition is generally satisfied in low mobility materials such as conjugated polymers and small molecules where the mean free path (~1 nm), is much less than the capture radius (larger than 10 nm at room temperature) [28].

The formed excitons will be either singlet or triplet states, where the singlets can relax radiatively, whereas for the triplet states the emission is forbidden. According to the simple spin statistics (i.e., spin-independent process), the ratio of singlets to triplets is 1:3 shown in Fig. 3(a). An excited state consists of two electrons, and for each electron the spin state is up or down with precession in or out of phase. According to the Pauli's exclusion principle, the triplet states (i.e., symmetric spins) keep the two electrons away from each other, reducing the electron-electron repulsion energy, whereas the singlet states have antisymmetric spins thus, can have the same position in space, resulting in a large electron-electron Coulombic repulsion. Therefore, the triplets are at a lower energy than the

singlets. The single-triplet splitting ($\Delta E_{S\text{-}T}$) is inversely proportional to orbital size, because the electrons will be further apart (e.g., $\Delta E_{S\text{-}T}$: 1.5, 1.3 and 1.1 eV for anthracene, tetracene, and pentacene, respectively), whereas the splitting is proportional to orbital overlap [34]. For a wide range of organics used in OLEDs, the triplet state is found to be ~0.7 eV below the singlet state [35,36].

For small molecules, the spin-independent singlet ratio seems to be applicable for the radiative recombination, limiting the maximum internal quantum efficiency to 0.25. However, for polymer-based materials the ratio can vary significantly greater than 0.5 although a clear origin is yet to be agreed. Recently, Chihaya Adachi (Kyushu University) et al. with rare-metal free emitter of dicyanobenzene derivatives suggest that new emission paths on the Perrin-Jablonski diagram, namely thermally activated delayed fluorescence (E-type) and triplet-triplet annihilation (P-type), can be the origin of higher internal quantum yield through fluorescent harvesting (Fig. 3(b)). Thus, by using both the singlet and triplet excitons, the internal quantum efficiency can be increased up to 1 through the phosphorescence (namely, phosphorescent harvesting) or delayed fluorescence (fluorescent harvesting).

The phosphorescent emission can occur through interactions with impurities or defects via spin-flip process and is generally orders of magnitude smaller than fluorescence. However, the phosphorescence can be enhanced by incorporating heavy mass element organo-metallic compounds through the increase in spin-orbit coupling hence enhanced spin-flip process. Generally, the phosphorescent materials are adopted as guest dopants to inhibit the triplet-triplet

annihilation. Exciton formation at the dopant material occurs through charge trapping model (Fig. 4(a)), where the host materials act as charge transport media, and energy transfer model from the host to the guest dopant. In the energy transfer model, an exciton in a host material can transfer to the phosphorescent dopant through radiative or non-radiative energy transfer process. The former occurs through radiative deactivation of a donor host and reabsorption of the emitted light by an acceptor (i.e., phosphorescent guest). In the presence of phosphorescent guest in OLED devices, two types of non-radiative process (Fig. 4(b)), Förster and Dexter transfer, seem to be dominant. Förster transfer is a resonant dipole-dipole coupling (i.e., Coulombic) and can occur very fast ($< 10^{-9}$ s) between molecular entities separated by a distance of ~3 – 10 nm, which is a typical mechanism for singlet-singlet transitions (i.e., singlet exciton transport) shown in Fig. 4(b). Dexter transfer occurs through diffusion of excitons from donor to acceptor (in other words, electron exchange between donor and acceptor under a restriction of wave function overlap) thus, it is relatively short range (~0.5 – 2 nm) transfer and is allowed for both single-singlet and triplet-triplet transitions (namely, a mechanism for both singlet and triplet exciton transport). Therefore, singlets formed in host can transfer to the guest through either Förster or Dexter process while triplets transfer mainly through the Dexter process, shown in the right part of Fig. 4(b).

For example, porphyrin based materials like PtOEP (platinum octaethyl porphyrin) generates red phosphorescent excitons, which are localized on organic ligands. The triplet excitons located in the ligands can have spin-flip process through effective spin-orbit coupling induced from strong magnetic field generated

by the heavy transition metal, causing phosphorescence. However, because of relatively long lifetime of the triplet excitons (> 10 μs), a large buildup of the triplet density at moderate injection levels enhances the triplet-triplet annihilation which leads to a rapid reduction in current efficiency [37]. On the other hand, $Ir(ppy)_3$ (Iridium tris (2-phenylpyridine)) is a typical green phosphorescent with metal-to-ligand charge transfer (MLCT) exciton type. Because of its shorter lifetime (~1 μs), the triplet-triplet annihilation reduces, hence the efficiency increases at higher brightness or higher injection levels [38]. In the case of blue phosphorescence (~2.9 eV), the band gaps of both host and dopant materials need to correspond to an energy in UV from large singlet-triplet splitting. Furthermore, the band gap is related to stability and charge injection/transport in the materials. Those collective requirements are yet to be met for practical applications of the blue phosphorescent materials although some of red or green phosphorescent materials are currently adopted in OLED display products with the increase in current efficiency.

One the other hand, the non-radiative exciton energy transfer mechanisms are not always efficiency-friendly. A metal electrode in contact with a thin fluorescent film can cause a coupling between the excitons and the plasmon modes of the two-dimensional electron gas present at the interface, or a near-field interaction of the excitons (namely, radiative dipoles) with the metallic electrode. Those interactions results in non-radiative recombination of the excitions through energy-transferring to the electrons in the electrode metal [39,40]. Because the ITO anode does not quench the fluorescence very efficiently, the efficiency in an OLED

can be improved by tailoring the recombination zone far away from the cathode and near the position of maximum constructive interference [41].

I-1-3. Output coupling

The external quantum efficiency (η_{ext}: emitted photons/injected charges) of OLED is given by the following fundamental equation:

$$\eta_{ext} = \frac{N_{ph}}{N_e} = \frac{\pi \int (\lambda / hc) F(\lambda) d\lambda}{J / e} \tag{11}$$

where λ is the wavelength, $F(\lambda)$ the radiance of each wavelength [$Wsr^{-1}m^{-2}nm^{-1}$], h the Plank's constant, c the light velocity, J the current density, and e the elementary electric charge. However, for practical design of OLED devices, the extraction of light generated inside the device to the required external environment must be considered as a major restriction on the current efficiency. The external quantum efficiency is generally described as following equation:

$$\begin{aligned} \eta_{ext} &= \gamma \times r_{st} \times q \times \eta_{coupling} \\ &= \eta_{int} \times \eta_{coupling}, \end{aligned} \tag{12}$$

where γ is charge balance between the numbers of electrons and holes injected into the organic layer, r_{st} is a ratio of singlets to triplets, q is a ratio of radiative decays to non-radiative decays (e.g., internal conversion, intersystem crossing, energy transfer to the metallic electrode through non-radiative dipole-metal transfer and excitation of surface plasmons) and finally $\eta_{coupling}$ is output coupling referring to the extraction of light. Especially, the terms except $\eta_{coupling}$ is referred as internal quantum efficiency ($\eta_{int} = \gamma \times r_{st} \times q$). Because the terms affecting the internal

quantum efficiency are implicitly described above, here, a brief expression of the models to estimate the output coupling efficacy and illustrations about the methods to enhance the efficiency are provided.

In the assumption of no optical losses or interference (micro-cavity) and perfect reflection at the metal interface, the output coupling efficiency is simply given by the often-cited relationship [41-43],

$$\eta_{\text{coupling}} \sim 1/(2n^2) \tag{13}$$

for isotropic dipole emission in small molecule-based OLEDs and

$$\eta_{\text{coupling}} \sim 3/(4n^2) \tag{14}$$

for preferential in-plane dipole emission in polymer-based OLEDs where n is refractive index of organic layer. With optimized constructive interference of the emitted reflected light and optimized location of emission zone away over 20 nm from the metal cathode, the output efficiency is significantly enhanced [41], following the eq. 14 for the isotropic dipole emission and

$$\eta_{\text{coupling}} \sim 6/(5n^2) \tag{15}$$

for the in-plane dipole emission.

A typical OLED device consists of the metallic cathode, organic layer, ITO anode and the glass substrate. The refractive index of the organic layer (~1.6 – 2.0) and the ITO (~1.6 – 2.0) is larger than that of the glass (~1.5). Thus, three main light-emission modes are generated, shown in Fig. 5 (a): surface-emitting external modes, substrate waveguide modes, and organic/ITO modes [44]. The substrate waveguide mode contributes to edge emission which is strongly TM polarized (i.e., *p* polarization), narrowed, and red-shifted with respect to the normal

surface emission mode while the organic/ITO waveguide modes is virtually eliminated due to absorption by the underlying metallic cathode [40]. A more rigorous model considers the emitter as a radiating dipole in an optical micro-cavity (namely, a structure with two highly reflective interfaces). The interaction of the dipole with the micro-cavity modes determines the electric fields, which in turn affects the radiative lifespan, altering the ratio of the radiative and non-radiative processes thereby changing the device efficiency [45]. Inclusion of the microcavity effects based on classical electrodynamics or quantum mechanics suggests that the output coupling is significantly higher than predicted by the simple mode mentioned above and that up to 50% coupling can be obtained under an optimized condition.

The techniques enhancing output coupling can be divided into two main streams: reduction of the total internal reflection at the glass/air interface, and modification of the relative number of three types of modes (i.e., external mode, substrate mode, and organic/ITO mode). The former can be achieved through substrate surface modification like roughening, attaching silica microspheres or micro-lenses. The roughening or patterning of the surface with silica or polystyrene spheres enables some of the light that would normally be totally internally reflected to be scattered out from the surface as shown in Fig 5(b) and (c) [46,47]. Especially, the two-dimensionally (2D) ordered microsphere array will cause generation of a photonic band structure and its corresponding optical diffraction of a 2D photonic crystal (i.e., periodically varying dielectric constants in the scale of optical wavelength, affecting the propagation of electromagnetic waves) [48]. The

microspheres in sub-micrometer size which is corresponded with visible frequency cause Mie scattering showing high forward scattering rather than backward scattering (cf. Rayleigh scattering for small particles) and the array also shows resonant excitation of photonic bands coupled with the incident visible light. Thus, although large amounts of light within the substrate modes are effectively scattered out with the microsphere array attached to the glass substrate, the emitted colors are dependent on observation angle, limiting direct applications for image viewing, e.g., for OLED displays [47]. Micro-lens array designed such that the emission occurs at the center of the sphere means that rays impinging on the glass/air interface will be at normal incidence and hence, escape the substrate (Fig. 5(d)) [43]. Although the color change issue could be almost cleared, the substrate and lens sheet might be thin (< ~0.5 mm) to avoid image blurring because the effective pixel size on the out-coupling surface increases with the increase in substrate/lens thickness, leading to the overlap of the light emitted from adjacent pixels hence a blurred image [49]. The other major loss due to the organic/ITO confined waveguide modes can be simply reduced by decreasing the organic/ITO thickness. For example, simple reduction of ITO thickness from 200 to 100 nm can dramatically reduce the waveguide modes confined to the organic/ITO layer and increase the output coupling as high as 52% [50].

On the other hand, OLED devices can be considered as an optical micro-cavity which is a structure with one or more spatial dimensions on the order of an optical wave length, changing photon density of states and spontaneous emission properties of an optically active material placed in such a cavity [51]. The

modifications of spontaneous emission include a change in spectral line width and radiation pattern, a directional emission enhancement, and a slight change of spontaneous emission lifetime hence the quantum efficiency. By tuning the cavity resonance to wavelengths near the peak (non-cavity) electroluminescence, the amount of escaped light can increase. To maximize output coupling efficiency, the exciton must be at the anti-node of the electric field (i.e., a radiation mode) and radiation modes have nodes near to the metal electrode while the distance between the exciton and the dominant reflective anodic interface (e.g., ITO/glass) should be a multiple of half wavelength for maximum constructive interference of electric fields at the point of the exciton (reflection at the ITO/glass without phase change) [40,50], shown in Fig. 6(a). For stronger micro-cavity effect to enhance the out-coupling efficiency, semitransparent metals/reflective metal oxides [52], semitransparent dielectric capping layers like ZnSe [53], or Brag mirrors such as a quarter wave dielectric stack (1-D photonic crystal) using TiO_2, SiO_2, or SiN_x [49] have been adopted as each schematically illustrated in Fig. 6(b) – (d). However, a blue shift or blue-and-then-red shift in the spectral peak with increasing angular displacement from the normal has been observed with non-Lambertian distribution of luminance [49,52], although a shorter cavity, e.g., an optical thickness of 1 half-wavelength, leads to a reduction in the angle and wavelength dependence of the emission [54]. Recently, the color variation under viewing angle due to the micro-cavity was reported to be remarkably suppressed by micro-lens arrays, which were randomly distributed to avoid undesirable diffraction patterns over the OLED micro-cavity formed by a stack of SiO_2 and SiN_x layer (1-D photonic crystal) and a

metal cathode [55].

I-2. Issues for practical applications of OLEDs

Recently, OLEDs have been popularly adopted as one of the main display technologies in mobile devices due to their many advantages such as wider color gamut, and thin/light-weight form factor on a plastic substrate, compared to the other competitive display, LCD. However power consumption of OLEDs still seems to be inferior to that of LCD at a same luminance although OLEDs can give high perceived brightness at lower luminance values according to the Helmholtz-Kohlrausch effect because of their higher color gamut. Moreover, the irreversible image-sticking (or residual-image) phenomenon due to degradation of the organic materials in OLEDs has been notorious to inhibit applicability of OLEDs to larger-area display products such as notebook or desk-top PC monitors. Therefore, both high power efficiency and device lifetime enhancement are critical for further expanded applications of OLEDs.

I-2-1. Power efficiency

Power consumption of the OLED device is still very challenging issue to compete with other lighting or display technologies such as inorganic LED or LED-back-lighted LCD. Assuming a Lambertian angular distribution of emitted light, the luminous power efficiency of a display or an area light source (η_p expressed in the unit lm/W) is related to its current efficiency (η_c expressed in the unit cd/A) as

$$\eta_p = \pi \eta_c / V_D, \quad (16)$$

where V_D is the drive voltage of the OLED. η_c is almost constant over a wide range of current density, or increases very slightly with the increase in drive voltage, so that η_p decreases as the current level or drive voltage increases.

The higher current injection is expected to affect adversely the current efficiency by increasing the recombination region and exciton diffusion length (typically ~20 nm for Alq3 [20]), causing a shorter average distance between a radiative dipole and the metal electrode hence suppressing the dipole radiation [40]. Especially, in phosphorescent OLED devices, the current efficiency is further decreased due to higher triplet-triplet annihilation process in high injection levels (i.e., high current density) with short period.

The voltage dependency of power consumption is critical in passive matrix (PM) type for addressing OLED pixels. Because the device is operated in a pulsed mode with low duty cycle and a high peak brightness to give the desired average luminance, the current level would be very high depending on the number of scan lines for one frame of display, correspondingly, resulting in an increase in the drive voltage, and hence, lowering the power efficiency. For example, in a display of monochrome quarter VGA (qVGA) resolution, there are 240 scan lines, so that the duty cycle for each frame would be *ca.* 1/240. Thus, when turned on, the current density of the device would be 240 times higher than that of a device operated with dc for the same average luminance [56], resulting in an increase in the drive voltage by at least a factor of two, and hence, leading to a reduction in the power efficiency and increase in the power consumption by an equal amount. An

active matrix (AM) type of OLED addressing overwhelms the power efficiency of PM-OLED, but AM-OLED displays still seem to be (slightly) inferior to that of the competitive display technology, TFT-LCD, in recent years.

Although the OLED is self-emitting display technology without other (back-)light sources, a circular polarizer which decrease the original OLED light output amount down to ~40% is put on the encapsulating layer of OLED display to reduce reflected light from metal cathode, and hence to improve contrast. Moreover, a full color display solution of white emitters followed by RGB color filters or a blue common layer followed by color conversion layers for red and green inherently further decreases power efficiencies.

I-2-2. OLED degradation

In industrial applications such as display and lighting, differential degradation between the three primary colors and sticking image effects are among hot issues. Several mechanisms have been suggested to explain the device degradation upon operation. Crystallization or inter-diffusion of organic layers has been widely considered to be one of the most plausible causes for deterioration of OLEDs [57-59]. However, as reported by complex mechanistic origins in various conditions even without consensus, an understanding of the degradation process is still remained to be complete. For example, storage life time was reported to be enhanced by replacing amorphous α-naphthylphenylbiphenyl diamine (NPB) layer with a partially crystalline NPB layer as a hole transport material [60]. Through Fig. 9, the origins are categorized along with similar fundamental origins, sometimes

with slight correlation between each other, e.g., metal migration and roughness under electrical stress.

Roughened surface (esp., sharp points) of electrodes can cause strongly concentrated local electric fields, illustrated in Fig. 7(a), causing highly intensive current flow. Thus, enhanced local (or non-uniform) luminescence and Joule-heating lead to instability of the organic current paths, e.g., through organic inter-diffusion hence lowered electrical conductivity [59], until the organic materials break down or carbonize, which may lead to short and/or open circuits, in addition to the generation of volatile species including carbonyl groups (a luminescence quencher in Polymer OLED [61]) with occurrence of the electrical short [62,63]. Furthermore, once localized electrical shorts occur, the intrinsic organic materials in the localized intensive current path can be also volatile due to local high temperature of larger than 200 °C [64], which might be a cause of de-lamination of electrodes, although NPB and Alq3 on ITO surface are reported to be thermally stable at or above 150 °C [65]. The concentrated electric field can facilitate the metal migration (more explained later): the local high temperature by Joule heating could melt the organic layers and hence, forms an ion channel for metal ions (e.g., In) field-emitted from electrode spike tips to migrate according to the electric field and eventually arrive at the opposite electrode [66], and the reverse is also true that initial metal migration caused by the prolonged electrical stress can increase the roughness of the organic/electrode interface, inducing the intensive local field. In any case, stabilizing and smoothing the organic/electrode interface is one way to minimize the device degradation.

Electrodes themselves can contaminate the inner organic layers with their metallic elements, resulting in deterioration of the device performance through exciton-quenching or forming a non-radiative center (band-gap states) [67] shown in Fig. 7 (b). According to the mobile ion model [68], the positive and negative ions, of which sources could be electrodes or other contaminants incorporated during fabrication, accumulate toward the cathode and anode, respectively, over the operating time, causing the increase in drive voltage from the increase in internal polarization field (i.e., opposite to the applied bias field). Indium (In) has been reported to not only diffuse from anode to cathode (prior to operation) in polymer LED [69], but also migrate under electric filed in small molecule OLEDs [70], indicating that In is highly diffusive, which were confirmed by various surface analysis techniques such as X-ray photoelectron spectroscopy (XPS) depth profiling, Rutherford backscattering spectroscopy (RBS), and secondary ion mass spectroscopy (SIMS). After removal of the organic films, the ITO surface is found to be damaged to an extent of topographic change from the In-depletion, correlated with the electrical stress time [71]. The presence of In in the emission zone was detrimental to electroluminescence efficiency owing to its exciton-quenching effect, while In in the electron transport layer (Alq3) and hole transport layer (NPB) increased the operation voltage. The upper shift of drive voltage points to the role of In impurity in forming hole traps or in increasing internal polarization field. Along with the trapping model, the hole and electron mobility are reduced in the charge transport layers for hole and electron, respectively, which is similar to the mechanism for the shift in current density versus voltage (*J-V*) characteristics to

higher voltages in the case of rubrene-doped NPB hole transport layer [72,73], while the mobile ion model explains the increase in drive voltage is ascribed to the increased polarization field through the accumulation of In cations toward cathode side. The diffusive In can further contaminate the opposite cathode/organic interface across the emission zone, causing an increase in electron injection barrier, hence again drive voltage might increase. (Once In cations have been removed from the ITO electrode surface, the remaining O^{2-} anions will be reduced in the form of O_2 or O_2^- due to arriving holes.) In this view, the remedy against the degradation is to reduce the field gradient near the ITO surface or ITO/organic interface by introducing a hole injection buffer layers such as conducting polymer or forming ladder (i.e., stair-case) type of hole injection electronic structure near the interface. Li was also reported to diffuse rapidly into organic materials from a Li/Al cathode, and create non-radiative decay centers, leading to the shortened device lifetime [74]. Mg in Mg:Ag/Alq3 cathodic interface penetrates slightly into 2–3 nm of Alq3 layer (from SIMS results), partially doping the Alq3 electron transport layer [70]. The Mg-doped electron transport layer caused an increase in drive voltage possibly because of Mg-doping induced electron-trap sites. Aluminum (Al) in Al/Alq3 also diffuses into adjacent organic layers like In but to a lesser extent in a strong correlation with Alq3 photoluminescence quenching [75], and tin (Sn) is known to form continuous metallic layers directly (i.e., not so significantly diffusive) [76]. Oxygen was also reported to be pulled out of the ITO by holes in a neighboring space charge layer [77]. Polymer OLEDs based on PPV (Poly(phenylene vinylene) are known to be susceptible to photo-oxidation which

generates carbonyl species (e.g., aromatic aldehydes) as a luminescence quencher and increases the operating voltage by lowering charge carrier mobility from the loss of conjugation of polymer. During the oxidative degradation of polymer, ITO anode was suggested to be the source of oxygen. However, oxygen diffusion by pulling of adjacent holes should be only operative less than a few molecular layers from ITO, even against the applied field gradient and hence, degradation throughout the organic layers is not plausible [71].

Crystallization of organic layers has been still considered as a representative failure mode. For the device architecture of ITO/NPB anode interface and Alq3/Al cathode interface, crystallization of both NPB and Alq3 by Joule heat during operation was confirmed by high resolution x-ray diffraction (HRXRD) and grazing-incidence x-ray diffraction (GIXD) [78]. Especially, NPB is predominantly crystallized due to its lower glass transition temperature (T_g: 100 and 175 °C for NPB and Alq3, respectively [79,80]), shown in Fig 7(c), thus the volume of organic materials expands, inducing the de-lamination between the Al and Alq3 layer [78]. With the prolonged electrical stress, the protrusions expanded more and more, finally leading to the formation of hollows (e.g., dark spots) via bursting of protrusions. More directly, the crystallization of HTL would disrupt and reduce the contact between layers, e.g., weak adhesion of HTL to the adjacent ITO anode, sometimes, allowing oxygen and water vapor to penetrate between the layers in the device, which were speculated from secondary electron microscopy (SEM) and energy-dispersive X-ray (EDX) analyses [81]. On the other hand, the local aggregation of molecules pre-existed as an amorphous phase might form hole

or electron traps and a part of the injected charge-carriers builds up a space charge, which might cause an excess charges at/near light emission zone, leading to non-radiative destruction of excitons through interaction with the excess incoming charges [82-84].

The moisture and oxygen seem to be crucial factors for degradation of organic/cathode interface, illustrated in Fig. 7 (d), entering through a pinhole in the metallic cathode and reacts at the metal/organic interface, hence causing the oxidation of the metal or organic species and finally forming the dark spots [85]. For Mg/Alq3, the oxidation process may involve reduced Alq3 molecules, which are generated near the cathode/Alq3 interface during thermal deposition of Mg [86]. The formed Alq3 anion is known to facilitate electron injection into the organic bulk through its interfacial mid-gap states [87]. Thus the oxidation of negatively charged Alq3 molecules adversely affects the electron injection. Mg would be converted to oxidized insulating species such as MgO and $Mg(OH)_2$, forming a electron injection barrier. In the case of polymer, carbonyl groups (e.g., aromatic aldehydes), which are luminescence quencher [61], are generated through the oxidation. The local oxidation finally might be an origin of dark spot formation. Crystallization of organic species might be also facilitated by moisture [88], forming protruded bumps, but may not be considered as a principal cause of the dark spot. Smoother substrates are effective on removing the pinholes [71], and thorough encapsulation against oxygen or moisture is required in the device fabrication.

Both excess charges and immobile charges are known to deteriorate both

device performance and lifetime by hurting the organic molecules in emission zone or charge transport layers, illustrated in Fig. 7(e). Excess electrons may interact with molecular excitons, leading to the non-radiative destruction of the excitons [84]. In a polymer OLED, due to relatively low electron mobility, the electrons have a more opportunity to form bipolarons (i.e., quite stable and effective exciton quenchers) [89,90]. Moreover, the relatively immobile space charge formed by the bipolarons or their more chemically stable rearranged forms would increase the drive voltage and charge imbalance. On the other hand, because Alq3 is an excellent electron transport layer [91], electron transport is not expected to cause device degradation. However, oxidation of Alq3, which was found to be irreversible through cyclic voltammetry [92], causes unstable cationic Alq3 species by the excess hole. According to the device degradation model based on the unstable Alq3 cations, the device half-life ($t_{1/2}$) is considered to be inversely proportional to the concentration of the Alq3 cationic species ($Alq3^+$) [93,94], given by Boltzmann statistics:

$$t_{1/2} \sim t_{1/2} \approx \frac{1}{[Alq3^+]} = A \exp\left(\frac{\Delta E}{kT}\right) \tag{17}$$

where the pre-exponential factor, A, has material dependency in hole injection characteristics and space charge distribution [94], and ΔE (namely, activation energy for the formation of Alq3 cation) is speculated to be the difference between HOMO energy levels of Alq3 and the hole transport molecule. The activation energy obtained from temperature dependency of luminance decrease under electrical stress was found to be in good agreement with an estimated value from

the difference between ionization potentials of Alq3 and NPB [93]. Moreover, according to the Kondakov's results (device architecture: ITO/CF_x (fluorocarbon plasma polymer, 1 nm)/NPB/Alq3/Mg:Ag), luminance efficiency versus characteristic voltage change with electrical stress (η_c-ΔV) was explained with accumulated immobile positive charges at the HTL/ETL interface by using impedance analysis technique (capacitance verse voltage), although the chemical nature of the positive charge was unclear, additionally showing a similar slope of η_c-ΔV curve for different temperature conditions in which the degradation rate increased five times at 70 °C compared to that at room temperature [95]. During the operation of an OLED, fixed charges such as cationic Alq3 will accumulate near the HTL/EML interface and hinder further charge injection and transportation, leading to an increase in the driving voltage [95]. The fixed charges seem to be non-radiative trapping centers, as implied by the linear correlation between the increase in fixed charge density and the decrease in luminance efficiency [95,96] and by other experimental evidences [82,97,98]. Thus, higher hole/electron ratios lead to faster degradation of Alq3-based OLED devices [73,82]: they accelerate the formation of non-radiative trapping centers, leading to the luminance decay and drive voltage increase. Therefore, according to the degradation mechanism based on Alq3 cation formation, the enhanced device stability from a mixed emitting layer of hole and electron transporting molecules is explained as follows: holes in the mixed layer will preferentially reside on a hole transport material because of the lower ionization potential, whereas electrons will reside on Alq3, and the direct recombination of holes and Alq3 anions producing excited states of Alq3 will be a

dominant exciton recombination process. Furthermore, Kondakov *et al*. showed the similar phenomenology associated with the electrical ageing in a non-Alq3 emitting material, 9,10-*bis*(2-naphthyl)-2-*t*-butylanthracene (TBADN). The degradation mechanism was ascribe to the hole traps (and trapped holes) or electron traps, in which the letter may be represented by metal ions diffused from the electrodes. The hole traps or electron traps could easily act as non-radiative recombination centers [68,95,98].

The degradation factors are categorized along the external of internal sources, and their resultant device failure modes are connected with arrow line(s), as summarized in Fig. 8. Among the external factors, heat and electric field still seem to predominantly affect the device degradation while others such as oxygen and moisture permeation have been considerably alleviated with stringent encapsulation technologies. The generated heat during operation is one of the main issues for both physical (e.g., organic inter-diffusion or crystallization) degradation and chemical decomposition of organic materials [61,64]. It is noteworthy that the organic inter-diffusion can change the photoluminescence color [99] because color coordinate shifts are a typically appeared phenomenon after prolonged electrical stress in addition to the luminance decay. Thus, typically, a higher power-efficient device has longer lifespan maybe due to the lowered electrical energy conversion to heat [96]. Moreover, the heat dissipation is one of the hot issues in practical applications of OLEDs. Especially for large area display, due to much poorer heat-convection and the lack of lateral heat transport, the temperature rise is substantially higher than for small displays [100]. The main heat source during

operation is considered to be originated from Joule heat under the applied electric filed. Thus, well-distributed electric field gradients between anode and cathode and decreased drive voltage will be very effective on the elongation of device life time.

Particles in metallic cathode can give a room for ambient moisture or oxygen to penetrate into the internal layers of OLED devices, or particles in anodic sides allow cathode metal to get close to the anode by generating pinholes between the electrodes or by thinning organic interlayer. The thin spot can be burnt out by a concentrated electric field current, finally leading to the generation of dark spot. Although the particles have been relatively well-controllable in glass substrate-based OLED device fabrication, they are still a big issue in handling plastic substrates for flexible OLED displays.

Intrinsic factors are critically considered for rational design of OLED devices. The electrode surfaces are both physically and chemically cleaned and buffered with organic or inorganic layer to suppress the contamination of inner charge transport organics and to enhance the charge carrier injection from the electrodes with essential smooth surface. More basically, challenges are converged into the charge balancing because the charge imbalance cause the intrinsic decrease in the electroluminescence efficiency of the devices during operation, through forming the trapped charges and converting the excitons to nonratiative decay centers with another adverse effect of driving voltage increase.

I-3. Inorganic/organic interface engineering in OLEDs

Charge injection efficiency from an electrode to a charge transport layer is a crucial factor to lower the driving voltage and then the power consumption, and to enhance device stability because the intrinsic factors of the device degradation in Fig. 8 are intensively related to the interfacial properties such as electronic injection barrier and interfacial energy. Many works have been done to enhance the charge injection efficiency mainly by introducing a buffer layer between electrode and charge transport layer.

Several mechanisms have been suggested to explain the origin of the effect of the interlayer. For some buffer layer materials, one mechanistic model may not be sufficient to explain the origin of the enhanced efficiency. Surface scientists have investigated the solid/solid interface phenomena, for example, HOMO/LUMO shift and new gap state formation, mainly by using photoelectron spectroscopic techniques. Thus, useful intuition for the interfacial engineering has accumulated from the electronic structure studies. But the fundamental origins or interfacial chemistry about HOMO/LUMO shift or new gap state generation have not been fully understood. In some severe cases, controversial estimations seem to be reported for the same buffer layer species in a similar interfacial system. Therefore further in-depth surface studies have to be made for rational design and cost-effective device architecture through detail understanding of interfacial phenomena.

I-3-1. Metal halides as an EIL

Insulating thin layers between the electrodes and organic layers has been shown to dramatically improve the charge carrier injection. The mechanistic origins have been explained by voltage dropping across the insulator under the applied voltage, or bend bending or vacuum level shift through interfacial dipole layer formation, resulting in the decrease in the energy barrier between the Fermi level of the electrodes and the LUMO of the adjacent organic layers. Among the insulating materials, metal halides are widely applied as electron injection thin buffer layers due to their likely liberation of low work metallic ingredients. However it is not yet clear whether the metal halides behave as insulating layers for dropping the voltage or as source materials for the generation of low work function metal elements to meet the Fermi level of the cathode metals. Therefore closer look into the chemistry at the interfacial layers is important for engineering the OLED device to meet the requirements of lower injection barrier and then lower power consumption and longer lifetime.

LiF, the most typical electron injection buffer material, is known to be dissociated in the presence of Alq3 and Al. Mason *et al.* found that a new gap state appeared in the valence band region of UPS as shown when other alkaline or alkali earth pure metals exist with aluminum (Al) [101]. From quantum-chemical calculations at the density functional theory level, each electron transferred from the pure metals seemed to be stored on one of the three ligands of the Alq3 molecule, resulting in the new gap spectral feature. Moreover, they showed that as little as sub-angstrom thickness of Al deposition on Alq3 was sufficient to almost destroy the well-defined valence band spectral structure of Alq3 without gap state

formation whereas introduction of LiF interlayer prior to the deposition of Al preserved the basic molecular structure of underlying Alq3 layer. Therefore it was suggested that the enhanced injection by LiF is due to a reaction between the liberated Li and the Al metal to form a lower work function cathode (Al:Li alloy) and that the above mentioned Alq3 radical anion is simply a byproduct for reduction of the Al-bonding-induced degradation of Alq3. However, the gap sates do not appear when the LiF is only with Alq3 without Al as reported by Park et al [102]. Further, they noted that the HOMO of Alq3 was shifted downwardly upon deposition of LiF (or NaF) on the Alq3 layer. The origin of HOMO level shift upon fluoride deposition is not still clear. Some kind of chemical reaction between Alq3 and the fluorides are expected. Heil *et al.* also suggested that the LiF was dissociated during the OLED device fabrication [103]. They pointed out that only Al is thermodynamically difficult to cause the dissociation of LiF. Thus they took into account the presence of water which was found to be present in the evaporation chamber by mass spectroscopy. By assuming that the LiF surface was covered with water adsorbates, it was found that water molecules could initiate the reduction of LiF to form free Li metal atoms thermodynamically.

However, LiF seems to be not so dissociative in other systems using polymers instead of Alq3. Greczynski *et al.* reported that deposition of LiF on PFO (poly(9,9-dioctyl-fluorene) surface did not cause doping of the polymer films, nor did the LiF dissociate at the interface whereas Li-deposition on the polymer films caused doping of the polymer films as indicated from observation of new gap states [104]. The new gap states were identified as (bi-)polarons of the polymer but still

unknown for the chemical identities. Mass spectrometric studies were also carried out to identify the interfacial reaction – whether the Li is liberated from LiF or not. Gennip *et al.* investigated the chemical reaction of LiF at the interface of Al/MDMO-PPV (poly[2-methoxy-5-(3'-7'-dimethyloctyloxy)1,4-phenylene-vinylene]) or PCBM (1-[3-(methoxycarbonyl)propyl]-1-1-phenyl[6,6]C_{61}) polymers [105]. In the case of Li liberation from the interfacial chemical reaction of LiF on the electron injection at the Al cathode, the formation of a Li^{+}polymer^{-} or Li^{+}molecule^{-} complex would occur after reaction of LiF with Al, giving intermediates of AlF_3 and liberated Li [101]. They used high energy of primary Xe ion beam of 5 keV to get the secondary ion fragments. Due to the high energy of primary ion beam, many molecular fragments are detected. Among the secondary ion mass spectral peaks, they observed very low intensity of molecular fragments which would be originated from AlF_3. Pure AlF_3 powder pressed into In-foil as control sample was used to get a secondary ion mass spectral pattern of AlF_3. The spectral pattern of Al/LiF/PCBM or Al/LiF/PPV was not similar to that of pure AlF_3. Therefore they disapproved the formation of AlF_3 and then the dissociation of LiF at the Al/polymer interface. Although the authors said that the matrix effect was not serious because then all signal intensities decrease or increase by more or less the same amount, so called matrix effect has not so similar effect on all mass peaks. Moreover, it seems to be better to use AlF_3 on Al instead of AlF_3 on In-foil as control sample to remove the matrix effect more strictly.

Different from LiF, CsF is more chemically labile than LiF. Thus, CsF has higher possibility of low work function metal (Cs here) liberation at Al/organic

interfaces. Greeczynski et al. reported the release of Cs from the CsF at the interface of Al/PFO, generating the intermediates of Cs^{+}polymer^{-} and AlF_3 which were identified from XPS (X-ray photoelectron spectroscopy) results [106]. On other hand LiF did not show significant binding energy shifts of any of core levels, implying non-dissociation of LiF. Chen et al. investigated the impact of the metal cathode on the CsF buffer [5]. By comparison of current-voltage-luminance (*I-V-L*) characteristics with the overall heats of formation for metal fluoride dissociation, the release of free Cs metal atoms from CsF at the metal/Alq3 interface was estimated. As expected, decreasing the work function of cathode clearly improves the device performance. The work function changes along with different cathode metals became not so effective on the *I-V* characteristics by introducing CsF cathodic buffer layer except when a noble metal such as Ag as cathode metal is used.

Many other metal halides were also studied as electron injection buffer layer. Yi *et al.* reported that NaCl, cheaper than LiF, caused a new gap state at the interface of Al and Alq3 as in the case of LiF [107]. Core energy levels of NaCl and Alq3 were not significantly shifted, just showing a very weak interaction between Alq3 and NaCl or Al from XPS narrow scan data. Thus, Na-Cl bond breaking was not evidenced implying no possibility of Na liberation from the NaCl. Moreover the negative charge transfer seemed to occur from carbon of Alq3 to the NaCl molecule from the XPS data, which is contrary to the expected origin of the gap state, Alq3 anion, formed through the charge transfer from metal-to-Alq3 observed for the case of other alkali metals or their metal halides such as K, Na, Li,

Mg, Ca, LiF, CsF or NaF [101]. Additionally, from Yi's report about CsCl buffer layer for the interface of Alq3/Al, a new gap state is also observed but its origin is not mentioned [6]. Anyway, the chemical origin of the gap state is still not known in detail. On the other hand, Kang *et al.* explained the enhancement of their OLED was due to the liberation of Na from the thin NaCl buffer layer from the stoichiometric results of NaCl with XPS when they introduced NaCl into the interface of Al/Alq3 [2]. For complimentary chemical information, Lee *et al.* used near-edge x-ray absorption fine structure (NEXAFS) technique in addition to XPS and UPS [7]. In that case, KF was introduced as buffer layer. F 1s peak shoulder and change of F *K*-edge NEXAFS were consistent with the HOMO level shift at the instance of the very first deposited layer of KF on Alq3. Thus, they suggested that the HOMO level shift originated from the dipole layer formation or K^+ ion doping of the Alq3 through strong interaction between KF and Alq3. With deposition of Al, the KF/Al showed F 1s peak shift and gradual changes of F *K*-edge NEXAFS and new peak at lower binding energy side of N 1s. The evidence of dissociation of KF in the presence of Alq3 and Al was not observable because the F 1s peak shift was not so significant if then two peaks in F 1s core level might be observed due to the large difference of binding energies in KF and AlF_3. The gap states in the presence of Al, KF, and Alq3 seems to be originated from the formation of Alq3 anion due to the simultaneous appearance of new peak in the lower binding energy side of N 1sshown in the case of Al/LiF/Alq3 [101]. In the case of MgF_2, its strong interaction with Alq3 was observed from XPS and UPS results showed charge transfer from Alq3 to MgF_2. At the instance of Al deposition,

a new gap state appeared, but the evidence for dissociation of MgF_2 is still unclear [4]. On the other hand, the improved performance of the OLEDs with MgF_2 cathodic buffer was believed to originate from improved morphology and adhesion to the cathode without any experimental evidence while the electron injection enhancement was ascribed to a space charge field which were formed by the accumulated holes at the Alq3/MgF_2 interface because of the decreased tunneling leakage-current of the holes through the MgF_2 barrier. However, the build-up of the space charge decreases the potential drop across the other layers (esp., anodic layer), thus resulting in lower hole injection efficiency under the same bias potential.

Table II summarizes the mechanistic origins related to the metal halides as electron injection buffer materials. Pure alkaline or alkaline earth metal atoms react with Alq3 forming Alq3 anion. The Alq3 anion seems to be the origin of gap state observed in valence band photoemission spectrum. LiF or NaF shows similar gap state implying that the halide dissociates under the presence of Alq3 or water in contact with Al-cathode material, resulting in the liberation of free metal atoms. The origin of HOMO shift, which is more directly related to the electron injection efficiency, is not clear. NaCl also shows a gap-state, even though relatively weak intensity. But there is no evidence of Na-liberation. Moreover, the charge transfer from Alq3 to NaCl is observed through XPS, which seems to be contrary to the formation of Alq3 anion previously predicted from the case of LiF. Other metal halides such as CsCl, KF, and MgF_2 show similar behavior like NaCl, in the aspect that the gap state appears on the presence of Alq3 and Al even without evidence of

free metal atom liberation. The origin of HOMO shift seems to be the dipole layer formation through interaction of the metal halides with Al cathode or the organic layer, and metal atom doping (n-type) of the organic materials via dissociation of the metal halides.

Conclusively, gap-state assignment based on Alq3 anion formation is not be explanatory for other metal halides except LiF even though a similar gap state is observed in the valence band electronic structure. The origin of HOMO level shift is still unclear. Therefore, both theoretical and experimental approach is necessary for more clear understanding about the interfacial chemistry of the metal halide EIL materials. Quantum chemical calculations about metal halide-Alq3 interaction (on Al cathode) have not been reported. Only metal-Alq3 interactions were calculated by using quantum mechanical techniques [108]. Thus, the theoretical studies will be very useful for explaining the previous photoelectron spectroscopic results and estimating the origin of HOMO shift and gap state(s). Experimentally, Cs^+ reactive ion scattering (RIS) technique is expected to be a good candidate. Cs^+ reactive scattering occurs in a sub-picosecond time scale which renders the Cs^+-molecule association to occur only with promptly desorbed molecular species in the region of less than 1 nm over the surface [109]. Therefore, the RIS would be a promising tool to get informative data related to the existing neutrals (e.g., Li, AlF_3 here) or ions (e.g. Li^+) at surfaces.

I-3-2. Metal halides as an HIL

Strategies for the hole injection enhancement through the anode/organic interface would be mechanistically categorized into three electronic energetic schemes (Fig. 9) and mechanical adhesion: introduction of higher work-function (semi-) conductors [110-112], interfacial dipole formation or band-bending [113-125], insertion of an insulating layer between the anode/organic interface for enhanced tunneling under applied forward bias [113,126-130], and interfacial energy matching for enhancement of effective electric contact [112,123,131-134]. Among them, in principle, the insulating materials for the enhanced tunneling is not dependant on whether the electrode/organic interface is for electron injection or hole injection while materials for the other mechanistic schemes have strong dependence on it. Therefore the pre-investigated metal halide insulators for electron injection enhancement can be considered as candidates for hole injection enhancement also.

Table III displays various but not exhaustive hole injection materials with their estimated origins of the hole injection enhancement. Firstly, transition metals or their semiconducting oxide forms were investigated as HIL due to their high work function. Insulating transition metal oxides were also effective on lowering the injection barrier through the interface dipole formation induced from their high work function (typically 5 – 7 eV). On the other hand, organic semiconductors such as Cu phthalocyanine (CuPc, Φ ~4.83 – ~5.1 eV) and a star-burst amine 4,4',4"-tris{N,(3-methylphenyl)-N-phenylamino}-triphenylamine) (Φ ~5.11 eV) showed good wettability on both the ITO anode and the organic HTL material, leading to enhanced effective electric contact. In the case of CuPc, a positive

interfacial dipole (i.e., positive charge outward) layer through a strong chemical interaction between the ITO and CuPc causes negative change of the ITO work function (namely, decrease in work function), but forms a staircase (or ladder-type) HOMO energy level between the ITO and HTL hence reduces the effective hole-injection barrier [123,124]. A (semi-) conductive plasma polymer, UV-illuminated fluorocarbon (CF_x) generates a large interface dipole layer at both sides of the interlayer between ITO anode and NPB HTL due to strong electronegativity of CF_x (namely, negative charge toward CF_x layer) [113,135]. However, at the same HTL coverage, CF_x-coated ITO always showed higher work function than that of uncoated ITO, implying lowering of hole injection barrier. In the aspect of interface dipole by using electronegative moieties, ITO anode surface was been modified with acids such as phosphonic or phosphoric acids, and halide Lewis acids (I_2 or B_2), generating dipole layers at both sides of the interlayer with net increase in the ITO work function (i.e. qualitatively similar to the case of CF_x). However, the degradation of the interface by their strong acidity has been pointed out [136].

Insulating buffer layer in accordance with the tunneling hole-injection mechanism seems to be relatively simple approach for the enhancement of hole injection, but not so many studies have been done. Amorphous carbon and SiO_2 showed tunneling behavior from *J-V* curve with thickness variation of the buffer layer, but hole-injection enhancement was not demonstrated with practically used ITO anodes which are generally pre-treated with UV-ozone (UVO) or O_2-plasma before deposition of HTL or HIL materials. LiF or MgF_2 also showed tunneling

injection behavior and enhanced thermal device stability, especially in the form of mixed phase with HTL materials. However, the LiF did not demonstrate hole injection enhancement with the UVO or O_2-plasma treated ITO. From the limited studies or reports about the metal halides as HIL materials, mere the device life-time (i.e., thermal stability) enhancement seems to be a practically applicable property for high performance OLED device products.

This thesis demonstrates the metal halides can be applied as HIL for practical OLED devices, with both hole injection enhancement and longer life-time. This means that fabrication process for high performance OLED devices can be simpler and cheaper by adopting the same material as in EIL. The mechanisms were investigated in the aspect of both electronic and interfacial energetics.

References

[1] L. S. Hung, C. W. Tang, and M. G. Mason, *Appl. Phys. Lett.* **70**, 152 (1997).

[2] S. J. Kang, D. S. Park, S. Y. Kim, C. N. Whang, K. Jeong, and S. Im, *Appl. Phys. Lett.* **81**, 2581 (2002).

[3] J. Lee, Y. Park, D. Y. Kim, H. Y. Chu, H. Lee, and L.-M. Do, *Appl. Phys. Lett*. **82**, 173 (2003).

[4] Y. Park, J. Lee, S. K. Lee, and D. Y. Kim, *Appl. Phys. Lett*. **79**, 105 (2001).

[5] M. Y. Chan, S. L. Lai, M. K. Fung, C. S. Lee, and S. T. Lee, *J. Appl. Phys*. **95**, 5397 (2004).

[6] Y. Yi, S. J. Kang, K. Cho, J. M. Koo, K. Han, K. Park, M. Noh, C. N. Whang, and K. Jeong, *Appl. Phys. Lett.* **86**, 213502 (2005).

[7] J. Lee, J. S. Lim, H. J. Shin, and Y. Park, *Appl. Phys. Lett.* **91**, 261902 (2007).

[8] S. M. Tadayyon, H. M. Grandin, K. Griffiths, L. L. Coatsworth, P. R. Norton, H. Aziz, Popovic, *Org. Electron.* **5**, 199 (2004).

[9] K. Sugiyama, H. Ishii, and Y. Ouchi, *J. Appl. Phys*. **87**, 295 (2000).

[10] S.-F. Chen, and C.-W. Wang, *Appl. Phys. Lett.* **85**, 765 (2004).

[11] C. O. Poon, F. L. Wong, S. W. Tong, R. Q. Zhang, C. S. Lee, and S. T. Lee, *Appl.Phys. Lett.* **83**, 1038 (2003).

[12] H. Lee, S. W. Cho, K. Han, P. E. Jeon, C.-N. Whang, K. Jeong, K. Cho, and Y. Yi, *Appl. Phys. Lett.* **93**, 043308 (2008).

[13] C. Qui, Z. Xie, H. Chen, M. Wong, and H. S. Kwok, *J. Appl. Phys.* **93**, 3253 (2003).

[14] Y. Shen, D. B. Jacobs, G. G. Malliaras, G. Koley, M. G. Spencer, and A. Ioannidis, *Adv. Mater.* **13**, 1234 (2001).

[15] S. A. Van Slyke, C. H. Chen, and C. W. Tang, *Appl. Phys. Lett.* **69**, 2160 (1996).

[16] W. Brütting, S. Berleo, and A. G. Mückl, *Org. Electron.* **2**, 1 (2001).

[17] L. B. Schein and D. W. Brown, *Mol. Cryst. Liq. Cryst.* **87**, 1 (1982).

[18] W. Brütting, M. Meier, M. Herold, S. Karg, and M. Schwoerer, *Chem. Phys.* **227**, 243 (1998).

[19] S. M. Sze, *Physics of Semiconductor Devices* (Wiley, New York, 1981).

[20] P. E. Burrows, Z. Shen, V. Bulovic, D. M. McCarty, S. R. Forrest, J. A. Cronin, and M. E. Thompson, *J. Appl. Phys.* **79**, 7991 (1996).

[21] U. Wolf, V. I. Arkhipov, and H. Bässler, *Phys. Rev. B* **59**, 7507 (1999).

[22] I. D. Parker, *J. Appl. Phys.* **75**, 1656 (1994).

[23] M. A. Lampert and P. Mark, *Current Injection in Solids* (Academic, New York, 1970).

[24] P. N. Murgatroyd, *J. Phys. D: Appl. Phys.* **3**, 151 (1970).

[25] M. Abkowitz, J. S. Facci, and M. Stolka, *Chem. Phys.* **177**, 783 (1993).

[26] K. C. Kao, and W. Hwang, *Electrical Transport in Solids* (Pergamon Press, Oxford, 1981).

[27] L. B. Schein, and D. W. Brown, *Mol. Cryst. Liq. Cryst.* **87**, 1 (1982).

[28] M. Pope and C. E. Swenberg, *Electronic Processes in Organic Crystals and Polymers*, 2nd ed. (Oxford University Press, Oxford, 1999).

[29] M. Stöβel, J. Staudigel, F. Steuber, J. Blässing, J. Simmerer, A. Winnacker, *Appl. Phys. Lett.* **76**, 115 (2000).

[30] S. Barth, U. Wolf, H. Bässler, P. Müller, H. Riel, H. Vestweber, P. F. Seidler, and W. Rieβ, Phys. Rev. B **60**, 8791 (1999).

[31] T. Tsutsui, H. Tokuhisa, and M. Era, *Proc. SPIE* **3281**, 230 (1998).

[32] S. Naka, H. Okada, H. Onnagawa, J.Kido, and T. Tsutsui, *Jpn. J. Appl. Phys.* **38**, L1252 (1999).

[33] E. A. Silinsh, *Organic Molecular Crystals* (Springer, Berlin, 1980).

[34] P. Monkman, H. D. Burrows, L. J. Hartwell, L. E. Horsburgh, I. Hamblett, and S. Navaratnam, *Phys. Rev. Lett.* **86**, 1358 (2001).

[35] J. S. Wilson, A. Köhler, R. H. Friend, M. K. Al-Suti, M. R. A. Al-Mandhary, M. S. Khan, and P. R. Raithby, *J. Chem. Phys.* **113**, 7627 (2000).

[36] D. Hertel, S. Setayesh, H.-G. Nothofer, U. Scherf, K. Müllen, and H. Bässler,

Adv. Mater. **13**, 65 (2001).

[37] M. A. Baldo, D. F. O'Brien, Y. You, A. Shoustikov, s. Sibley, M. E. Thompson, and S. R. Forrest, *Nature* **395**, 151 (1998).

[38] M. A. Baldo, S. M. Lamansky, P. E. Burrows, M. E. Thompson, and S. R. Forrest, *Appl. Phys. Lett.* **75**, 4 (1999).

[39] R. R. Chance, A. Prock, and R. Sibey, *J. Chem. Phys.* **62**, 2245 (1975).

[40] V. Bulović, V. B. Khalfin, G. Gu, and P. E. Burrows, D. Z. Garbuzov, and S. R. Forrest, *Phys. Rev. B* **58**, 3730 (1998).

[41] J.-S.Kim, P. K. H. Ho, N. C. Greenham, and R. H. Friend, *J. Appl. Phys.* **88**, 1073 (2000).

[42] N. C. Greenham, R. H. Friend, and D. D. C. Bradley, *Adv. Mater.* **6**, 491 (1994).

[43] C. F. Madigan, M. H. Lu, and J. C. Strum, *Appl. Phys. Lett.* **76**, 1650 (2000).

[44] N. K. Patel, S. Cinà, and J. H. Burroughes, *IEEE J. Select. Topoics Quantum Electron.* **8**, 346 (2002).

[45] J. Grüner, F. Cacialli, and R. H. Friend, *J. Appl. Phys.* **80**, 207 (1996).

[46] R. Windisch, P. Heremans, A. Knoloch, P. Kiesel, G. H. Döhler, B. Dutta, and G. Borghs, *Appl. Phys. Lett.* **74**, 2256 (1999).

[47] T. Yamasaki, K. Sumioka, and T. Tsutsui, *Appl. Phys. Lett.* **76**, 1243 (2000).

[48] T. Yamasaki and T. Tsutsui, *Jpn. J. Appl. Phys.* **38**, 5916 (1999).

[49] R. H. Jordan, L. J. Rothberg, A. Dodabalapur, and R. E. Slusher, *Appl. Phys. Lett.* **69**, 1997 (1996).

[50] M.-H. Lu and J. C. Strum, *J. Appl. Phys.* **91**, 595 (2002).

[51] R. E. Slusher and C. Weisbuch, *Solid State Commun.* **92**, 149 (1994).

[52] C. Qiu, H. Peng, H. Chen, Z. Xie, M. Wong, and H. S. Kwok, *IEEE Trans. Electron Devices* 51, 1207 (2004).

[53] H. Riel, S. Karg, T. Beierlein, B. Ruhstaller, and W. Rieβ, *App. Phys. Lett.* **82**, 466 (2003).

[54] K. Neyts P. De Visschere, D. K. Fork, and G. B. Anderson, *J. Opt. Soc. Am. B* **17**, 114 (2000).

[55] J. Lim, S. S. Oh, D. Y. Kim, S. H. Cho, I. T. Kim, S. H. Han, H. Takezoe, E. H. Choi, G. S. Cho, Y. H. Seo, S. O. Kang, and B. Park, *Opt. Express* **14**, 6564 (2006).

[56] C. Hosokawa, M. Eida, M. Matsuura, K. Fukuoka, H. Nakamura, and T. Kusumoto, *Dig. Soc. Inform. Display*, 1073 (1997).

[57] T. Mori, S. Miyake, and T. Mizutani, *Jpn. J. Appl. Phys.*, Part 2 **34**, L1485 (1995).

[58] M. Fujihira, L. Do, A. Koike, and E. Han, *Appl. Phys. Lett.* **68**, 1787 (1996).

[59] M. Fujihira, L.-M. Do, A. Koike, and E.-M. Han, *Appl. Phys. Lett.* **68**, 1787 (1996).

[60] Z. Q. Gao, W. Y. Lai, T. C. Won, C. S. Lee, I. Bello, and S. T. Lee, *Appl. Phys. Lett.* **74**, 3269 (1999).

[61] M. Yan, L. J. Rothberg, F. Papadimitrakopoulos, M. E. Galvin, and T. M. Miller, *Phys. Rev. Lett.* **73**, 744 (1994).

[62] L. Ke, S.-J. Chua, K. Zhang, and N. Yakovlev, *Appl. Phys. Lett.* **80**, 2195 (2002).

[63] P. Melpignano, A. Baron-Toaldo, V. Biondo, S. Priante, R. Zamboni, M. Murgia, S. Caria, L. Gregoratti, A. Barinov, and M. Kiskinova, *Appl. Phys. Lett.* **86**, 041105 (2005).

[64] X. Zhou, J. He, L. S. Liao, M. Lu, Z. H. Xiong, X. M. Ding, X. Y. Hou, F. G. Tao, C. E. Zhou, S. T. Lee, *Adv. Mater.* **12**, 265 (2000).

[65] L. S. Liao, L. F. Cheng, X. H. Sun, N. B. Wong, C. S. Lee, and S. T. Lee, *Chem. Phys. Lett.* **356**, 194 (2002).

[66] G. Liu, J. B. Kerr, and S. Johnson, *Synth. Met.* **144**, 1 (2004).

[67] W. R. Salaneck *et al.*, *Adv. Mater.* **8**, 48 (1996).

[68] J. Shen, D. Wang, E. Langlois, W. A. Barrow, P. J. Green, C. W. Tang, and J. Shi, Synth. Met. 111, 233 (2000).

[69] A. R. Schlatmann, D. W. Floet, A. Hilberer, F. Garten, P. J. M. Smulders, T. M. Klapwijk, G., and Hadziioannou, *Appl. Phys. Lett.* **69**, 1764 (1996).

[70] S. T. Lee, Z. Q. Gao, and L. S. Hung, *Appl. Phys. Lett.* **75**, 1404 (1999).

[71] J. R. Sheats and D. B. Roitman, *Synth. Met.* **95**, 79 (1998).

[72] H. Vestweber and W. Rieb, *Synth. Met.* **91**, 181 (1997).

[73] H. Aziz, and Z. D. Popovic, *Appl. Phys. Lett.* **80**, 2180 (2002).

[74] E. I. Haskal, A. Curioni, P. F. Seidler, and W. Andreoni, *Appl. Phys. Lett.* **71**, 1151 (1997).

[75] M. B. Huang, K. McDonald, J. C. Keay, Y. Q. Wang, S. J. Rosenthal, R. A. Weller, and L. C. Feldman, *Appl. Phys. Lett.* **73**, 2914 (1998).

[76] Y. Hirose, A. Kahn, V. Aristov, and P. Soukiassian, *Appl. Phys. Lett.* **68**, 217 (1996).

[77] J. C. Scott, S. A. Carter, S. Karg, and M. Angelopoulos, *Synth. Met.* **85**, 1197 (1997).

[78] S. Y. Kim, K. Y. Kim, Y.-H. Tak, and J.-L. Lee, *Appl. Phys. Lett.* **89**, 132108 (2006).

[79] C. H. Chen, J. Shi, and C. W. Tang, *Macromol. Symp.*, 1997, **125**, 1.

[80] K. Naito and A. Miura, *J. Phys. Chem*. **97**, 6240 (1993).

[81] P. F. Smith, P. Gerroir, S. Xie, A. M. Hor, and Z. Popovic, *Langmuir* **14**, 5946 (1998).

[82] H. Aziz, Z. D. Popovic, N.-X. Hu, A.-M. Hor, and G. Xu, *Science* **283**, 1900 (1999).

[83] C. Adachi, K. Nagai, and N. Tamoto, *Appl. Phys. Lett.* **66**, 2679 (1995).

[84] K. C. Kao, and W. Hwang, *Electrical Transport in Solids* (Pergamon, New York, 1981), p. 485.

[85] D. Kolosov, D. S. English, V. Bulovic, P. F. Barbara, S. R. Forrest, and M. E. Thompson, *J. Appl. Phys*. **90**, 3242 (2001).

[86] H. Ishi, K. Sugiyama, E. Ito, and K. Seki, *Adv. Mater.* **11**, 605 (1999).

[87] G. Gu, G. Parthasarathy, and S. R. Forrest, *Appl. Phys. Lett.* **74**, 305 (1999).

[88] H. Aziz, Z. Popovic, S. Xie, A. M. Hor, N. X. Hu, C. Tripp, and G. Xu, *Appl. Phys. Lett.* **72**, 756 (1998).

[89] H. Antoniadis, M. Abkowitz, and B. R. Hsieh, *Appl. Phys. Lett.* **65**, 2030 (1994).

[90] N. C. Greenham, J. Shinar, J. Partee, P. A. Lane, O. Amir, F. Ju, and R. H. Friend, *Phys. Rev. B* **53**, 13528 (1996).

[91] L. B. Bin, S. A. Jenekhe, R. H. Young, P. M. Borsenberger, *Appl. Phys. Lett.* **70**, 2052 (1997).

[92] F. Papadimitrakopoulos, X.-M. Zhang, D. L. Thomsen Ill, K. A. Higinson, *Chem. Mater.* **8**, 1363 (1996).

[93] H. Aziz, Z. D. Popovic, and N.-X. Hu, *Appl. Phys. Lett.* **81**, 370 (2002).

[94] G. Vamvounis, H. Aziz, N.-X. Hu, and Z. D. Popovic, *Synth. Met.* **143**, 69 (2004).

[95] D. Y. Kondakov, J. R. Sandifer, C. W. Tang, R. H. Young, *J. Appl. Phys.* **93**, 1108 (2003).

[96] J.-H. Lee, J.J. Huang, C.-C. Liao, P.-J. Hu, and Y. Chang, *Chem. Phys. Lett.*, **402**, 335 (2005).

[97] Z. D. Popovic, H. Aziz, A. Ioannidis, N. Hu, and P. N. M. dos Anjos, *Synth. Mat.* **123**, 179 (2001).

[98] Z. D. Popovic, H. Aziz, N. Hu, A. Ioannidis, and P. N. M. dos Anjos, *J. Appl. Phys.* **89**, 4673 (2001).

[99] E. M. Han, L. M. Do, N. Yamamoto, and M. Fujihira, *Mol. Cryst. Liq. Cryst.* **267**, 411 (1995).

[100] J. C. Sturm, W. Wilson, and M. Iodice, *IEEE J. Sel. Top. Quantum Electron.* **4**, 75 (1998).

[101] M. G. Mason; C. W. Tang, L.-S. Hung, P. Raychaudhuri, J. Madathil, D. J. Giesen, L. Yan, Q. T. Le, Y. Gao, S.-T. Lee, L. S. Liao, L. F. Cheng, W. R. Salaneck, D. A. dos Santos, and J. L. Brédas, *J. Appl. Phys.* **89**, 2756 (2001).

[102] Y. Park et al. *Appl. Phys. Lett.* **82**, 173 (2003).

[103] H. Heil, J. Steiger, S. Karg, M. Gastel, H. Ortner, H. von Seggern, and M. Stößel, *J. Appl. Phys.* **89**, 420 (2001).

[104] G. Greczynski, M. Fahlman, and W. R. Salaneck, *J. Appl. Phys.* **113**, 2407 (2000).

[105] W. J. H. van Gennip, J. K. J. van Duren, P. C. Thüne, R. A. J. Janssen, and J. W. Niemantsverdriet, *J. Chem. Phys.* **117**, 5031 (2002).

[106] G. Greczynski, W. R. Salaneck, and M. Fahlman, *Appl. Surf. Sci.* **175**, 319 (2001).

[107] Y. Yi, S. J. Kang, K. Cho, J. M. Koo, K. Han, K. Park, M. Noh, C.-N. Whang, K. Jeong, and E. J. Hahn, *Appl. Phys. Lett.* **86**, 113503 (2005).

[108] (a) R. Q. Zhang, X. G. Xie, S. X. Liu, C. S. Lee, and S. T. Lee, *Chem. Phys. Lett.* **330**, 484 (2000). (b) A. Curioni, and W. Andreoni, *J. Am. Chem. Soc.* **121**, 8216 (1999). (c) R. Q. Zhang, W. C. Lu, C. S. Lee, L. S. Hung, and S. T. Lee, *J. Chem. Phys.* **116**, 8827 (2002). (d) R. Q. Zhang, X. Y. Hou, and S. T. Lee, *Appl. Phys. Lett.* **74**, 1612 (1999).

[109] (a) H. Kang; K. D. Kim, and K. Y. Kim, *J. Am. Chem. Soc.* **119**, 12002 (1997). (b) T.-H. Shin, S.-J. Han, and H. Kang, *Nucl. Instrum. Methods Phys. Res. Sect. B* **157**, 191 (1999). (c) M. C. Yang, C. H. Hwang, and H. Kang, *J. Chem. Phys*. **107**, 2611 (1997).

[110] J.-M. Moon, J.-H. Bae, J.-A Jeong, S.-W. Jeong, N.-J. Park, H.-K. Kim, J.-W. Kang, J.-J. Kim, and M.-S. Yi, *Appl. Phys. Lett.* **90**, 163516 (2007).

[111] I-M. Chan and F. C. Hong, *Thin Solid Films* **450**, 304 (2004).

[112] Y. Shen, D. B. Jacobs, G. G. Malliaras, G. Koley, M. G. Spencer, and A. Ioannidis, *Adv. Mater.* **13**, 1234 (2001).

[113] S. W. Tong, K. M. Lau, H. Y. Sun, M. K. Fung, C. S. Lee, Y. Lifshitz, and S. T. Lee, *Appl. Surf. Sci.* **252**, 3806 (2006).

[114] D. J. Milliron, I. G. Hill, C. Shen, A. Kahn, and J. Schwartz, *J. Appl. Phys.* **87**, 572 (2000).

[115] F. Nüesch, L. J. Rothberg, E. W. Forsythe, Q. T. Le, and Y. Gao, *Appl. Phys. Lett.* **74**, 880 (1999).

[116] S. Y. Kim, J.-L. Lee, K.-B. Kim, and Y.-H. Tak, *J. Appl. Phys.* **95**, 2560 (2004).

[117] S. Y. Kim, K. Hong, and J.-L. Lee, *Appl. Phys. Lett.* **90**, 183508-1 (2007).

[118] H. Lee, S. W. Cho, K. Han, P. E. Jeon, C.-N. Wang, K. Jeong, K. Cho, and Y. Yi, *Appl. Phys. Lett.* **93**, 043308 (2008).

[119] H. M. Zhang and W. C. H. Choy, *IEEE Trans. Electron Devices* 55, 2517 (2008).

[120] X. M. Ding, L. M. Hung, L. F. Cheng, Z. B. Deng, X. Y. Hou, C. S. Lee, and S. T. Lee, *Appl. Phys. Lett.* **76**, 2704 (2000).

[121] A. Sharma, P. J. Hotchkiss, S. R. Marder, and B. Kippelen, *J. Appl. Phys*.**105**, 084507 (2009).

[122] X. L. Zhu, J. X. Sun, H. J. Peng, Z. G. Meng, M. Wong, and H. S. Kwok, *Appl. Phys. Lett.* **87**, 153508 (2005).

[123] S. M. Tadayyon, H. M. Grandin, K. Griffiths, P. R. Norton, H. Aziz, and Z. D. Popovic, *Org. Electron.* **5**, 157 (2004).

[124] H. Peisert, M. Knupfer, T. Schwieger, and J. Fink, *Appl. Phys. Lett.* **80**, 2916 (2002).

[125] X. H. Sun, L. F. Cheng, M. W. Liu, L. S. Liao, N. B. Wong, C. S. Lee, and S. T. Lee, *Chem. Phys. Lett.* 370, 425 (2003)

[126] Z. B. Deng, X. M. Ding, S. T. Lee, and W. A. Gambling, *Appl. Phys. Lett.* **74**, 2227 (1999).

[127] J. M. Zhao, S. T. Zhang, X. J. Wang, Y. Q. Zhan, X. Z. Wang, G. Y. Zhong, Z. J. Wang, X. M. Ding, W. Huang, and X. Y. Hou, *Appl. Phys. Lett.* **84**, 2913 (2004).

[128] X. Jing et al, *Chinese Phys. Lett.* **23**, 928 (2006).

[129] D. Grozea, A. Turak, Y. Yuan, S. Han, Z. H. Lu, and W. Y. Kim, *J. Appl. Phys.* **101**, 033522 (2007).

[130] S. Tokito, and Y. Taga, *Appl. Phys. Lett.* **66**, 673 (1995).

[131] J. S. Kim, R. H. Friend, and F. Cacialli, *J. Appl. Phys.* **86**, 2774 (1999).

[132] S.-F. Chen and C.-W. Wang, *Appl. Phys. Lett.* **85**, 765 (2004).

[133] J. Cui, Q. Huang, J. C. G. Veinot, H. Yan, Q. Wang, G. R. Hutchison, A. G. Richter, G. Evmenenko, P. Dutta, and T. J. Marks, *Langmuir* **18**, 9958 (2002).

[134] B. J. Chen, X. W. Sun, B. K. Tay, L. Ke, and S. J. Chua, *Appl. Phys. Lett.* **86**, 063506 (2005).

[135] S. W. Tong, C. S. Lee, Y. Lifshitz, D. Q. Gao, and S. T. Lee, *Appl. Phys. Lett.* **84**, 4032 (2004).

[136] A. C. Arias, M. Granström, D. S. Thomas, K. Petritsch, and R. H. Friend, *Phys. Rev. B* **60**, 1854 (1999).

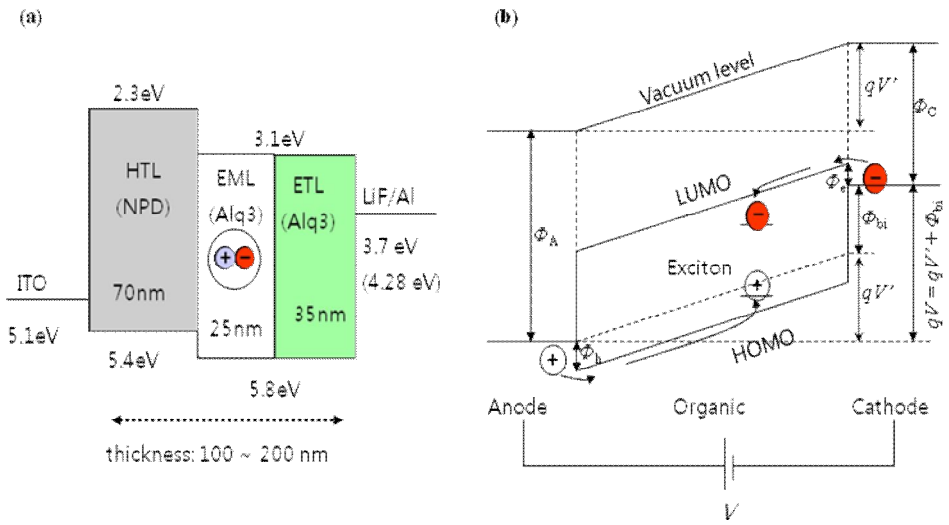

FIG. 1-1. (a) Stack-up structure of an OLED device in the flat band condition and (b) schematic diagram of the electroluminescence process (charge injection, transport, and exciton formation) in an OLED device with single organic layer; the polaronic effects and discrete transport states are neglected for brevity. Φ_A, Φ_h, Φ_e, Φ_{bi}, Φ_C, V', q, qV', and qV correspond to the anode work function, hole injection barrier, electron injection barrier, built-in potential, cathode work function, effective voltage, elementary charge, effective potential, and applied potential difference between the electrodes, respectively.

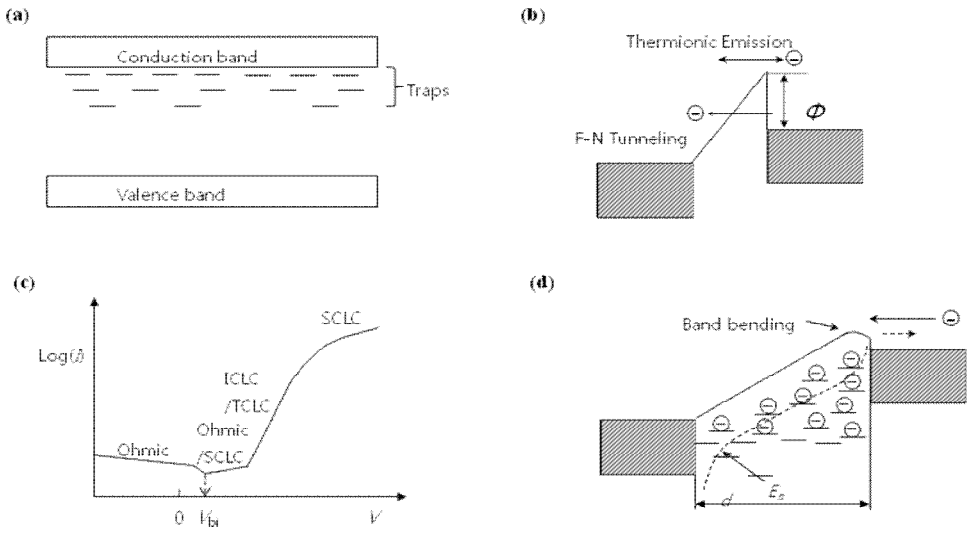

FIG. 1-2. (a) Illustration of exponential trap distribution in organic semiconductors, (b) charge (here, for electron) injection mechanisms: Richardson-Schottky thermionic emission and Fowler-Nordheim tunneling, (c) schematic *I-V* characteristic curve with a dominant current mechanism in each corresponded bias region, and (d) trapped charge or space charge limited current in bulk, where dotted line is the electron quasi-Fermi level (E_n).

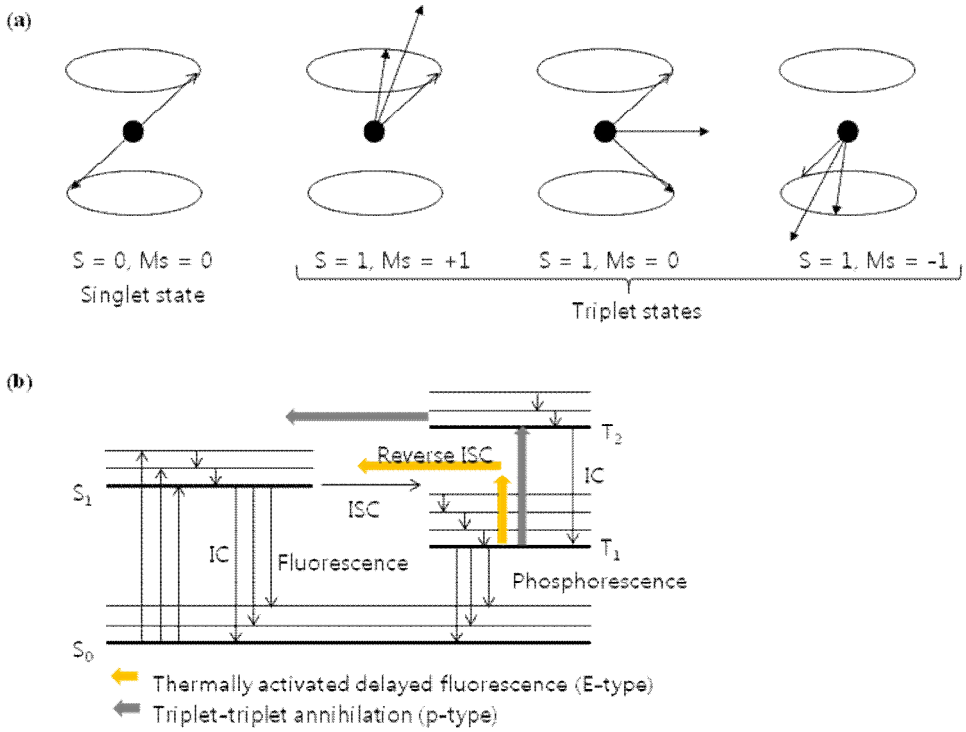

FIG. 1-3. (a) Exciton states formed in electroluminescence. (b) Exciton recombination process for the fluorescence and phosphorescence on the Perrin-Jablonski diagram.

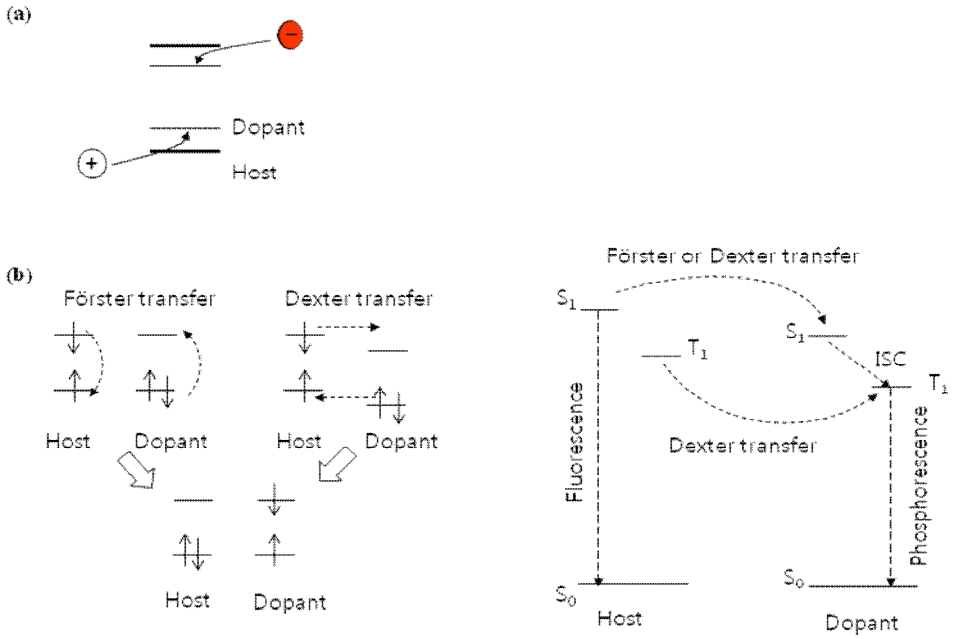

FIG. 1-4. Exciton recombination mechanisms in the host/dopant system: (a) charge-trapping model and (b) energy transfer model.

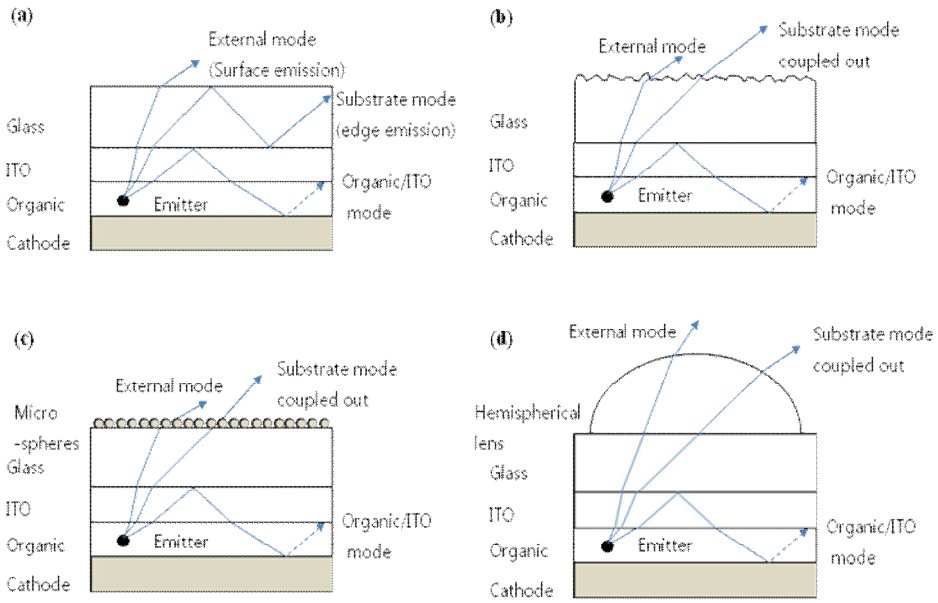

FIG. 1-5. (a) Light emission modes of a typical OLED device: dashed arrows denote the partial reflection on the cathode surface from non-radiative loss through light-absorption of the metal electrode. (b) Substrate mode coupled out deduced from the roughened surface of the substrate, (c) substrate mode coupled out through enhanced surface scattering from microspheres and (d) substrate mode coupled out through hemisphere micro-lenses [Ref. 43,44].

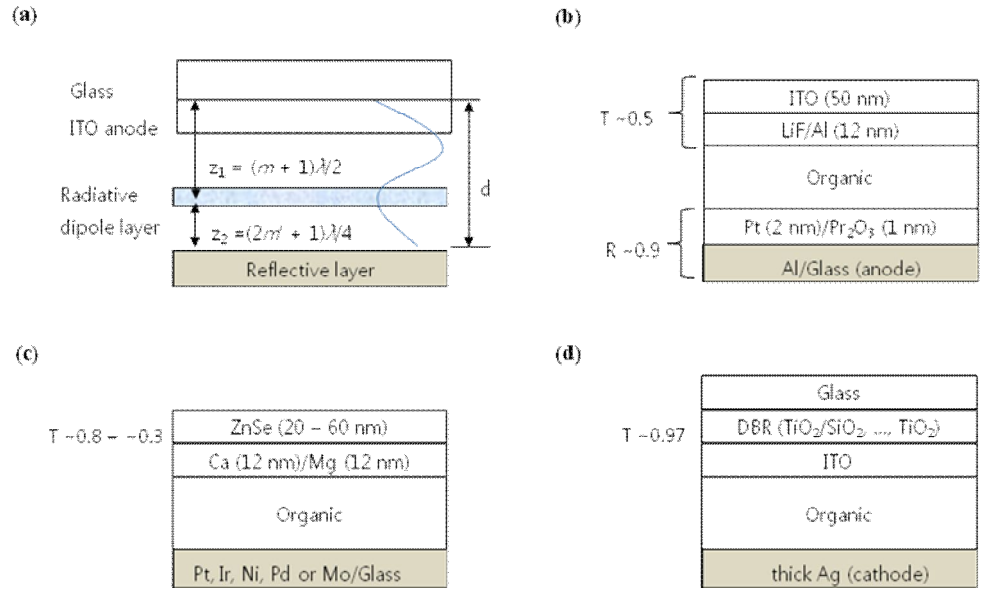

FIG. 1-6. (a) Micro-cavity effect; d is a effective cavity length, and z_1 and z_2 are distances from the emission zone to dominant reflective surfaces. Constructive interference condition for z is expressed with m, m' (m, m' = 0, 1, …) and λ (wavelength). As an example, a wave form is illustrated for the case of m = 1 and m' = 0. Micro-cavities with (b) semitransparent metal and reflective metal oxide, (c) capping layer, and (d) DBR 1-D photonic crystal structure; T, R, and DBR are the transparency, reflectivity, distributed Bragg reflector, reflectivity [Ref. 49,52,53].

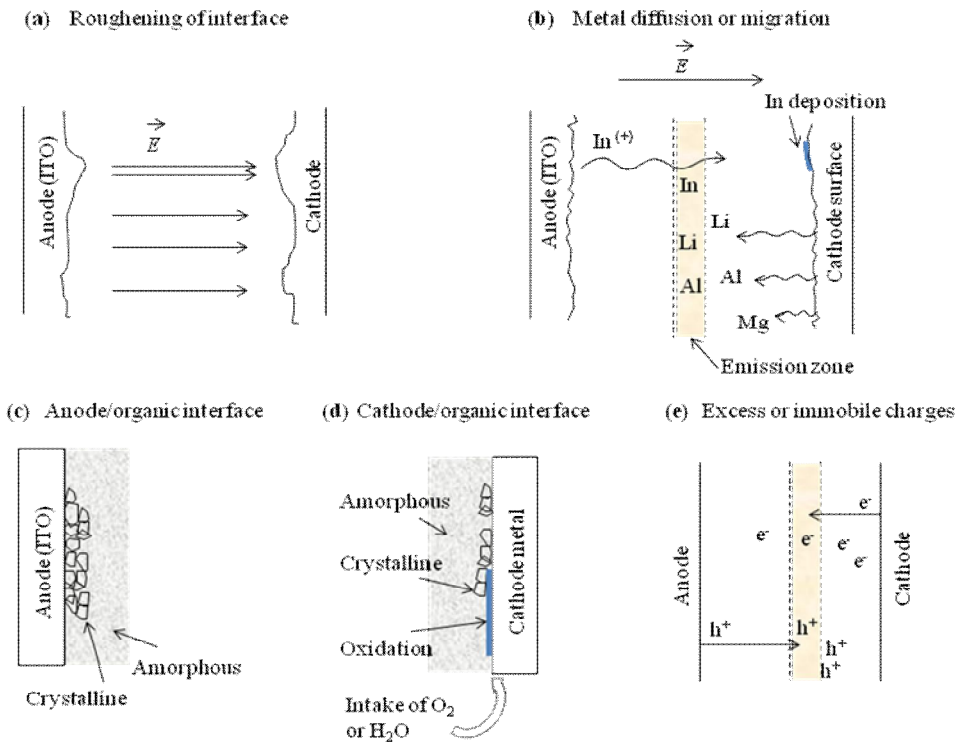

FIG. 1-7. Schematic diagrams for device degradation mechanisms. (a) Concentrated electric field at protruded tips of the rough electrode surface, (b) migration of metallic components of the electrodes, showing their accumulation in the emission zone and some species deposited on the opposite electrode, (c) aggregation/crystallization of an organic material at its interface with the anode, (d) oxidation of the organics or electrode surface at cathode/organic interface through up-taking oxygen or moisture, and (e) excess charges causing unstable chemical species in the electron and hole transport materials, respectively, or immobile charges causing stable effective exciton quenchers.

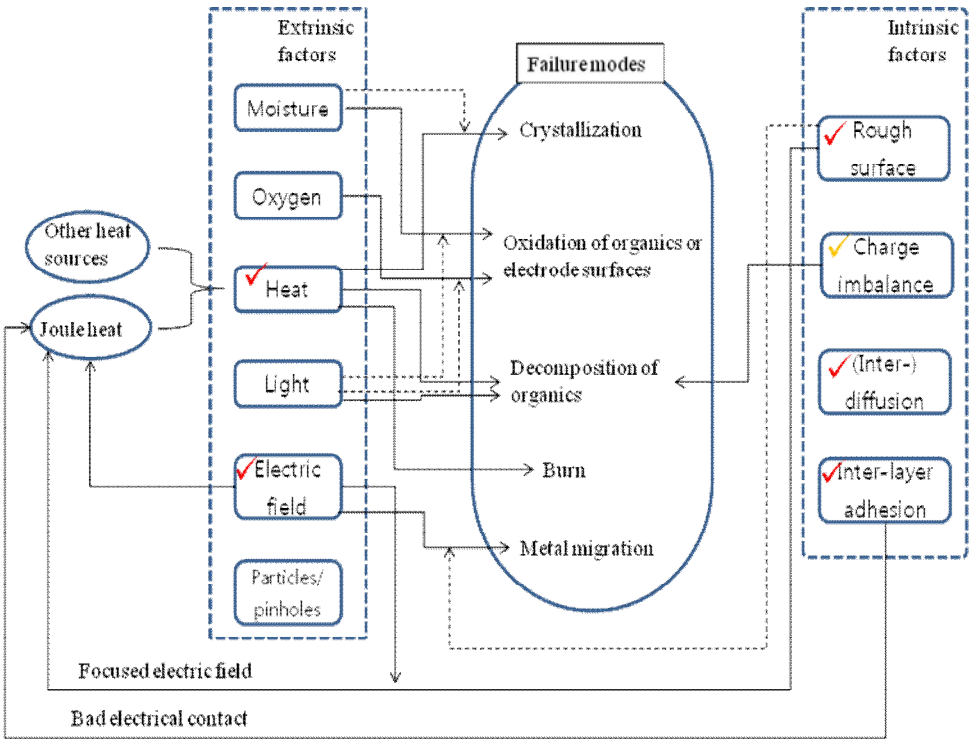

FIG. 1-8. Summary of the degradation factors and modes. Extrinsic factors have been solved through the encapsulation process and particle control in the clean room for fabrication except for the heat and electric field factors. The solutions for the intrinsic factors are intensively related to the interfacial engineering.

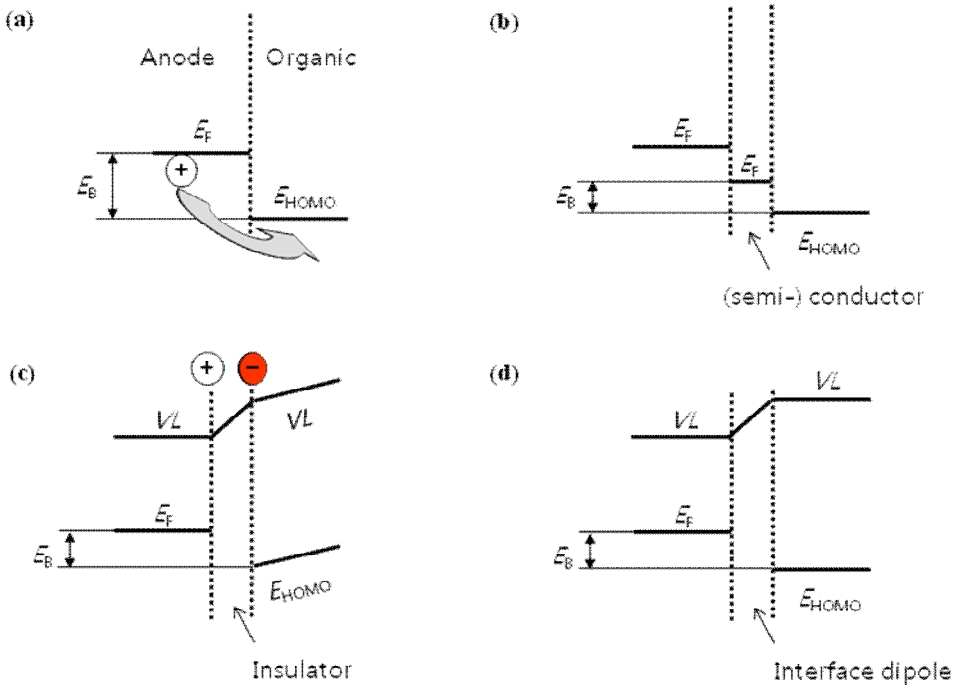

FIG. 1-9. Schematic electronic structures of the anodic side (a) without an interlayer between the anode and organic hole transport layer, (b) with a (semi-) conductive interlayer with a higher work function, (c) with an insulating interlayer under forward bias, and (d) with an interfacial dipole layer.

TABLE I-1. Prevailing conditions for each charge injection or transport mechanism in organic semiconductors. Prevailing or dominant conditions are relatively described. For example, with increasing temperature, both ICLC (injected-charge limited current) and SCLC (space-charge limited current) increase. But ICLC increases at a slower rate, thus, ICLC becomes dominant or a limiting mechanism at high temperature. See text for the abbreviations and symbols.

Current mechanism		Prevailing condition (qualitative)	Equation	Note
Ohmic		lowest E, thick film	$J \propto V/d = E$	Ohmic at reverse bias voltages
ICLC	R-S thermionic	high Φ, high T, low E at contact, (thin film)	$J \propto T^2 \exp\{-(\Phi_B - \beta_{R\text{-}S}E^{1/2})/kT\}$	
	F-N tunneling	high Φ, high T, high E at contact, (thin film)	$J \propto (E^2/(\Phi_B)\exp\{-2\alpha \Phi_B^{3/2}/(3qE)\}$	
SCLC	Shallow trap	low T, low E, moderate thickness	$J \propto V^2/d^3 = E^2/d$	
	TCLC	low T, moderate E, moderate thickness	$J \propto V^{(m+1)}/d^{(2m+1)} = E^{(m+1)}/d^m$	
	Trap-free	low T, high E, moderate thickness	$J \propto V^2/d^3 = E^2/d$	

TABLE I-2. Estimated underlying mechanisms related to the metal halides as electron injection buffer materials; origins of the HOMO level shift and gap-state formation of an adjacent electron transport material, and dissociation of the metal halides. Note: Al-deposition of Alq3 induces destructive interaction and no gap-state formation.

	Origin of HOMO shift	Origin of gap state	Liberation of metal atom	Note
Li, Na, K, Ca, Mg	-	Alq3 anion (doped Alq3)	-	Charge transfer: metal → Alq3
LiF (NaF)	Not clear (LiF-Alq3 interaction?)	Alq3 anion (Al/LiF/Alq3 or Al/LiF/H2O)	Liberation (no liberation in Al/LiF/polymers)	Alq3 anion: passive layer Charge transfer: Al or Na or Li → Alq3
NaCl	-	Alq3 anion? (Al/NaCl/Alq3)	No liberation (Yi *et al.*) Liberation (Kang *et al.*)	Charge transfer: Alq3 → NaCl
CsF	-	-	Liberation in Al/CsF/(PFO or Alq3)	AlF_3, Cs^+polymer
CsCl	Large dipole (CsCl/Al strong dipole)	Alq3 anion? (Alq3/CsCl/Al)	No liberation	CsCl: passive layer
KF	Dipole or K^+ doping (KF-Alq3 strong interaction)	Alq3 anion? (Al/KF/Alq3)	No liberation under Al/KF/Alq3	Charge transfer: KF or Al → Alq3
MgF_2	Dipole or … (MgF_2-Alq3 strong inter.)	Alq3 anion ? (Al/MgF_2/Alq3)	Dissociation unclear	Charge transfer :Alq3 → MgF_2

TABLE I-3. Estimated origins of hole-injection enhancement related to various hole injection layer (HIL) materials.

HIL	(HTL)/HIL/Anode	Origin of enhanced hole injection	Note
Pt	Pt (0.5 nm)/ITO	High work function Wettable on ITO	
Ag_2O, NiO_x	Ag_2O nano-dots, or NiO_x/ITO	High work function	Ag_2O film: p-type Φ ~5.3 eV NiO: p-type Φ ~5.0 eV
IrO_x, RuO_x, NiO_x, VO_x, MoO_3, (CuO_x)	1. Metal oxide/ITO 2. V_2O_5/p-Si	1. Interface dipole (due to large Φ of transition metal oxide: 5 – 7 eV) 2. Band-bending of p-Si	Insulator Wettalbe on ITO surface
Cu phthalocyanine (CuPc), Star-burst amine	1. CuPc or Star-burst amine/ITO	CuPc: Interface dipole → staircase injection level, wettable on ITO surface Star-burst amine: wettable on ITO surface	Organic semiconductor CuPc: promoted crystallization of HTL
CF_x	(NPB)/CF_x/ITO	Interface dipole	UV-cured CF_x: oxygen rich surface & increased conductivity
Phosphonic or phosphoric acid	(NPB)/acid/ITO	Interface dipole: remaining anion on protonated ITO surface and $(NPB\text{-}H)^+$	Compatible with the hydrophobic HTL
Br_2 or I_2	(NPB)/Br_2 or I_2/ITO	Interface dipole (due to large electronegativity)	
Tetrahedral amorphous C	1. (PEDOT)/C/ITO 2. (CuPc)/C/ITO	1. (Enhanced field emission) 2. Tunneling (not effective on UVO-ITO)	Wettable on ITO surface
SiO_2	(NPB)/SiO_2/ITO	Tunneling	Wettable on ITO surface
LiF	LiF or NPB:LiF/ITO	Tunneling (not effective on UVO-ITO)	- Increased thermal stability - LiF:NPB → increased drive voltage
MgF_2	MgF_2 or MgF_2:TPD/ITO	(Tunneling)	- Increased thermal stability

Chapter II

Comparison of ultraviolet-ozone and O_2-plasma surface treatment of an ITO anode in organic light emitting diodes

Abstract

To enhance hole injection, an ITO anode was treated with simple physical pretreatments including ultraviolet-ozone (UVO) cleaning or plasma surface treatments to achieve the highest possible work function of the ITO. Both UVO and plasma treatments probably for the most part remove the ambient contaminants but do not affect the surface morphology. However, the best physical treatment must be clarified and chosen for the industrial application of OLEDs. Here, the effects of the UVO and O_2 plasma surface treatments of the ITO anode on the performance of an OLED device were compared to each other. While the OLED device with the UVO-treated ITO anode showed a relatively low turn-on voltage and less increase in the drive voltage during device operation, the life time of the device was shorter than that with the O_2 plasma-treated ITO, which is in contrast to

a general belief that a lower turn-on voltage is also beneficial for a longer lifespan. Therefore, the origins of the discrepancy between the turn-on voltage and device life time are discussed using surface analysis techniques.

II-1. Introduction

Indium tin oxide (ITO) has been popularly used as an anode in OLEDs because of its good conductivity, wide energy band gap, high work function and transparency in the visible range. In general, as-deposited ITO substrates have been cleaned with organic solvents and then treated with UVO or gas plasma to enhance the ITO surface properties such as the work function and surface energy.

An as-cleaned ITO surface is suspected to have various chemical species such as In/Sn metals (M) and their oxides (M–O–M) or hydroxides (M–OH), as well as residual hydrocarbon contaminant species, shown in Fig. 1 [1,2]. Those species collectively contribute to a change of the work function through the generation of various dipoles. Usually, an asymmetric structure and high polarizability cause higher polarity, leading to higher dipole moments; thus, the oxygen of metal oxides is less polar (i.e., hydrophobic) than its corresponding metal atom because of the symmetric structure of metal oxides [3]. The dangling bond of M–O is highly polar and might be stabilized through resonance with its anionic form through delocalization with an adjacent oxygen despite the high chemical reactivity of the dangling bond, shown in the lower part of Fig. 1(b). On the other hand, the concentration of the hydroxide groups on the ITO surface is considerable, with one OH group/nm^2 of clean ITO surface [4]. The polarity of the hydroxide is thought to be comparable to that of pure metal species because the work function of ITO was found to be independent of dehydroxylation and rehydroxylation by an Ar-bombardment/water-dosing experiment shown in Fig.

1(*b*) [2]. While reducing treatments like H_2 plasma or base treatments increase the drive voltage of OLED devices because of an increase in hole injection barrier through a downward vacuum level shift [1,5], oxidative treatments such as ultraviolet-ozone (UVO) and O_2 plasma are well known to increase the hole injection efficiency.

In the UVO process with oxygen gas and a Hg lamp as a UV source, active oxygen species (oxygen radical, ^3D) and ozone are generated from the oxygen molecule (O_2) under a wavelength of 184.9 nm (6.6 eV, 647 kJ/mol), and the ozone can be further fragmented to form other active oxygen species such as hydroxyl radicals (strong oxidizing agent), and free radicals (^1D) under a wavelength of 253.7 nm (4.8 eV). While organic contamination cannot be easily removed by simple heating, e.g., 300 °C for 3 h [6], active oxygen species (oxygen free radicals, hydroxyl radicals, ozone, etc.) are very effective in oxidizing and removing organic contaminants; ozone is also well known to be very efficient in the fragmenting unsaturated hydrocarbons in the presence of H_2O (i.e. ozonolysis). Carbon on the ITO surface is thought to be oxidized into C–O or C=O during UVO treatment followed by evacuation from the UVO chamber through a vacuum pump. However, the UVO-treated ITO seems to be susceptible to variation in work function; UV irradiation in the presence of environmental contaminants such as water, CO, CO_2, and hydrocarbons can cause a permanent reduction in work function [7], and the energetic secondary electrons induced by the UV irradiation can cause the ejection of the oxygen anion resulting in the attenuation of the ITO work function.

In the O_2 plasma surface treatments, because of the active oxygen species and the large amount of charged oxygen atoms or molecules generated in the plasma condition, hydrocarbon contaminants are effectively removed, which contribute to the high surface polarity by exposing the polar species mentioned above. Especially, O_2 plasma is believed to convert the M–OH or M–OOH into the electron deficient species M–O• (i.e., electron withdrawing and hence negatively charged oxygen) through hydroxide group oxidation chemistry, enhancing the ITO surface polarity shown in Fig. 1(b) [1,2]. The electron deficient oxygen radical can be stabilized through delocalization with the unpaired electrons of the adjacent lattice oxygen atoms. Milliron et al. further proposed that the increase in the ITO work function by other oxidative surface treatments such as UVO, H_2O_2 [8], aqua regia [9], or nitric acid [10] was also attributed to the oxidative conversion of the surface tin (Sn) hydroxide to Sn–O•. From this point of view, the oxidative treatments of highly Sn-doped ITO would be beneficial for the hole injection efficiency. On the other hand, the charged particles in the plasma can make collision-induced high kinetic impacts on surfaces under the electric field of the plasma experimental condition, possibly leading to the structural deformation of the surface in addition to the removal of contaminants adsorbed under a harsh plasma condition.

The effective removal of ambient contaminants with UVO or O_2 plasma treatments is also considered to significantly increase the surface energy and provides better adhesion in the organic layers through reduced interfacial tension between the organic material and the substrate [11]. On the other hand, UVO and

O_2 plasma are somewhat different from each other; UVO is a UV-induced ozone environment whereas O_2 plasma uses radiofrequency-induced oxygen plasma (charged oxygen particles). UVO-treated ITOs are reported to have a trend for a higher work function compared to that treated with O_2 plasma [6]. However, direct comparative studies between UVO and O_2 plasma have rarely been reported yet. Here, the effects of UVO and O_2 plasma treatments on the performance of an OLED device were compared to each other. While the OLED device with UVO-treated ITO showed a relatively low turn-on voltage, the device lifetime was shorter than that of O_2 plasma-treated ITO device, which contrasts to the general belief that a lower turn-on voltage is also beneficial for a longer lifespan [12,13]. Therefore, the origin of the discrepancy between the turn-on voltage and life time was further investigated with surface analysis techniques.

II-2. Experiments

Schematic of OLED fabrication system is shown in Fig. 2, consisted of pretreatment chamber for UVO/plasma surface-treatments and sample-loading/unloading, transfer chamber with a robot arm, deposition chamber with thermal evaporation unit, and glove box (purging gas: 3%-H_2:N_2 mixture) with an attached sample loading chamber. The deposition chamber has inner four partitions for preventing contaminations between source materials during deposition, grouping source materials with similar chemical structure or melting temperature into one partition.

ITO coated glass substrates were cleaned by scrubbing in a detergent and then sonicated in de-ionized water and organic solvents such as acetone and methanol. After rinsing, they were dried with blowing air or N_2 jet. Finally the sample was subjected to inductively coupled O_2-plasma cleaning (radiofrequency power of 100 – 150 W, typically 150 W) for 1 – 5 min (typically 5 min) under a pressure of 50 mTorr oxygen ambient in the pretreatment chamber, or UVO treatment (150 mW) for 10 min by using low pressure quartz mercury vapor lamp (UV emission of 185 nm) attached to the same chamber. The organic layers and the cathode layers were deposited onto the ITO substrate by conventional resistive heating vapor deposition with the substrates maintained at ambient temperature under a base pressure of ~5 × 10^{-7} Torr. The thicknesses of thin films are monitored with quart crystal microbalance (QCM) sensors. Due to the difference between distances of QCM and sample from source materials, the sensor must be calibrated with tooling factor (T), which is calculated by the ratio of the distance between source and thickness sensor ($D_{\text{source-QCM}}$) to the distance between source and sample substrate ($D_{\text{source-substrate}}$):

$$T = \frac{D_{source-QCM}}{D_{source-substrate}}. \qquad (1)$$

For more accurate determination of thickness, in the present work, QCM was further calibrated through X-ray reflectivity (XRR) thickness measurements. Thus, the final calibrated tooling factor (T_f) is simply related with the T_i as following equation:

$$T_f = \frac{T_i\left(Th_{measured-XRR}\right)}{Th_{nominal}}, \quad (2)$$

where $Th_{measured\text{-}XRR}$ and $Th_{nominal}$ is a thickness value measured by XRR and nominal thickness value displayed by QCM before calibration, respectively.

N,N'-bis(naphthalene-1-yl)-N,N'-bis(phenyl)benzidine (NPB), tris(8-hydroxyquinoline) aluminum (Alq_3), and LiF were used as hole transport, electron transport and electroluminescent layer, and electron injection layer material, respectively. The chemical structure of NPB and Alq3 are shown in Fig. 3(a) and (b). The organic materials were deposited slowly at a rate of less than a few Å/sec after preheating the source materials for ~30 min below their evaporation temperatures. After the organic deposition and electrode metallization with Al, the OLED-deposited substrate was moved into the glove box for encapsulation process which is for the protection of OLED device from penetration of ambient water vapor or oxygen gas. The OLED device of architecture of ITO/NPB (70 nm)/Alq3 (60 nm)/LiF (0.5 nm)/Al and the prepared sample patterns are illustrated in Fig. 1(c) and (d), respectively. Current density-voltage-luminance (*J-V-L*) characteristics were measured with Keithely 238 source measure unit and PR650 luminance meter (Photo Research) in front of a light-emitting active area. Voltage-luminance-time (*V-L-t*) characteristics were obtained under the aging condition of a constant current of 50 mA/cm^2 by using a lifetime measurement system (Mac Science Inc.).

For surface characterization, the ITO substrates cleaned or surface-treated as above were stored in a vacuum desiccator and transported under vacuum

packaging, and exposed only briefly to the air before loaded into a ultrahigh vacuum (UHV) chamber equipped with a He discharger lamp for UPS and also with X-ray sources, or into a high vacuum chamber for scanning electron microscope (SEM) measurements. The base pressure of the UHV chamber was 2×10^{-10} Torr which rose to high 10^{-9} Torr range during UPS measurements mainly due to backfilling of the He gas. For UPS, He I discharge at 21.22 eV (i.e., 58.48 nm of vacuum UV energy) was used and the energy resolution was 0.1 eV. Although the UV energy is relatively very low compared to that of X-ray, the cross-sections for photoemission are much larger and the peak width is narrower, resulting in much greater signal intensity and more discernible features in UPS than in X-ray excited valence band spectra. The spectrum was taken for −10 V sample bias for clearing the inelastic signals from the spectrometer (i.e., to separate the secondary electron cut-offs from the sample and spectrometer which otherwise overlapped) [14]. As shown in Fig. 4, the binding energies of the emitted electron from a conductive sample surface by UV or X-ray irradiation can be calculated with the following Einstein equation:

$$E_b = h\nu - E_k' - \phi_{\text{spec.}}, \tag{3}$$

where E_b is the electron binding energy, $h\nu$ the energy of the incident photon, E_k' the electron kinetic energy detected from the spectrometer, and ϕ_{spec} the work function of the detector material. When a sample surface is not sufficiently electrically conductive, positive charges build up, lowering the Fermi level of the sample surface relative to that of the spectrometer. Additionally, the Einstein equation can be modified to consider the surface charge energy (E_{ch}): $E_b = h\nu - E_k'$

$- \phi_{spec.} - E_{ch}$. Because of the variation in the surface charging energy during the experiments and the floating Fermi level, peak-broadening and peak-shifts are present and the binding energies of a sample are, generally, calibrated with an internal reference, e.g., C 1*s* at 285.0 eV. The work functions of the sample surfaces can be calculated with the spectroscopic data and the Einstein equation in the case of no surface charging effects by considering the photoelectron processes originating from (1) the Fermi level and (2) the secondary cut-off level shown in Fig. 5:

$$h\nu\,(1) = E_{k,F}' + \phi_{spec} - E_{bias}, \tag{4}$$

$$h\nu\,(2) = (E_{SCO} - E_F) + (\phi_{spec} - E_{bias}) + E_{k,SCO}', \tag{5}$$

thus

$$E_{SCO} - E_F = E_{k,F}' - E_{k,SCO}'. \tag{6}$$

Therefore,

$$\begin{aligned} \phi_{sample} &= h\nu - (E_{SCO} - E_F) \\ &= h\nu - (E_{k,F}' - E_{k,SCO}') \\ &= h\nu - W, \end{aligned} \tag{7}$$

where E_F, E_{SCO}, ϕ_{sample}, ϕ_{spec} and E_{bias} correspond to the Fermi level, secondary cut-off level, work function of a sample surface, work function of the detector of the spectrometer, and applied bias energy, respectively. $E_{k,F}'$, and $E_{k,SCO}'$ are the kinetic energies of the photoelectrons detected at the spectrometer, originating from the Fermi level and secondary cut- off level, respectively. W is the energy difference between the Fermi and secondary cut-off levels. The photoelectron emission features corresponding to the electron density of states (DOS) appear on

the background signals of the secondary electrons induced by the excitation of lower binding electrons.

The Mg $K\alpha$ line at 1253.6 eV was used in XPS and the energy resolution was ~1.1 eV. The XPS signal intensity (I) can be expressed as following equation:

$$I = nf\sigma\theta y\lambda AT$$

$$= nS, \quad (8)$$

where I, n, f, σ, θ, y, λ, A, and T denote the photoelectron intensity [counts/sec], atomic concentration [atoms/cc], X-ray flux [photons/cm^2-sec], photoelectric cross-section for an atomic orbital of interest [cm^2], X-ray angle coefficient (namely, orbital angular symmetry factor, 1 at 54.7° between the X-ray source and detector from a sample surface), photoelectron process efficiency, photoelectron mean free path, sample area, and detection efficiency, respectively. S is defined as atomic sensitivity factor (ASF), $S = f\sigma\theta y\lambda AT$. For practical methodology to evaluate surface atomic concentration, relative atomic concentration (C) is adopted through the following equation.

$$C_x = \frac{I_x / S_x}{\sum I_i / S_i}$$

$$= \frac{(I_x / S_x) / S_R}{(\sum I_i / S_i) / S_R}, \quad (9)$$

where the subscript of x, i, or R denotes the atomic constituent of a sample surface. S_x or S_i would be referenced to S_R in the form of S_x/S_R or S_i/S_R, respectively, namely relative atomic sensitivity factor (RSF), and thus the RSF is nearly independent of sample matrix and signal detection system. Generally, ASF of F 1s is used as a

reference (S_R) for the tabulated RSF values of atoms.

All photoemission data were evaluated with Igor Pro software (Wavemetrics). For morphological investigation, SEM and atomic force microscope (AFM) measurements were carried out.

II-3. Results

Figure 6 exhibits the *J-V-L* characteristics of the devices with the structures of ITO/NPB (70 nm)/Alq3 (60 nm)/LiF (0.5 nm)/Al with different physical surface cleaning process of ITO: one treated with UVO (device B) and the other with O_2 plasma (device C). Device A is an as-cleaned reference sample without UVO or O_2 plasma treatments of ITO, denoted as "no treatment". The UVO and O_2 plasma treated samples show larger current density than no treated one. Furthermore, the current density of device B is higher than that of device C at the same voltages, indicating that the hole injection efficiency of each device is in the order of (UVO) > (O_2 plasma) > (no treatment). For example, as compared at a current density of 50 mA/ cm^2, the device B shows a driving voltage of 5.47 V while the device C and A 5.72 V and 7.45 V, respectively. However, from the *L-J* curve of Fig. 3(b), luminance intensities at the same current density are found to be in the order of (no treatment) > (O_2 plasma) > (UVO), inverse order of the hole injection efficiency above. It seems that the charge balance at the electroluminescent center is broken more severely with the increase in hole injection efficiency at the interface of anode and hole transport layer.

To evaluate the effects of the surface treatments on the operational stability, *L-V-T* characteristics of the OLEDs with the surface-treated ITO are compared to those of the reference (no treated ITO). Figure 7 shows the luminance and voltage changes measured during device operation at a constant current density of 50 mA/cm^2. The decay times by the 60% of initial brightness (L_0) are 30 h, 226 h, and 9 h for the device B (UVO treated ITO, L_0 = 1349 cd/m^2), C (O_2 plasma treated ITO, L_0 = 1410 cd/m^2), and A (no treated ITO, L_0 = 1816 cd/m^2), respectively. For the life comparison between the devices at the same brightness, each value can be estimated from the assumption of the scalable law of Coulombic degradation [15]. The projected 60% life under the initial luminance of 100 cd/m^2 (a prototypical desktop display luminance) is 404 h for the device B, which is higher than that of device A (163 h) but much lower than that of device C (3,187 h). From Fig. 7(b), the voltage change of device B after the operation time of 40 h is 0.56 V, which is much lower than that of device A (2.45 V) and slightly lower than that of device C (0.62 V).

Table I exhibits the summarized values of driving voltages, initial luminance, current efficiencies, power efficiencies, external quantum efficiency and 60% lifetimes of the devices A, B, and C, operated at a constant current density of 50 mA/cm^2. In general, current efficiency does not reflect the degree of charge balance at the electroluminescent center due to different charge-loss paths such as leakage current or non-radiative decay of excitons. However, when device architectures are not significantly different from each other as here, the degree of charge balance is thought to be in the same order of the current efficiencies:

(device A) > (device C) > (device B). A similar explanation is possible for the tendency of the external quantum efficiency: since the UVO or O_2 plasma treated ITO anode enhances hole injection from the anode to the NPB, the larger number of holes is expected to reach the carrier recombination center than electron, thus an excess number of holes in the carrier recombination zone causes the decrease in the external quantum efficiency [16]. The charge balance of electrons and holes in the recombination zone is critical to both current efficiency and device stability [17,18], especially for Alq_3-based OLEDs [13]. Charge balance might be easily broken due to the higher hole mobility of NPB overwhelming the electron mobility of Alq_3 by up to two orders of magnitude [19]. Therefore, the charge balance can be improved by introducing an ETL with higher electron mobility. Although the current efficiencies of the device B and C are lower than that of device A, the power efficiencies are higher due to the reduction of driving voltages. In contrast to the general belief that the lifetime increases with the increase in power efficiency, the power efficiency does not explain the tendency of life time variation observed here because the lifetime of device C is tremendously larger than that of device B even though the power efficiencies are comparable to each other.

The origin of driving voltage lowering and life span elongation of OLED device is highly related with injection barrier and compositional changes at the ITO/organic interface. Fig. 8 shows the full ultraviolet photoelectron emission spectra of variously surface-treated ITO in binding energy scale. The spectra imply some revealing characteristics of ITO's electronic structure. Generally, degenerate semiconductors would be expected to display photoelectron emission from the

filled valence band, followed by a gap and then emission from conduction band populated by the *n*-type donor states. However, there is no indication of a gap between emission at the Fermi level and the onset of the oxygen 2*p*-like valence band. Origin of the absent gap is attributable to the high doping level to completely fill the gap of the impurity bands. Further the Fermi edge did not readily show up for some samples maybe due the low free carrier density of ~2 x 10^{20} cm^{-3} [20–22], about two orders of magnitude lower than a typical metal, which are, however, not problematic because the Fermi edge is referenced to the energy scale and should not change from sample to sample as long as grounded. The spectrum width is determined from the distance between the sample inelastic cutoff and the Fermi edge. These edges are ideally infinitely abrupt but they are broadened owing to the limited spectrometer resolution and thermal effects. To account for the analyzer broadening (± 0.1 eV [1]), 0.1 eV was added to the work function values which are taken as the excitation energy minus the spectrum width. The deep valley between the cut-off and the valence band emissions indicates low concentrations of carbon on the sample surfaces [7]. Generally, the work function is also sensitively affected by the surface compositional change [23]. Significant surface contamination by carbon is common with smaller amounts of nitrogen and sulfur. Thus, the atomic concentrations of In, Sn, O, and C were determined from the measured XPS peak intensities and the reported relative atomic cross sections [24]. The atomic concentration obtained in this way typically has an accuracy of ~15% and reproducibility (i.e. precision) of ~2%. Moreover, the carbon contaminants usually exist in (partially) oxidized states, confounding attempts to obtain the accurate

amount of oxygen bound to In and Sn. Therefore the XPS data will serve only as a qualitative guide when comparing results from different samples. Further notable knowledge is that the concentration is determined by the intensity of XPS with a probing depth of about 3–4 nm while the work function is determined by a thinner layer at the surface [25], and thus the change in concentration may not be reflected by that in work function. Table II summarized the results of work functions, chemical compositions in atomic %, and compositional ratios.

Observed as shifts of the secondary cutoffs in Fig. 8, the work functions of the ITOs were on the order of (UVO-treated ITO, 5.3 eV) > (O_2 plasma-treated ITO, 5.1 eV) > (no-treated ITO, 4.3 eV), which means the injection barrier was lowered in the same order, resulting in the corresponding lowering of the driving voltages of the OLED devices shown in Fig. 6(a). From the XPS results in Table II, the concentration of carbon, considered as a residual organic contaminant indicator, obviously decreased after the surface treatments of ITO, especially after the O_2 plasma treatment. To investigate the intrinsic compositional change of the ITO surfaces, the concentrations of the ITO ingredients (In, Sn, and O) without carbon and their ratios were compared shown in the parentheses and right three columns of Table II. Different from the sputtered ITO [6], the UVO- or O_2 plasma-treated ITO does not show any substantial compositional changes in the intrinsic ITO surface except for Sn, for which the surface concentration seemed to decrease after the UVO treatment revealed by the values for the Sn/In ratios, from 0.158 to 0.151. The decrease in the Sn/In ratio has been frequently observed in various surface treatments including ion sputtering and heating [6,23,26,27]. From the ratios of the

O/In and O/(1.5In +2Sn), the difference between the oxygen concentrations of the samples is very slight. Additionally, from the values for the O/(1.5In +2Sn) larger than unity, the samples were found to be oxygen-rich compared to the perfectly stoichiometric ITO [28].

Morphological changes of the ITO surface can also affect the performance of OLED devices. Especially, the rough surface with spikes on the ITO surface can cause localized high electric field, leading to electric shorts [29]. Root mean square roughness values from AFM results (images not shown here), however, are 10.05 (no-treatment), 9.60 (plasma), and 8.05 (UVO) Å, implying slight reduction in the surface roughness after the oxidative surface treatments. Therefore, UVO or plasma treatments largely removed the ambient carbon contaminants and slightly modify the surface composition of the ITO without significant change of the surface morphology or surface roughness, though a sputtering with more than a few hundred eV/particle could modify the surface morphology through the preferential sputtering of oxygen or Sn [23,26].

II-4. Discussion

To clarify whether the devices are hole-rich or hole-deficient at the electroluminescent center, the degree of charge balance is displayed as a schematic curve in a 2-dimensional diagram shown in Fig. 9. The degree of charge balance is reflected in the current efficiency because our devices have similar charge loss paths with each other because they have the same device architecture except for the different surface treatments of the ITO anodes. The current efficiency decreased as

the hole injection efficiency increased shown in Fig. 6. Therefore, the degree of charge balance for the prepared OLED devices decreases as the hole injection efficiency increases (namely, the increase in the number of holes at the electroluminescent center) and thus the assigned positions for the samples on the curve should be interconnected as an negative slope. Two possible assignments are derived: one sequential positioning as 1, 3, and 4, and the other as 2, 3, and 4, for device A, C and B, respectively. Therefore, although it is unclear whether the reference is hole-rich or hole-deficient, devices B and C are found to be hole-rich at the electroluminescent center.

The increased hole injection efficiency as well as being hole-richer at the emission centers seems to be mainly because of the removal of carbon contaminants on the ITO surface through the UVO or O_2 plasma cleaning resulting in an increase in the ITO work function. As the work function of ITO increases, the hole injection barrier decreases accordingly. The decreased injection barrier would lead to a decrease in the driving voltage because the current across the interface is proportional to the negative exponent of the barrier height in the injection-limited regime [30]. The decreased work function in the carbon contaminated ITO surface can be explained as a downward shift of the vacuum level. The origins of the dipole moments are explained by various factors such as charge transfer between the ITO and NPB, image effect (i.e., mirror force), rearrangement of the electron cloud at the ITO surface (i.e., tailing part of the electronic cloud at the ITO surface pushed back by repulsion with the electron cloud in the adsorbate), chemical interaction, interfacial states, and permanent dipole through adsorption of polar

functional groups, summarized with schematic diagrams in Fig. 10 [31]. Among them, the contribution of the surface electron tail should be reduced because ITO like other metal oxides has fewer free electrons ($\sim 10^{20}/cm^2$) than that of metal ($\sim 10^{22}/cm^2$) [32]. Dipole moments and their corresponding vacuum level shifts are denoted in each case. Because electric field in the dipole is constant, the potential energy of the vacuum level is linear with distance. The schematic energy level diagrams of the ITO/NPB surface with various ITO surfaces are shown in Fig. 11, with the expected dipole moments. As-cleaned ITO surface is believed to have many hydroxyl groups as mentioned above, and thus, the hydrogen of the hydroxyl group may react with NPB nitrogen leading to a vacuum level downward shift forming inward negative dipole moments (i.e., negative change of the work function, following the convention of surface science) when NPB is deposited on the ITO surface shown in Fig. 11(a) [5,33,34]. When the ITO surface is contaminated with hydrocarbons, the work function of the ITO should increase from the insulating property of the organic contaminants. However, the organic contaminants have lower polarity from their additional covalent bond features; therefore, less dipoles are exposed. Furthermore, the electron withdrawing polar nature of the ITO surface will be expressed in the insulating layer, leading to the lowering of the vacuum level shown in Fig. 11(b). Accordingly, the HOMO level of the following NPB will be shifted downwardly and hence, the hole injection barrier increases. For comparison, an upward shift of the vacuum level through the adsorption of electro-withdrawing moieties or the generation of electron deficient sites/species through oxidative surface treatments including O_2 plasma and UVO as

mentioned above is also represented for the case of the M–O• species (i.e., electron withdrawing thus negatively charged oxygen) on the ITO surface in Fig. 11(c). And thus, with the removal of carbon after the UVO or O_2 plasma treatment, vacuum levels shift upwardly, as indicated from the secondary edges in Fig. 8. Although a more effective removal of the carbon concentration was observed with the O_2 plasma-treated ITO, the work function was still higher in the UVO treated-ITO. Thus, other compositional changes might have significant roles.

Because ITO is a Sn-doped *n*-type semiconductor through the substitution of the four valent Sn for three valent In and one electron of Sn is in the conduction band (i.e., one electron donor level), the carrier density of the ITO decreases with the decrease in Sn through a reduced electron density in the conduction band, and thus, the Fermi level moves downwardly resulting in an increase in the work function shown in Fig. 12(a) and (b) [35]. Therefore, the greater increased work function of the UVO treated-ITO than that of the O_2 plasma-treated ITO can be explained by the significantly decreased Sn concentration. Furthermore, the decreased conductivity of the ITO surface induced by the decrease in the Sn concentration may enhance the potential drop under bias and thus favor hole injection from the ITO.

On the other hand, the effect of the oxygen component on the rise in work function has been thought to be from an upward shift in the vacuum level through the generation of outward facing negative dipoles, shown in Fig. 12(c), such as an almost universal effect in oxygen adsorption on metals [36], while the ejection of oxygen from the ITO surface probably from the influence of the energetic

secondary electrons or charged particles during the UV irradiation or plasma discharge [27,37,38] is suspected to depress the work function by forming oxygen vacancies (two trapped electrons per vacancy) in the donor states which could then cause an upward shift of the Fermi level of the ITO [39]. However, the O/In ratios obtained are virtually constant at the present error range; although the oxygen concentration of the O_2 plasma-treated ITO is less than that of the UVO-treated one, the difference seems to be not so significant. Therefore, when comparing with device C (O_2 plasma-treated ITO), the lowering of the driving voltage of device B (UVO treated-ITO anode) is expected to be attributed to the increased work function and decreased surface conductivity of the ITO caused by the relatively greater decreased Sn surface concentration rather than by the carbon contaminants which were richer in the UVO treated-ITO and otherwise could cause less increase in the ITO work function compared to the O_2 plasma-treated ITO in this work.

The enhanced hole injection efficiency through the increased work function of ITO also seems to be reflected in the result of the ΔV-t characteristics in Fig. 7(b). The increase in the driving voltage during device operation is thought to mainly originate from the disruption of the ITO/HTL interface because of joule heat. A lipophilic arylamine such as NPB was shown to undergo decohesion on the hydrophilic oxide (i.e., ITO) surface under mild heating [40]. ITO has a bixbyite crystal structure with a hydrophilic native (hydroxylated) oxide surface (advancing aqueous contact angle ~0–30°) while a typical HTL, NPB, is hydrophobic with advancing aqueous contact angles of ~90°, which implies that the large surface energy mismatch at the ITO/NPB interface introduces an intrinsic micro-structural

instability and will cause interfacial decohesive forces under the influence of localized resistive heating at/near the glass temperature of NPB. As shown in Fig. 13, the device structures before and after the degradation are compared to the assistance of corresponding simple equivalent electric circuits under an applied forward bias with a constant current density. The joule heat generated during the operation can cause the aggregation or crystallization of NPB, making the lattice and surface energy mismatches at the NPB/ITO interface a significant factor for interfacial stability; thus, disrupted contact areas between NPB and ITO would be generated via joule heat-induced crystallization of the organic material, resulting in a decreased area of hole injection from ITO into NPB, shown in Fig. 13(b). Thus, the electrical resistance (R) between anode and cathode increases because of the decreased conduction paths: $R_1 < R_2$. Additionally, the applied voltage (V), defined as IR, is also increased under the constant current source ($I_1 = I_2$, here 50 mA/cm^2): $V_1 < V_2$. It means that both a higher electric filed and higher current density are applied on relatively well-remaining contact areas after the disruption of the interface. Therefore, the device degradation mechanism from the increase in the hole injection barrier is explained in Fig. 14. The increased injection barrier would increase the joule heat at the interface of the ITO and NPB, which accelerates the aggregation/crystallization of NPB to cause a disruption in the ITO/NPB contact. And thus, the current would bypass the disrupted contact regions, causing a higher electric field and current density focused on the still contacted areas of NPB and ITO under the condition of an external constant current density of 50 mA/cm^2. The increased local electric field would increase the joule heat further, repeating the

degradation cycle above. It is noteworthy that the possibility of electric shorts from a high local electric field is excluded because, in this work, no significant increase in the leakage current with operation time was observed under a reverse applied bias voltage. Thus, the steep increase in the drive voltage of device A with the operation time, even with relatively higher initial charge balance, is mainly because of the aggregation/crystallization of NPB and the disruption of NPB/ITO contact from joule heat induced by a higher hole injection barrier [35]. The device degradation through disruption of the electrical contacts at the electrode/organic interface caused by joule heat would be mitigated under the decreased hole injection barrier and hence decreased drive voltage condition of devices B and C, leading to a reduced increase in the driving voltages with the electrical stress time. Moreover, device B with the UVO treated-ITO shows a slightly but clearly less increase in the driving voltages with the operation time than that of device C, reflecting the contribution of the slightly lower hole injection barrier in device B.

Meanwhile, the luminance decrease with the operation time is intrinsically related to the breakdown of the charge balance condition during operation. Excess charges from the broken charge balance can cause detrimental effects on device performance such as chemical degradation of Alq3 because of unfavorable hole uptake [13,17,18], or charge traps serving as non-radiative centers [41] or deterrents of charge mobility [42]. The further generation of excess charges during operation might be caused by charge carrier mobility changes with an increase in the device temperature, shown as a proposed mechanism in Fig. 15. Temperature dependence of the charge mobility in semiconductors has been reported [43]. Heat

generated during device operation would cause mobility change for both the hole and electron in different manners from each other because of their different effective masses and phonon scattering times, leading to a worse charge-balanced condition or to a better balanced condition. The latter is frequently observed experimentally as an initial luminance increase (namely, forming period) in the *L-t* curve [44], although the origins have not been clearly verified. In any case, it is hard for the charge balance to remain at the apex of the charge balance curve shown in Fig. 9 under the variable condition of charge mobility. Once the charge balance is broken or decreased, the excess carriers would adversely affect device stability; especially, the excess hole in hole-rich devices, as in this work, will facilitate the degradation of Alq3. Cationic species of Alq3 initially accumulate at or near the NPB/Alq3 interface and oxidation seems to occur over the bulk of Alq3 [41]. This oxidation process of Alq3 from incoming excess holes causes non-radiative centers, and seems to reduce electron mobility in the ETL, causing further breakdown of the charge balance and subsequently accelerating device degradation shown in the upper cycle of Fig. 15. The fixed and accumulated cations might decrease the charge transportation [41], leading to an increase in the driving voltage and the subsequent ohmic heating; thus, another possible degradation cycle, shown in Fig. 14, is formed.

Therefore, the origins of luminance decrease with electrical stress for each device are summarized as follows. (1) In the case of the device with no-treated ITO, because the device shows the highest initial charge balance among the samples, the fast luminance decrease or charge balance breakdown with the operation time is

mainly attributed to the higher joule heat generation at the ITO/NPB interface. (2) When comparing devices B and C, the unexpectedly faster decrease in luminance with the operation time of device B (UVO-treated ITO anode) implies that mechanistic origins other than the joule heat at the interface of the ITO and NPB must be considered because device B shows a slightly lower hole injection barrier and thus a lower increase in the driving voltage with the operation time (therefore, a lower joule heat) as explained above. However, device B is initially slightly less charge-balanced and considered to be at the step of "worse charge balance" in Fig. 15 and the device degradation is quickly accelerated in the degradation cycle while device C is at the step of "better charge balance" and device degradation would be retarded. However, the slight difference of the initial charge balance between devices B and C seems not to be enough to explain the large difference in *L-t* curves of the devices. More carbon contaminants in the device B might be the origin for the fast decrease of the luminance, of which mechanism is unclear.

On the other hand, the excess charges from the charge imbalance might be another heat source, as namely hot carriers. The hot carrier effect is well known to detrimentally affect the device performance and stability of semiconductors, especially in the field of MOSFET (Metal Oxide Semiconductor Field Emission Transistor) by formation of the space charge (volume charge) within the insulator(s) or interface states at the semiconductor/insulator interface through chemical reaction(s). In general, under weak electric fields, the behavior of charge carriers can be described by Ohm's law (namely a linear proportional relationship between drift velocity and electric field), but Ohm's law breaks down at electric

fields exceeding 10^4 V/cm, such as in semiconductor devices, making analytical descriptions difficult [45]. Under a high electric field, carriers can acquire so much energy that their kinetic energy exceeds that of the lattice, leading to the generation of hot electrons. In OLED devices, the charge carriers are under a high electric field, e.g. ~4×10^4 V/ for drive voltage of 5 V in this work.

In Fig. 16, the process of hot carrier generation during device operation is proposed by showing a schematic of the light emission process of an OLED based on simple electronic structure diagrams with the assumption of a common vacuum level alignment. ITO is a degenerate *n*-type semiconductor from a high electron concentration of ~$10^{20–21}$/cm^3 [20–22]. The work function of ITO and the ionization potential and LUMO levels of the organic materials are referenced from previous reports [37, and therein]. The electronic structural variation induced by LiF at a sub-nanometer thickness is not considered for brevity. In the absence of external forward bias, holes from ITO and electrons from Al have difficulty moving toward each other. Under the bias applied, holes and electrons are injected from the electrodes and self-localize to generate positive and negative polarons, which are transported through the HOMO edge of Alq3 and NPB and through the LUMO edge of Alq3, respectively; thus, the transport mechanism is mainly based on hopping rather than appreciably dispersed electronic bands, only achievable for highly crystalline defect-free samples. It is notable that because of the strong difference in the charge carrier mobility between NPB and Alq3, the voltage drop at Alq3 will be much higher than at the NPB layer, thus showing an accumulation of injected positive carriers (i.e., holes) at the organic interface [43]. When two

oppositely charged polarons encounter each other at the interface of NPB and Alq3, they can form bound electron-hole pairs (i.e., excitons) which can emit light (here, green) via exciton annihilation (through the recombination of electrons and holes). Some excess carriers of electrons or holes could pass over the emitting interfacial region without generating the excitons, resulting in the arrival at their counter electrodes. The electron encountered ITO anode and hole encountered Al cathode would have high kinetic energies from the lowering of the corresponding potential energies at their counter electrodes, leading to the generation of hot carriers. Although the hot carrier effect has rarely been reported in OLED devices, breakage of the charge balance would generate many hot carriers, and thus limit the long term stability of the device; hot holes (or hot electrons) are expected to couple with phonons from their high kinetic energy induced by the high effective temperature rather than to cause the formation of excitons, resulting in the generation of positive (or negative) polarons which can then be annihilated via heat dissipation, namely, the emission of phonons. Consequently, the effect of hot carriers would be manifested as an increase in the heat of the OLED device, accelerating the degradation of the organics. Therefore, the fast degradation of device B might be ascribed to the hot carrier effect from the lower degree of charge balance compared to device C. However, experimental observations of hot carrier effects in OLED devices are needed through further investigations with clear evidence of hot carriers. In some device architectures, a hole (or electron) blocking layer has been reported to be adopted in the cathode (or anode) side to accumulate holes (or electrons) in the emitting layer (e.g., 2,9-dimethyl-4,7-diphenyl-1,10-

phenanthroline (BCP) hole blocking layer [46]).

II-5. Conclusions

After UVO or O_2 plasma surface treatments of ITO, its work function increased tremendously mainly by the removal of hydrocarbon contaminants, resulting in the enhanced hole injection efficiency, and thus, the operation voltages of the OLED devices were lowered. However, the slightly higher work function of the UVO-treated ITO compared to that of the O_2 plasma-treated ITO could be ascribed to the decreased Sn concentration which causes a downward shift in the Fermi level. The hole injection barriers are also reflected in the drive voltage changes with the device operation time, based on a possible mechanism that organic crystallizations are accelerated by the joule heat at the hole injection interface. The OLED device with no-treated ITO has a very fast decrease in luminance with the operation time possibly through joule heat-induced degradation because of its high hole injection barrier. Although the OLED device with the UVO treated-ITO has a lower drive voltage because of its lower hole injection barrier and a higher electric field induced by the decreased surface conductivity of ITO from the decreased amount of Sn caused by the UVO treatment, the device has fast degradation compared to the device with the O_2 plasma-treated ITO. Therefore, a proposed degradation mechanism is the charge balance breakdown mainly from the higher hole-excess in the device with the UVO treated-ITO, rather than joule heat at the hole injection interface. The higher hole-excess makes the device enter the degradation cycle

faster based on chemical decomposition, e.g. Alq3 here. Additionally, hot carrier effect from the excess holes also can be issue from the excess carriers which needs to be further investigated. Based on the observed higher carbon contaminants in the UVO treated-ITO, carbon residues could be another origin of the fast degradation, of which mechanism is still unclear.

References

[1] Z. H. Huang, X. T. Zeng, X. Y. Sun, E. T. Kang, J. Y. H. Fuh, and L. Lu, *Org. Electron.* **9**, 51 (2008).

[2] D. J. Milliron, I. G. Hill, C. Shen, A. Kahn, J. Schwartz, *J. Appl. Phys*. **87**, 572 (2000).

[3] J. S. Kim, F. Cacialli, and R. H. Friend, *Thin Solids Films* **445**, 358 (2003).

[4] S. K. Vanderkam, E. S. Gawalt, J. Schwartz, and A. B. Bocarsly, *Langmuir* **15**, 6598 (1999).

[5] Q.-T Le, E. W. Forsythe, F. Nüesch, L. J. Rothberg, L. Yan, and Y. Gao, *Thin Solids Films* **363**, 42 (2000).

[6] Y. Park. V. Choong. Y. Gao, B. R. Hsieh, C. W. Tang, *Appl. Phys. Lett*. **68**, 2699 (1996).

[7] R. Schlaf, H. Murata, Z. H. Kafafi, J. Electron Spec. Relat. Phen. **120**, 149 (2001).

[8] T. Osada, T. Kugler, P. Bröms, and W. R. Salaneck, *Synth. Met.* **96**, 77 (1998).

[9] J. S. Kim, M. Granström, R. H. Friend, N. Johansson, W. R. Salaneck, R. Daik, W. J. Feast, and F. Cacialli, *J. Appl. Phys*. **84**, 6859 (1998).

[10] F. Nüesch, L. Kamarás, and L. Zuppiroli, *Chem. Phys. Lett.* **283**, 194 (1998).

[11] J. S. Kim, R. H. Friend, and F. Cacialli, *J. Appl. Phys.* **86**, 2774 (1999).

[12] C. Adachi. K. Nagai, and N. Tamoto, Appl. Phys. Lett. **66**, 2679 (1995).

[13] J.-H. Lee, J.J. Huang, C.-C. Liao, P.-J. Hu, and Y. Chang, *Chem. Phys. Lett.*, **402**, 335 (2005).

[14] R. Schlaf, P. G. Schroeder, M. W. Nelson, B. A. Parkinson, C. D. Merritt, L.

A. Crisafulli, et al., Surf. Sci. 450 (2000) 142.

[15] H. Aziz, Z. D. Popovic, and N.-X. Hu, *Appl. Phys. Lett.* **81**, 370 (2002).

[16] T. Tsutsui, *Mater. Res. Bull.* **22**, 39 (1997).

[17] Z. Chen, J. Yu, Y. Sakuratani, M. Li, M. Sone, S. Miyata, T. Watanabe, X. Wang, and H. Sato, *J. Appl. Phys.*, **89**, 7895 (2001).

[18] B. J. Chen, X. W. Sun, Y. Divayana, and B. K. Tay, *J. Appl. Phys.*, **98**, 046107 (2005).

[19] T-Y. Chu, and O.-K. Song, *Appl. Phys. Lett.*, **90**, 203512 (2007).

[20] D. V. Morgan, Y. Aliyu, and R. W. Bunce, *Phys. Status Solidi A* 133, 77 (1992).

[21] John C. C. Fan, and John B. Goodenough, *J. Appl. Phys.* 48, 3524 (1977).

[22] I. Hamberg and C. G. Granqvist, J. Appl. Phys. 60, R123 (1986).

[23] K. Sugiyama, H. Ishii, Y. Ouchi, K. Seki, *J. Appl. Phys*. **87** (2000) 295.

[24] M. P. Seah, in *Practical Surface Analysis by Auger and X-Ray Photoelectron Spectroscopy*, edited by D. Briggs and M. P. Seah (Wiley, New York, 1983)

[25] L. Ley and M. Cardona, in *Photoemission in Solids I*, edited by M. Cardona and L. Ley (Springer, New York, 1978).

[26] Th. Kugler, Å. Johansson, I. Dalseg, U. Gelius, and W. R. Salaneck, *Synth. Met*. **91**, 143 (1977).

[27] C. C. Wu, C. I. Wu, J. C. Strum, and A. Kahn, *Appl. Phys. Lett.* **70**, 1348 (1997).

[28] M. G. Mason, L. S. Hung, C. W. Tang, S. T. Lee, K. W. Wong, and M. Wang, *J. Appl. Phys.* **86**, (1999) 1688.

[29] G. Liu, J. B. Kerr, and S. Johnson, *Synth. Met*. **144**, 1 (2004).

[30] S. Z. Sze, *Physics of Semiconductor Devices*, Wiley, New York (1981).

[31] H. Ishii, K. Sugiyama, E. Ito, and K. Seki, *Adv. Mater.* **11**, 605 (1999).

[32] Z. Qiao, R. Latz, and D. Mergel, *Thin Solid Films* **466**, 250 (2004).

[33] F. Nüesch, L. J. Rothberg, E. W. Forsythe, Q. T. Le, and Y. Gao, *Appl. Phys. Lett.* **74**, 880 (1999).

[34] P. He, S. D. Wang, W. K. Wong, C. S. Lee, and S. T. Lee, *Appl. Phys. Lett.* **79**, 1561 (2001).

[35] S. Y. Kim, K. Y. Kim, Y.-H. Tak, and J.-L. Lee, *Appl. Phys. Lett*., **89**, 132108 (2006).

[36] J. T. Yates, N. E. Erickson, S. D. Worley, and T. E. Madey, in *The Physical Basis for Heterogeneous Catalysis*, edited by E. Drauglis and R. I. Jaffee (Planum, New York, 1975), p. 75.

[37] S. M. Tadayyon, H. M. Grandin, K. Griffiths, L. L. Coatsworth, P. R. Norton, H. Aziz, et al., Org. Electron. 5, 199 (2004).

[38] T. A. Delchar, *Vacuum Physics and Technology*, Chapman & Hall, London, 1993, p. 72.

[39] J. C. C. Fan and J. B. Goodenough, *J. Appl. Phys.* **48**, 3524 (1977).

[40] J. Cui, Q. Huang, J. C. G. Veinot, H. Yan, Q. Wang, G. R. Hutchison, A. G. Richter, G. Evmenenko, P. Dutta, and T. J. Marks, *Langmuir* **18**, 9958 (2002).

[41] D. Y. Kondakov, J. R. Sandifer, C. W. Tang, R. H. Young, *J. Appl. Phys.* **93**, 1108 (2003).

[42] H. Aziz, Z. D. Popovic, N.-X. Hu, A.-M. Hor, and G. Xu, *Science* **283**, 1900 (1999).

[43] W. Brütting, S. Berleb, and A. G. Mückl, *Org. Electron.* **2**, 36 (2001).

[44] S. A. Van Slyke, C. H. Chen, and C. W. Tang, *Appl. Phys. Lett.* **69**, 2160 (1996).

[45] P. Y. Yu and M. Cardona, *Fundamentals of Semiconductors*, Springer-Verlag, New York (1996).

[46] T. Watanabe, K. Nakamura, S. Kawami, Y. Fukuda, T. Tsuji, T. Wakimoto, S. Miyaguchi, M. Yahiro, M.-J. Yang, and T. Tsutsui, *Synth. Met.* **122**, 203 (2001).

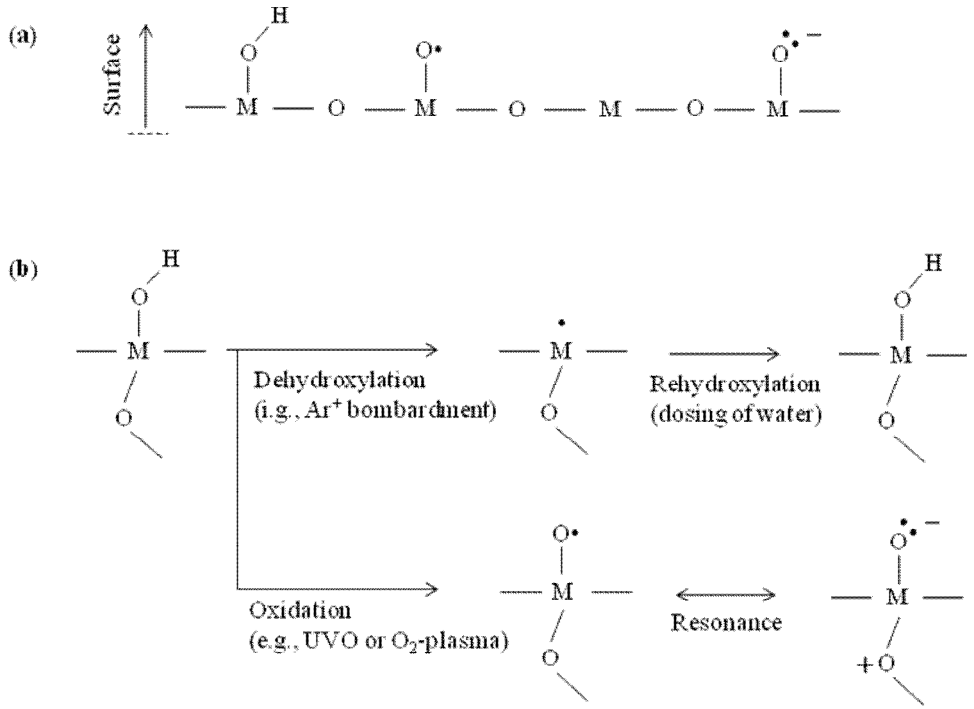

FIG. 2-1. (a) Chemical species of as-cleaned ITO surface, and (b) the chemical modification of the surface hydroxyl group through reduction with Ar^+ bombardment and oxidation with UVO or O_2 plasma treatment [Ref. 1 and 2] where M denotes In or Sn.

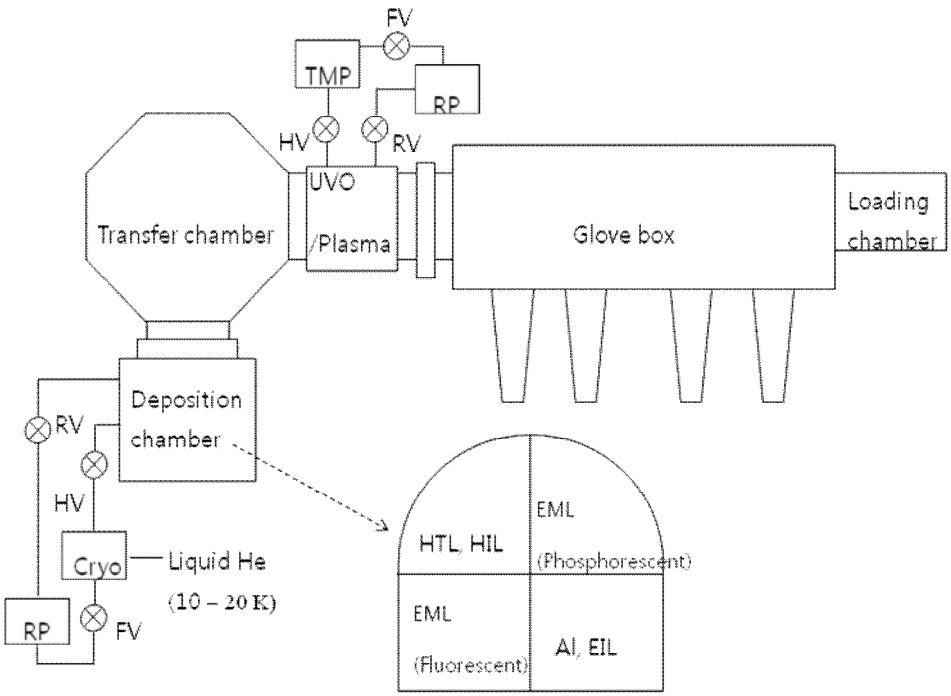

FIG. 2-2. Schematic diagram of OLED fabrication system. Vacuum systems only related to the deposition and UVO/plasma treatment are briefly depicted; Cryo, RP, RV, HV, FV, and TMP denotes the Cryo-pump, rotary pump, roughing valve, high-vacuum valve, fore-line valve, and turbo-molecular pump, respectively. Positions of source materials in the deposition chamber are displayed in the lower part arrowed from the chamber; HTL, HIL, EML, and EIL means the hole transport layer, hole injection layer, emitting layer, and the electron injection layer, respectively.

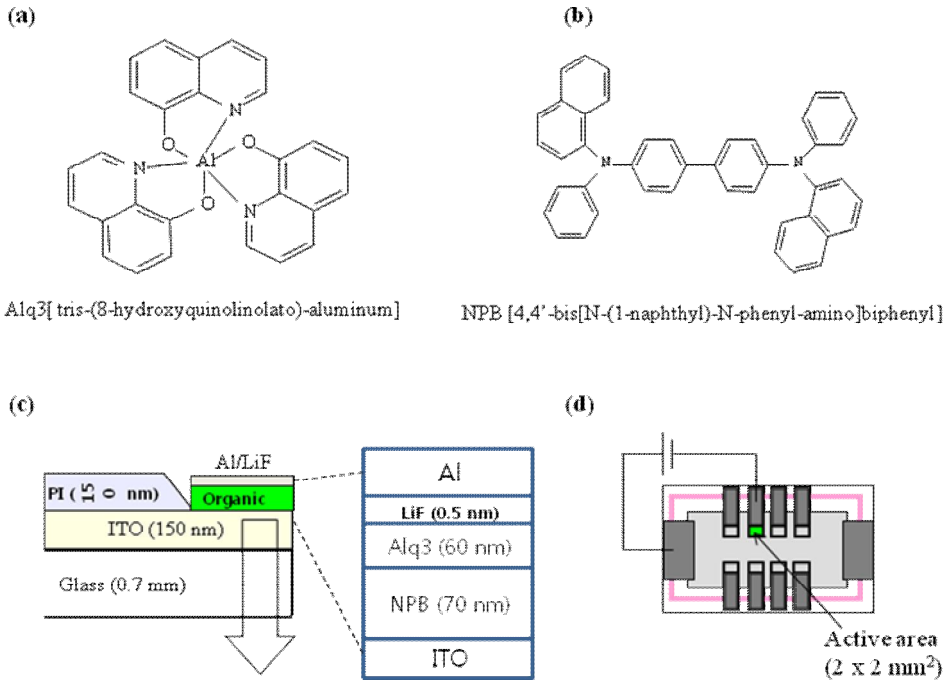

FIG. 2-3. Chemical structure of (a) Alq3 and (b) NPB, (c) schematic of partial cross-sectional view of an OLED device (PI: abbreviation of polyimide), and (d) a sample (30 x 40 mm^2) with eight active patterns of an area of 2 x 2 mm^2.

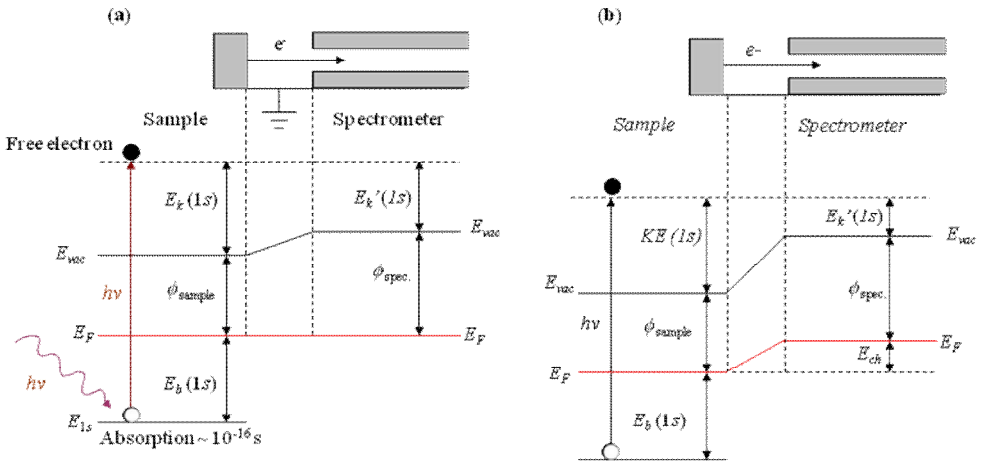

FIG. 2-4. Electron energy diagrams for a (a) conductive or insulating (b) sample surface, and electron energy spectrometer, and variation of the kinetic energy of the photoelectron, which is generated by ultraviolet or X-ray irradiation of its energy $h\nu$, during the drift from the sample surface to the detector of the spectrometer. Here, for example, the photoelectron originating from 1*s* orbital is illustrated. E_{vac}, E_F, E_{1s}, ϕ_{sample}, $\phi_{\text{spec.}}$, E_b (1*s*), E_k (1*s*), E_k' (1*s*), and E_{ch} correspond to the vacuum level, Fermi level, electronic energy level of 1*s* orbital, work function of the sample, work function of the detector of the spectrometer, binding energy of the 1*s* orbital, kinetic energy of the photoelectron positioned at the sample surface, kinetic energy of the photoelectron positioned at the detector surface, and the surface charge energy, respectively. The kinetic energy of the photoelectron can be calculated with the Einstein equation: $E_k' = h\nu - E_b - \phi_{\text{spec.}}$ for conductive samples and $E_k' = h\nu - E_b - \phi_{\text{spec.}} - E_{\text{ch}}$ for insulating surfaces.

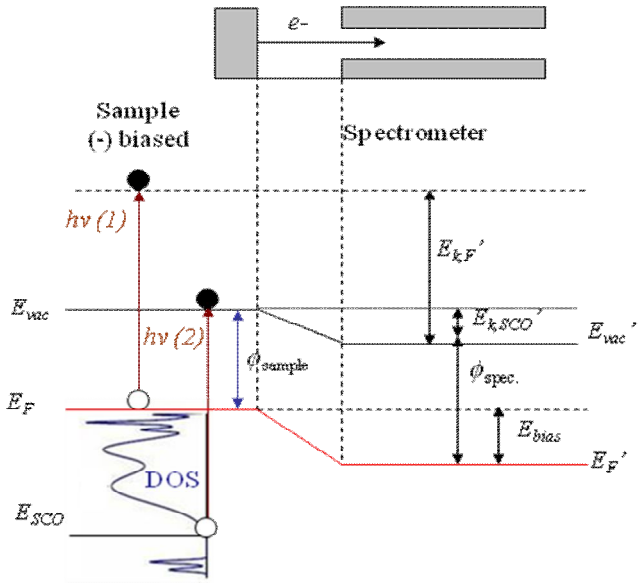

FIG. 2-5. Electron energy diagram for a conductive sample biased negatively and the electron energy spectrometer (left) and the corresponding electron emission spectroscopy obtained through ultraviolet irradiation with energy $h\nu$ (right). E_{vac}, E_F, E_{SCO}, ϕ_{sample}, and $\phi_{spec.}$ correspond to the vacuum level, Fermi level, secondary cut-off level, work function of the sample, and work function of the detector of the spectrometer, respectively. $E_{k,\,F}'$, and $E_{k,\,SCO}'$ are the kinetic energies of the photoelectrons detected at the spectrometer, originating from the Fermi level and secondary cut- off level of the sample, respectively. E_{bias} is the applied bias energy.

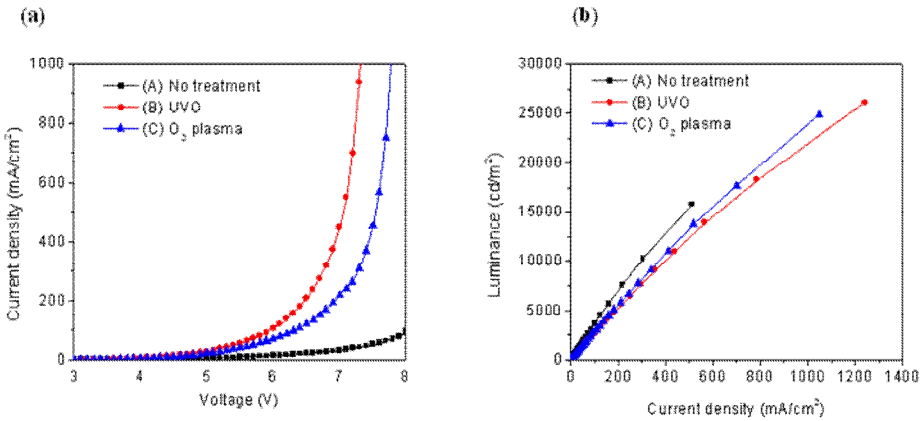

FIG. 2-6. (a) Current density-voltage and (b) luminance-current density characteristics of OLEDs with the ITO anodes treated with UVO and O_2 plasma.

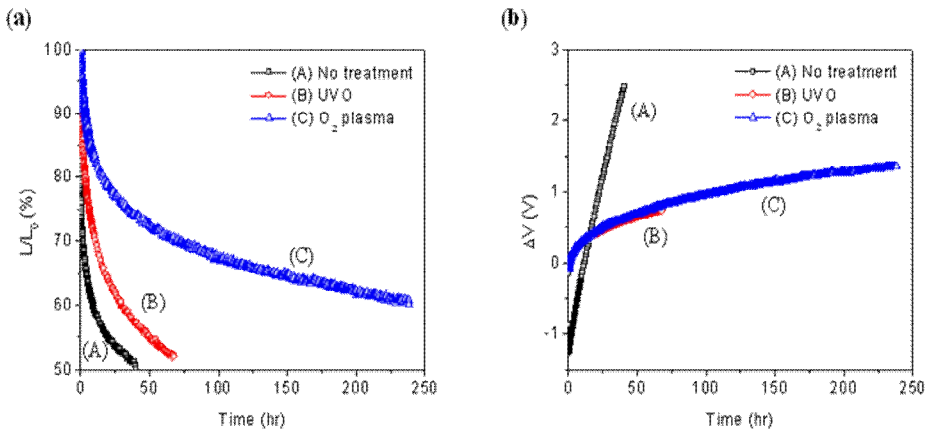

FIG. 2-7. (a) Luminance and (b) voltage changes measured in time at a constant current density of 50 mA/cm^2, as a reflection of operational stabilities for the OLED devices.

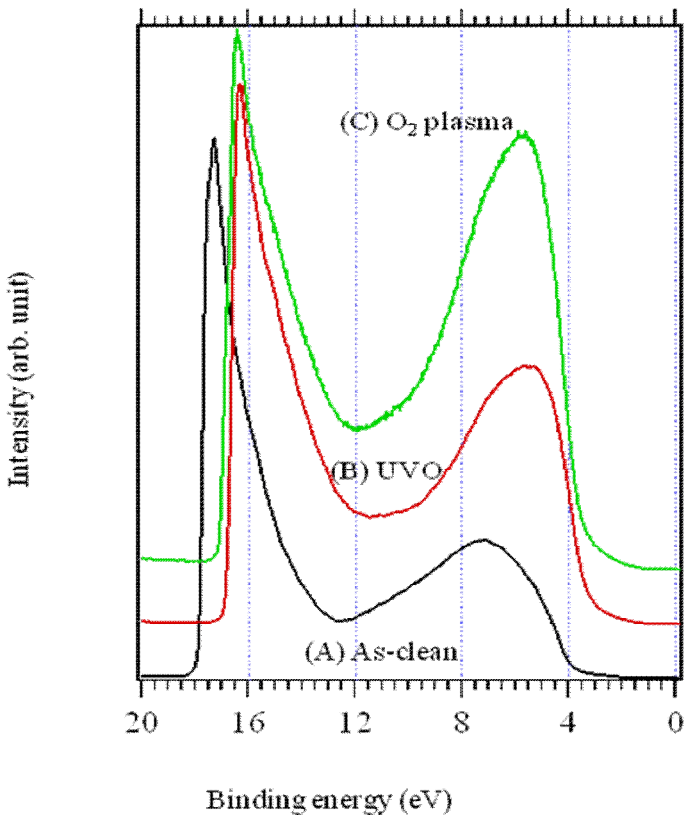

FIG. 2-8. Full range of UPS spectra from the Fermi level to the secondary cutoff regions of the ITOs surface-treated with UVO or O_2 plasma, and the no-treated ITO which is a wet-cleaned control sample before the surface treatments.

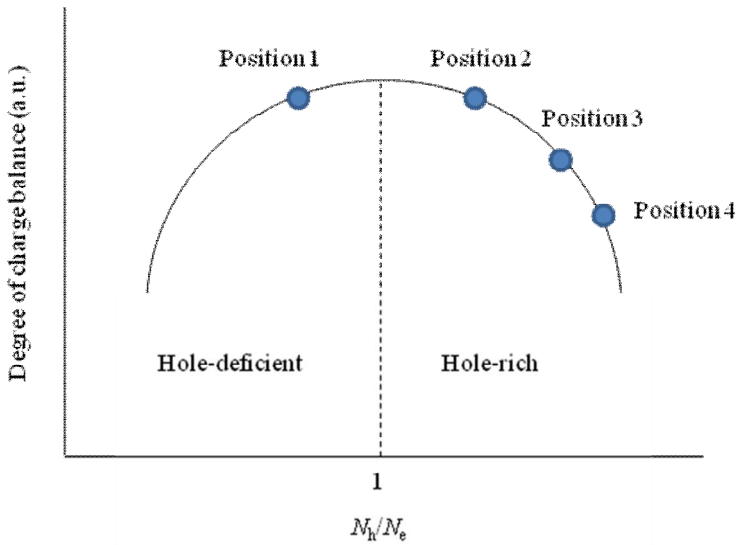

FIG. 2-9. Degree of charge balance vs. N_h/N_e ratio, where N_h and N_e are the number of holes and electrons reaching the electroluminescent center, started from the anode and cathode, respectively.

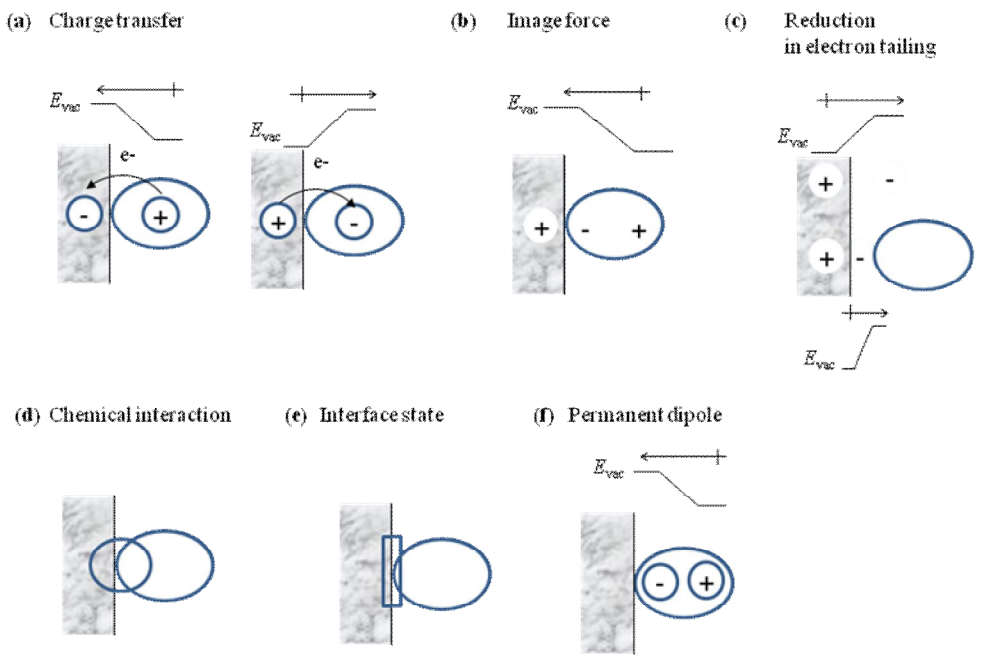

FIG. 2-10. Plausible factors for generation of the interfacial dipoles [Ref. 31]. (a) charge transfer across the interface, (b) image force leading to the positive charging of the vacuum side, (c) Reduction of the electron tailing into vacuum through repulsive interaction between the electron clouds of the adsorbate and metallic surface, (d) rearrangements of the electron cloud and molecular/surface geometries through a strong chemical interaction, (e) formation of the interface states, and (f) adsorption of the polar molecules. E_{vac} corresponds to the vacuum level. Dipole moment is denoted as cross-bar/arrow.

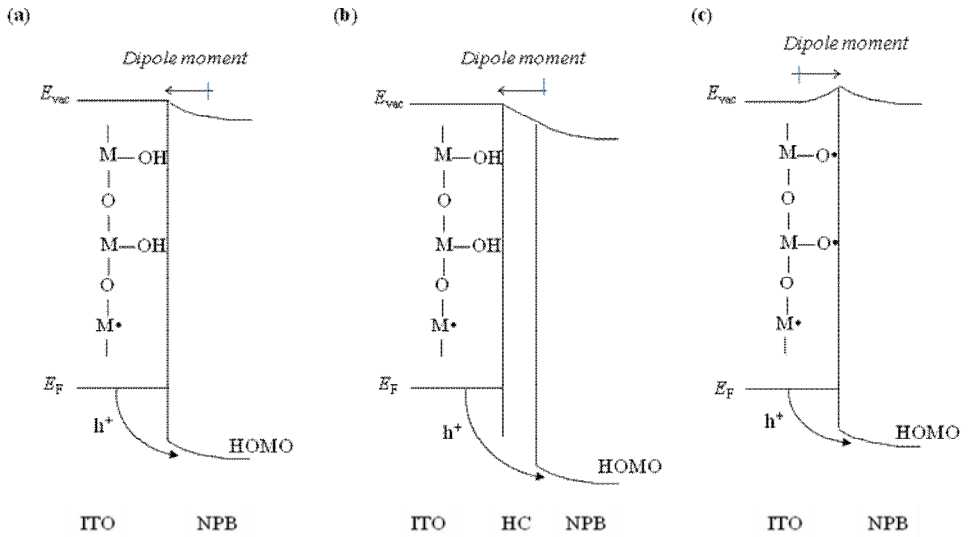

FIG. 2-11. Schematic diagram of electronic structures of the ITO/NPB interfaces with various ITO surfaces: (*a*) as-cleaned ITO, (*b*) hydrocarbon-contaminated ITO, and (*c*) oxidized ITO. E_{vac}, E_F, M, and HC correspond to the vacuum level, Fermi level, metal elements (Sn or In) of ITO, and hydrocarbon contaminants, respectively.

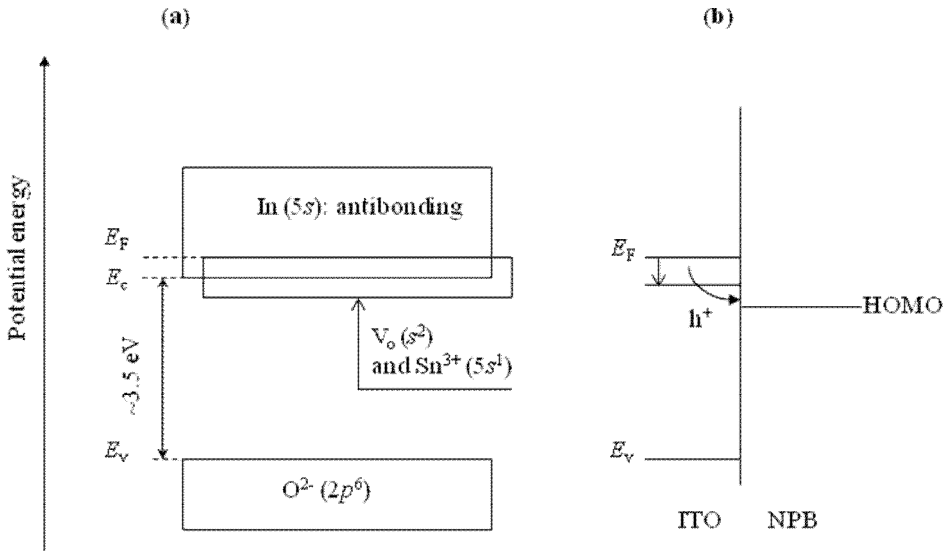

FIG. 2-12. (a) Band structure of ITO based on the Ref. 21 and (b) schematic of hole injection barrier change from ITO to NPB with the downward shift of ITO Fermi level (E_F). E_c and E_v denote the conduction band edge and valence band edge, respectively.

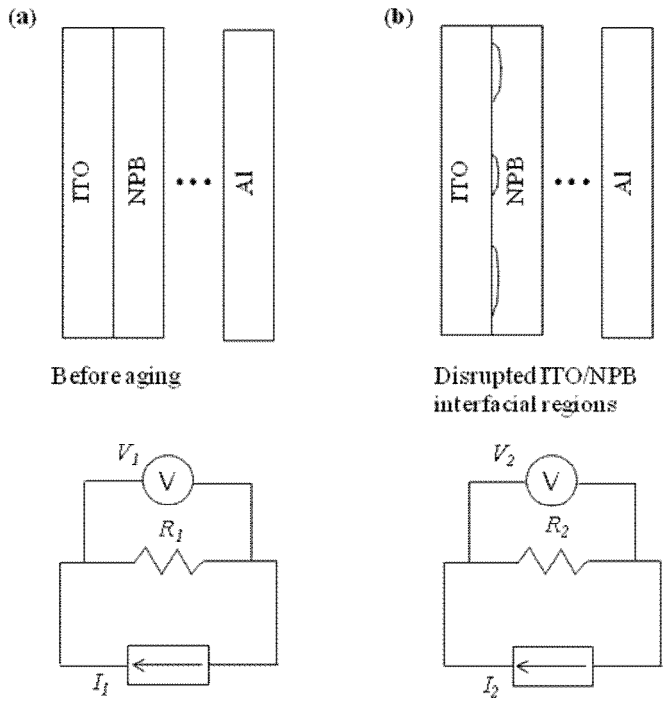

FIG. 2-13. Schematic illustration of the NPB/ITO interface (a) before and (b) after de-lamination and their corresponding simple equivalent electric circuits under an applied constant current source.

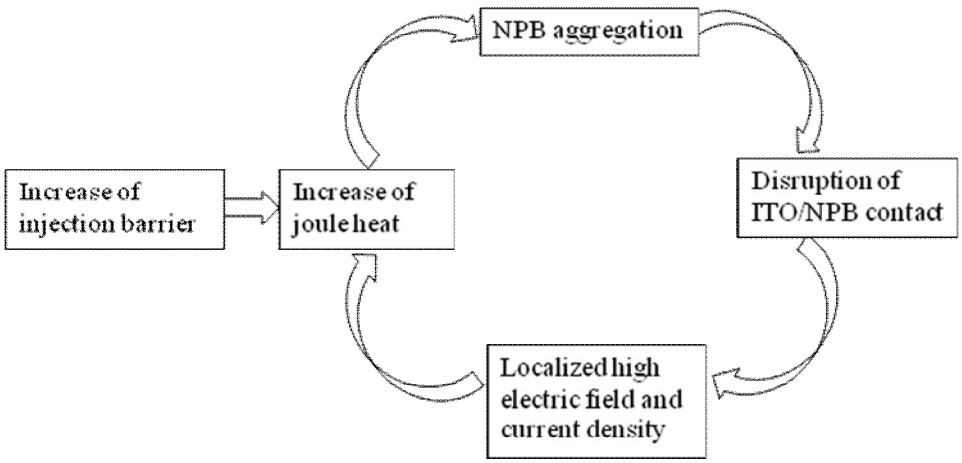

FIG. 2-14. Cycle of device degradation based on the NPB aggregation- or crystallization-induced disruption of the ITO/NPB contact.

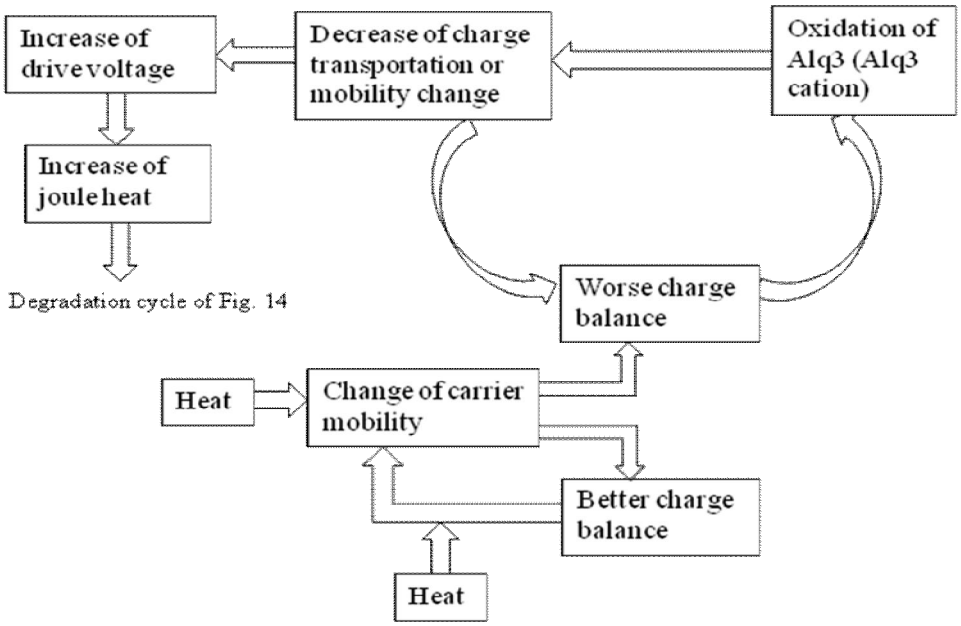

FIG. 2-15. Charge balance breakdown by heat.

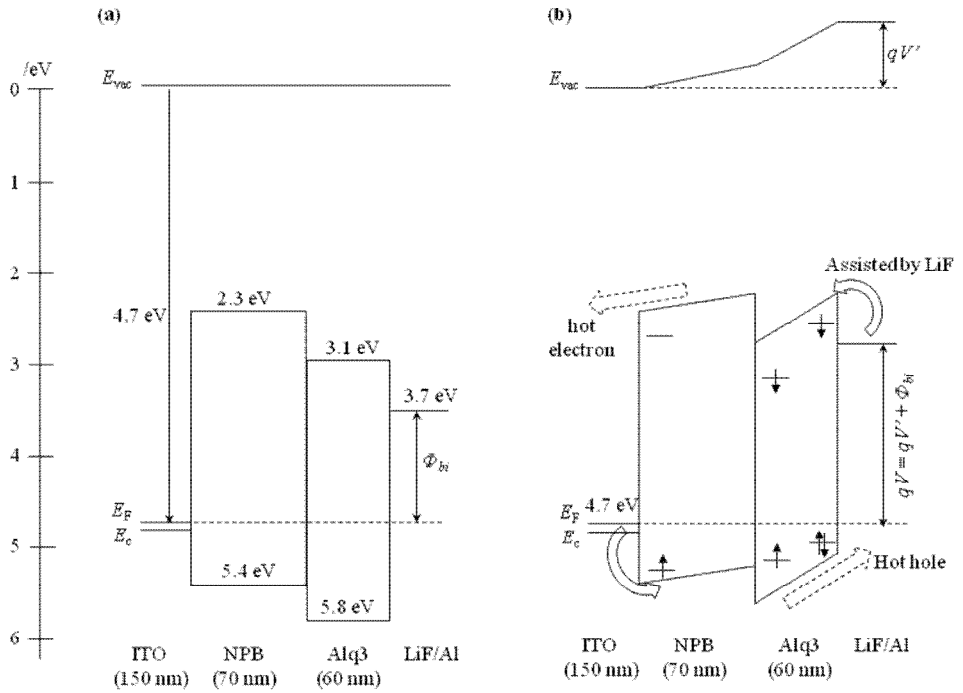

FIG. 2-16. Schematic energy level diagram of the ITO/NPB/Alq3/LiF/Al based on the common vacuum level alignment (a) without applied bias and (*b*) with applied bias voltage exceeding the built-in voltage. E_{vac}, E_F, E_c, Φ_{bi}, qV', and qV correspond to the vacuum level, Fermi level, conduction band edge, built-in potential, effective potential, and applied potential between the electrodes, respectively. Work functions of the ITO and Al, and LUMOs and HOMOs of organics are referenced to reported values [4, and therein]. Details in interface states and the energy levels of LiF are missed for brevity.

TABLE II-1. Summary of the driving voltages, luminance, current efficiencies, power efficiencies, external quantum efficiencies, and 60% lifetimes of devices A, B, and C, operated at a constant current density of 50 mA/cm^2.

Device	Driving voltage (V)	Luminance (cd/m^2)	Current efficiency (cd/A)	Power efficiency (lm/W)	External quantum efficiency (%)	60% lifetime (h)
(A) No-treatment	7.45	1816	3.6	1.5	1.4	9
(B) UVO	5.47	1349	2.7	1.6	1.0	30
(C) O_2 plasma	5.72	1410	2.8	1.6	1.1	226

TABLE II-2. Work function (ϕ) and atomic concentration for the ITOs treated with the UVO and O_2 plasma surface treatments. The values in ( ) are the ratios without carbon.

Treatment	ϕ (eV)	Chemical composition in at. %				Ratio		
		In	Sn	O	C	Sn/In	O/In	O/(1.5In + 2Sn)
(A) No-treatment	4.3	24.0 (31.0)	3.80 (4.90)	49.7 (64.1)	22.5 -	0.158	2.07	1.14
(B) UVO	5.3	25.6 (31.1)	3.90 (4.70)	52.9 (64.2)	17.6 -	0.151	2.06	1.15
(C) O_2 plasma	5.1	27.6 (31.2)	4.30 (4.90)	56.6 (64.0)	11.5	0.157	2.05	1.13

Chapter III

Current-voltage-luminance characteristics of OLEDs using a NaCl-organic composite as a hole injection buffer layer

Abstract

Composite buffer layers of N,N'-bis(naphthalene-1-yl)-N,N'-bis(phenyl)benzidine (NPB) and NaCl at the anode/organic interface were found to be very effective on the hole injection enhancement from an indium tin oxide (ITO) anode to the hole-transport layer (HTL) of NPB. Two maxima of significant current injection with respect to compositional variation were observed, implying multiple injection mechanisms of the tunneling effect and other interfacial effects. From a longer operation lifetime, the enhanced device stability was also confirmed as compared to a standard device with copper phthalocyanine (CuPc) as the hole injection layer.

III-1. Introduction

Although hole transport layer (HTL) materials with low ionization potential are used to match the work function of the indium tin oxide (ITO) anode, an energy barrier to hole injection from the ITO anode to HTL usually exists, resulting in decrease in hole injection efficiency. For example, O_2-plasma-treated ITO shows a work function of ~4.7 eV [1] and adjacent NPB HTL material has HOMO level of ~5.4 eV, resulting in the hole injection barrier of ~0.7 eV. The injection barrier is too high compared to the generally required injection barrier of less than 0.25 eV for non-ICLC (injected-charge-limited current) in most of OLED [2]. With increase in temperature during operation, the injection-limited-current mechanism will be further dominant. Moreover, chemical interactions between the ITO surface and the adjacent organic layer or morphological change of interfacial HTL in contact to ITO may cause degradation of the electronic properties, resulting in shorter lifetime of the OLED device. Thus, many works have been tried to insert a thin buffer layer between the ITO and the HTL for both enhancing the hole injection efficiency and improving the device stability for longer lifetime (the same is true for the interface of cathode/organic ETL interface).

Therefore, a low driving voltage and stable organic/electrode interface, strongly related to the charge injection properties from an electrode to a charge transport layer, are among the essential factors as well as the improvement of intrinsic bulk properties of organic materials. For the enhancement of hole injection, organic semi-conductive buffer layers such as a star-burst amine [3] and phthalocyanines [4,5] with suitable highest-occupied molecular orbital (HOMO)

energy levels, and high work-function metals like Pt and transparent insulating oxides have been used [6,7] have been utilized between the anodes and HTLs. For the injection of electrons, low work function metals, such as Ca, Mg, and Gd have been used as cathodes. As expected from the low work function, these metals are highly reactive, hence unstable in air. They are typically capped or alloyed with more stable metals like Al, Ag, etc. Alternatively, ultrathin insulating layers that contain low work function metal elements (i.e., LiF [8]) are introduced to allow dipole or bias-induced realignment of the Fermi levels of the metal electrodes and the lowest-occupied molecular orbital (LUMO) energy levels of the ETLs. Thus the interlayer materials for charge injection have been chosen in accordance with whether the interlayer is for hole or electron injection.

However, metal halides, mostly applied on the cathode/organic interfaces, have also been tried for better anode/organic interfacial property [9,10]. LiF, the most common electron injection layer (EIL) material, was reported to be effective in hole injection enhancement on hydrogen plasma treated ITO anodes, but not on the ones with more practically used oxidative treatments like oxygen plasma or ultra-violet ozone [11]. In addition, metal halides such as LiF and MgF_2 in a composite form with HTL materials have been reported to improve thermal stability of OLEDs [10,12].

Here, the improvements of both hole injection and device stability are demonstrated by using an alkali metal halide on ITO anode side as an HIL. The use of metal halides in the anode region can make simple the fabrication process of highly efficient OLEDs by introducing the same metal halide for both electron and

hole injection enhancement. And those alkali metal halides are usually cheap and easy to handle, compared to other organic or metal oxide interlayer materials such as CuPc [4], buckminsterfullerene [13,14], MoO_3 [15].

III-2. Experiments

To fabricate the devices for current investigation, an ITO-coated glass substrate with a sheet resistance of 15 Ω/cm^2 was used and an oxygen plasma treatment was employed to clean the substrate. The organic layers and the cathode layers were deposited onto the ITO substrate by resistive heating. NPB, tris(8-hydroxyquinoline) aluminum (Alq_3), and LiF were used as HTL, electron transport and emitting layer, and EIL material, respectively. The device structure was ITO/NPB:NaCl (1:*x* wt %) (*y* nm)/NPB (60-*y* nm)/Alq_3 (40 nm)/LiF (0.5 nm)/Al. To evaluate the effect of the NPB:NaCl buffer layer on the operational stability, reference devices with the structure of ITO/NPB (60 nm)/Alq_3 (40 nm)/LiF (0.5 nm)/Al and ITO/CuPc (16 nm)/NPB (44 nm)/Alq_3 (40 nm)/LiF (0.5 nm)/Al were used. The current density-voltage (*J-V*) characteristics of the devices were measured by a dc source (Keithley 238), and the brightness (*L*) was measured using a luminance meter (PR650). The lifetime measurements were carried out using a semiconductor parameter analyzer (HP 4155B) and a Si photodiode (SI1226) under the ambient condition at a constant current density of 50 mA/cm^2.

III-3. Results and discussion

Figure 1 exhibits the *J-V* characteristics of the devices with the structures of ITO/NPB:NaCl (*y* nm)/NPB (60-*y* nm)/Alq_3 (40 nm)/LiF (0.5 nm)/Al with different buffer layer thicknesses (y). The composition of NPB:NaCl was varied in 1:y wt %, where y is 0.5, 2, 8, 15, 30, or 45. At low composition of NaCl (1:0.5 wt %) and thin (1 nm) buffer layer condition in Fig. 1(a), the current density is lower than that without the buffer layer. At this relatively low concentration of NaCl, the NaCl seems to give just a negative effect on the hole injection. With the increase in the buffer layer thickness, the current density starts to increase until an optimum thickness of 8 nm. After then, the current density decreased gradually, reflecting the increase in insulating nature of the buffer film. Thus, the most effective reduction in driving voltage from 5.2 V (without the buffer layer) to 3.8 V at a current density of 50 mA/cm^2 is obtained for the device with thickness of 1 nm and composition of 1:2 wt % [Fig. 1(b)]. The devices with other compositions of NPB:NaCl (1:*y* wt%, *y* of 8, 15, 30 and 45) showed the same trend with different optimal thicknesses, shown in Fig 1(b), (c), (d), (e) and (f). The thickness dependence with an optimal thickness value is typically observed for OLED devices with insulating materials as a charge injection buffer layer, where the charge injection is based on the tunneling mechanism [6,11,16,17]. Thus the current injection enhancement is attributable to the highly dielectric property of the NaCl composite buffer layer which takes more electric field under the bias voltage and hence induces tunneling injection with lower barrier height [18].

However, when the *J-V* curves are plotted according to the variation of NPB:NaCl composition under the same buffer layer thickness, the current density

is found to have fluctuations with change of the composition at the same voltage, leading to two or three optimum compositions for high current injection. In the case of 1 nm thickness of the composite buffer (Fig. 2(a)), The addition of NaCl in NPB increases the current density until the first optimal composition of 1:2 wt % after slight decrease in the current density at 1:0.5 wt %, and then reduces (again) the current density with higher NaCl composition up to 1:8 wt %. The current density rises back until the second optimal composition of 1:30 wt %, after then with further higher composition of NaCl, the current density decreases back again and finally the current increases at pure NaCl with nominal thickness of 1 nm. Other devices with different thicknesses of the composite buffer also showed a similar compositional trend with multiple optimum points at 1:2, 1:30, or 1:8shown in Fig. 2(b), (c), and (d). The dependence of thickness and composition on the device performance is summarized in Fig. 3(a), which displays current density versus compositions with various thicknesses at the driving voltage of 5.6 V. Two maximum composition points of current density are clearly observed at 1:2 and 1:30 wt %, regardless of buffer layer thickness except 16 nm. Thus, it turns out that there exist at least two optimal compositional points, implying that multiple mechanisms including the tunneling injection are working for the enhanced current injection. In addition to the tunneling injection model by insulating buffer layer, other interfacial effects such as energy level realignment with the interfacial dipole [19] or gap state formation [20], enhanced mechanical adhesion [21], etc., are conceivable. Though the origin of the hole injection through the composite buffer layer will be further investigated in chapter 4, the interfacial effects may be

dominant for the first peak at 1:2 wt % in Fig. 3 (a), and the low composition of NaCl for the interfacial effects may appear with relatively low coverage of the surface. For clearer view of the current density variation in a corresponding composition range, a region including the first peak is magnified as shown in Fig. 3 (b). At 1:0.5 wt % and 1 nm thickness of the composite buffer, NaCl seems to be too small amount to enhance the hole injection, which might be due to ineffective electric contact between NPB and ITO because of the intervening NaCl insulating particles. With increase in NaCl amount, positive interfacial effect(s), which is described in chapter 4, starts to work, leading to current density maxima at 1:0.5 wt% (8 nm) and 1:2 wt% (1 nm). With further increase in NaCl through thickness increase at each compositional ratio, the current density decreases back maybe due to the insulating property of NaCl. On the other hand, the tunneling injection model for the second peak at 1:30 wt % may be preferred, which requires almost full coverage of that. Therefore, the variation of current density along with the buffer layer thickness and composition can be explained by the combination of tunneling model and interfacial effects under the trade-off with the electrical resistance increase in the buffer layer due to the NaCl insulating property. Consecutively, in the middle composition range (i.e., 1:8 and 1:15 wt %), both tunneling and interfacial effects are considered to simultaneously affect the hole injection efficiency. It is noticeable that overall current density and the relative intensity of the first peak to the second one decrease with increase in the buffer layer thickness, ending to be indistinguishable between the first and second peaks at 16 nm in Fig. 3(a). This is ascribed to the increased electrical resistance due to the insulating

nature of the buffer layer. That is, in the lower composition region of NaCl, the current injection vanishes rapidly via the suppression of the interfacial effects.

To evaluate the effect of the composite buffer on the charge balance, *J-V-L* and *L-J* characteristics of OLED devices with the composite buffer layers corresponding to the two peaks in Fig. 3, 1:2 wt % and 1:30 wt % are compared to those of two references, one without the buffer layer and the other with CuPc (16 nm) buffer layer, shown in Fig. 4 and 5. *L-V* curves have very similar shape and trend in the variation of the buffer layer thickness to *J-V* ones. As expected in principle, with the increase in the current injection efficiency by adopting the composite buffer layers, the luminance also increases (Fig. 4) at the same voltage. The current injection efficiency and luminance intensity at the same voltage are in the order of (1 nm) > (4 nm) > (8 nm) > (16 nm) > (no buffer layer) > (CuPc (16 nm)) for 1:2 wt % buffer layers, and (4 nm) > (8 nm) > (1 nm) > (16 nm) > (no buffer layer) > (CuPc (16 nm)) for 1:30 wt % buffer layers. However, from *L-J* curves in Fig.5, luminance intensities at the same current density are found to be in the order of (CuPc (16 nm)) > (no buffer layer) > (16 nm) > (8 nm) or (4 nm) > (1 nm) for 1:2 wt % buffer layers, and (CuPc (16 nm)) > (no buffer layer) > (16 nm) > (8 nm) or (1 nm) > (4 nm) for 1:30 wt % buffer layers, almost inverse order of the current injection efficiency above. It seems that the charge balance at the electroluminescent center is broken more severely with increase in hole injection efficiency, implicating the current OLED devices are hole-rich or hole-excess.

Differentiation of the *L-J* curve corresponds to current efficiency: the steeper the *L-J* curve, the higher the current efficiency. Fig. 6 displays current and

power efficiency along with current density. After initial stage of relatively large charge imbalance (namely, lower current efficiency under the current density of ca. 50 mA/cm^2) maybe due to larger contribution of non-emissive current paths like ohmic leakage current at low current or low voltage region, the current efficiencies are almost constant (Fig. 6), reflecting the generation of emission centers based on exciton formation from injected charge carriers in OLEDs. The current efficiency slightly increases with the increase in drive voltage (data not shown here), because the current would follows space-charge limited current (SCLC, $J \sim V^2$) behavior. Power efficiency decreases with the increase in current density due to simultaneous increase in current density and driving voltage. Due to voltage dependence of power efficiency, OLED devices with high current efficiency not always have high power efficiency. For example, CuPc (16 nm) reference shows the highest current efficiency but the lowest power efficiency in a large current density range. In Fig. 7, driving voltage, current and efficiency are simultaneously compared at current density of 50 mA/cm^2 (upper panel) and at luminance of 1000 cd/m^2 (lower panel) for OLEDs with 1:2 and 1:30 wt % composite buffer layers. When driving voltage decreases through hole injection enhancement with the composite anodic buffer layer, the current efficiency also decreases, as expected in hole-rich devices, but power efficiency is more or less recovered because of the lower driving voltage.

To investigate operational stabilities, luminance and driving voltage change in time (*L*-*t* or *V*-*t*) were measured at a constant current density of 50 mA/cm^2 for the devices with the composite buffer layer of 1:15 (device B), 1:30 (device C), and 1:45 (device D) wt % all in 4-nm thickness, and reference devices

(device A without anodic buffer layer and device E with CuPc buffer layer)shown in Fig. 8. Relatively steep increase in the driving voltage is observed during short-term operation time less than 200 h. OLED devices with lower initial driving voltage seem to give lower driving voltage after long-term operational aging, implying that the initial driving voltage plays significant role in degradation of OLED devices. From the *L*-*T* curve, device A (no buffer layer) shows the shortest life time, and devices with the composite buffer layer (device B, C, and D) have longer life time than the reference devices. Table I exhibits summarized values of initial driving voltage, initial luminance , initial current and power efficiency, and 70% life-time (namely, decay time by the 70% of initial brightness (L_0)) for each device operated at a constant current density of 50 mA/cm^2.

For the life-time comparison between the devices at the same brightness condition, the stretched exponential decay behavior has been adopted to fit the experimental luminance-time (*L*-*t*) curves [22].

$$\frac{L}{L_0} = \exp\left(-\left(\frac{t}{\tau}\right)^{\beta}\right), \qquad (1)$$

where τ and β are fitting parameters and τ, especially, corresponds to the life-time at which the luminance reaches 1/*e* of the initial luminance. Further, from the estimated life times at different initial luminance or initial current density values, L_0-$t_{1/2}$ characteristics can be expressed by using the equation

$$L_0^{\,n} t_{1/2} = \text{constant}, \qquad (2)$$

where *n* is the acceleration coefficient and $t_{1/2}$ is the half-life. Both β and *n* depend on the materials and the device architecture. Moreover, accelerations, of which test

conditions are higher luminance or higher temperature, might induce other or multiple aging mechanisms. The stretched exponential decay behavior seems to be physically based on the aging mechanism of light-emission centers. Another widespread fitting method for the prediction of operational stability from *L-t* curves is to use a combination of exponential decays, commonly two terms, the first-one accounting for the rapid initial decay, the second-one for the long-term degradation ($L/L_0 = ae^{-\alpha t} + be^{-\beta t}$, where a, b, α, and β are fitting parameters). However this approach is strongly dependent on when the fit is done (namely, the duration of aging acceleration).

Here, the projected 70% life under the initial luminance of 1000 cd/m^2 was estimated by simply assuming $n = 1$ in Eq. (2), based on the scalable law of Coulombic degradation [23], resulting in 636, 447, and 564 h for the device B, C, and D, respectively, which overwhelm 93 h of the device A without buffer layer and 324 h of the CuPc-based device E.

Degradation of OLEDs is known to proceed rapidly under high temperature conditions. The lipophilic NPB (aqueous contact angles of ~90°) was reported to undergo decohesion on the hydrophilic ITO surface (advancing aqueous contact angle ~0–30°) under mild heating [24]: the large surface energy mismatch at the ITO/NPB interface introduces an intrinsic micro-structural instability and will cause interfacial decohesive forces under the influence of localized resistive heating at/near the glass temperature of NPB. The joule heat generated during operation can cause crystallization of NPB [25], leading to the generation of disrupted contact areas between NPB and ITO. Thus, the current would bypass the

disrupted contact regions, making higher electric field and current density focused on the still contacted areas of NPB and ITO at a constant current density (here, 50 mA/cm^2). The increased local electric field would increase the joule heat further, accelerating the crystallization of NPB and disruption of the interface, hence degradation of the OLEDs (i. e., steeper *L-t* curves). Therefore, decreasing the driving voltages can be considered to suppress the generation of joule heat and reduce the thermally induced degradation of OLEDs. Another well known degradation mechanism is based on the charge imbalance or excess charge accumulation at the emission zone [26-29], especially induced by electrochemically unstable cations of Alq3 molecules due to the high hole mobility of NPB over the electron mobility of Alq_3 by up to two orders of magnitude [30]. The generated Alq3 cations might serve as deterrents of electron mobility in the ETL material [31], causing further charge-imbalance in hole-rich devices as here. The fixed and accumulated cations might hinder further charge (hole) injection and (electron) transportation, leading to the increase in driving voltage [29]. The charge balance can be improved by introducing a proper ETL having higher electron mobility or shorter electron drift time from cathode to the recombination zone. The degree of charge balance could be reflected on the current efficiency. Thus both driving voltage and current efficiency must be considered as critical factors to the enhancement of OLED lifespan.

Among the devices with an anodic buffer layer (device B, C, D, and E), device D shows the lowest driving voltage while device E has the largest current efficiency, and the longest life span appears in device B. At this point, power

efficiency (η_p) would be a rule of thumb for evaluation of the collective effects of both current efficiency (η_c) and driving voltage (V_D) on the device lifetime because it is related with the current efficiency and the driving voltage by the equation, $\eta_p = \pi\eta_c/V_D$: the larger the power efficiency is, the longer the lifetime would be. For example, the current efficiency of the device B is lower than those of devices E, the power efficiency is higher due to the reduction of driving voltage, from 1.43 (device E) to 1.80 lm/W, hence the life time is also longer, from the projected 70% lifetime of 324 h to 636 h. Thus, it is found that the power efficiency and the projected 70% lifetime are in the same order of (device B) > (device D) > (device C) > (device E), as data shown in Table I. Meanwhile, the device A shows the shortest life time even though it has higher power efficiency than device C and E, displayed as a sudden decrease curve at the initial stage of the device operation in Fig. 8, indicating that another origin serves as a significant degradation process in device A. Due to the absence of anodic buffer layer, the migration of indium (In) components into the NPB HTL is thought to be severely attributed to the initial degradation [32].

The improvement of lifetime can stem from better interfacial stability of ITO/NPB:NaCl/NPB. The enhanced wettability of NaCl to the ITO surface can be anticipated by the stronger interaction between ionic polar NaCl molecules/clusters and highly hydrophilic ITO surface induced by the oxidative O_2-plasma surface treatment [33,34]. Moreover, the enhanced mechanical contact between the ITO anode and NPB in the presence of NaCl particles or clusters might be deduced from interfacial energetics, of which investigations are given in chapter IV. Such a

morphological effect also contributes to the previous result of hole injection enhancement by the reduction in electrical resistance, in addition to the enhanced lifetime through the suppression of NPB aggregation/crystallization with the intervening NaCl molecules.

III-4. Conclusions

We have studied the OLED device performance using a NaCl composite as HIL and optimized its thickness and composition with NPB. The metal halide composite film, which has conventionally been used as EIL, can function as an excellent HIL for both lowering operation voltage and improving device stability. The NaCl:NPB composite buffer layer reduced the operation voltage from 5.2 to 3.8 V at the current density of 50 mA/cm^2, leading to an enhanced power efficiency. The optimized composite buffer layer also enhanced device stability compared to normal OLED structures, showing higher operational lifetime even under significant charge imbalance of lower current efficiency. A combination of optimal thickness and composition of NaCl:NPB buffer layer can be a practical choice of HIL with both reduced operation voltage and enhanced device stability which are two crucial factors for industrial applications.

References

[1] D. J. Milliron, I. G. Hill, C. Shen, A. Kahn, and J. Schwartz, *J. Appl. Phys.* **87**, 572 (2000).

[2] M. Pope and C. E. Swenberg, *Electronic Processes in Organic Crystals and Polymers*, 2nd ed. (Oxford University Press, Oxford, 1999).

[3] S.-F. Chen, and C.-W. Wang, *Appl. Phys. Lett.* **85**, 765 (2004).

[4] S. M. Tadayyon, H. M. Grandin, K. Griffiths, P. R. Norton, H. Aziz, and Z. D. Popovic, *Org. Electron.* **5**, 157 (2004).

[5] C.-a. Di, G. Yu, Y. Liu, X. Xu, Y. Song, and D. Zhu, *Appl. Phys. Lett.*, **90**, 133508 (2007).

[6] Z. B. Deng, X. M. Ding, S. T. Lee, and W. A. Gambling, *Appl. Phys. Lett.* **74**, 2227 (1999).

[7] C. Qiu, Z. Xie, H. Chen, M. Wong, and H. S. Kwok, *J. Appl. Phys.* **93**, 3253 (2003).

[8] M. Matsumura, K. Furukawa, and Y. Jinde, *Thin Solid Films* **331**, 96 (1998).

[9] S. W. Shi, D. G. Ma, and J. B. Peng, Eur. Phys. *J. Appl. Phys.* **40**, 141 (2007).

[10] S. Tokito, and Y. Taga, *Appl. Phys. Lett.* **66**, 673 (1995).

[11] J. M. Zhao, S. T. Zhang, X. J. Wang, Y. Q. Zhan, X. Z. Wang, G. Y. Zhong, Z. J. Wang, X. M. Ding, W. Huang, and X. Y. Hou, *Appl. Phys. Lett.* **84**, 2913 (2004).

[12] D. Grozea, A. Turak, Y. Yuan, S. Han, Z. H. Lu, and W. Y. Kim, *J. Appl. Phys.* **101**, 033522 (2007).

[13] Y. Y. Yuan, S. Han, D. Grozea, and Z. H. Lu, *Appl. Phys. Lett.* **88**, 093503 (2006).

[14] Y. Yuan, D. Grozea, and Z. H. Lu, *Appl. Phys. Lett.* **86**, 143509 (2005).

[15] H. You, Y. Dai, Z. Zhang, and D. Ma, *J. Appl. Phys.* **101**, 026105 (2007).

[16] S. W. Tong, K. M. Lau, H. Y. Sun, M. K. Fung, C. S. Lee, Y. Lifshitz, and S. T. Lee, *Appl. Surf. Sci.* **252**, 3806 (2006).

[17] X. Jing et al, *Chinese Phys. Lett.* **23**, 928 (2006).

[18] S. T. Zhang, X. M. Ding, J. M. Zhao, H. Z. Shi, J. He, Z. H. Xiong, H. J. Ding, E. G. Obbard, Y. Q, Zhan, W. Huang, and X. Y. Hou, *Appl. Phys. Lett.* **84**, 425 (2004).

[19] S. Y. Kim, K. Hong, and J.-L. Lee, *Appl. Phys. Lett.* **90**, 183508 (2007).

[20] Y. Yi, S. J. Kang, K. Cho, J. M. Koo, K. Han, K. Park, M. Noh, C.-N. Whang, K. Jeong, and E. J. Hahn, *Appl. Phys. Lett.* **86**, 113503 (2005).

[21] Y. Shen, D. B. Jacobs, G. G. Malliaras, G. Koley, M. G. Spencer, and A. Ioannidis, *Adv. Mater.* **13**, 1234 (2001).

[22] C. Féry, B. Racine, D. Vaufrey, H. Doyeux, and S.Cinà, *Appl. Phys. Lett*. **87**, 213502 (2005).

[23] H. Aziz, Z. D. Popovic, and N.-X. Hu, *Appl. Phys. Lett.* **81**, 370 (2002).

[24] J. Cui, Q. Huang, J. C. G. Veinot, H. Yan, Q. Wang, G. R. Hutchison, A. G. Richter, G. Evmenenko, P. Dutta, and T. J. Marks, *Langmuir* **18**, 9958 (2002).

[25] S. Y. Kim, K. Y. Kim, Y.-H. Tak, and J.-L. Lee, *Appl. Phys. Lett*., **89**, 132108 (2006).

[26] Z. Chen, J. Yu, Y. Sakuratani, M. Li, M. Sone, S. Miyata, T. Watanabe, X. Wang, and H. Sato, *J. Appl. Phys.* **89**, 7895 (2001).

[27] B. J. Chen, X. W. Sun, Y. Divayana, and B. K. Tay, *J. Appl. Phys.* **98**, 046107 (2005).

[28] J.-H. Lee, J.J. Huang, C.-C. Liao, P.-J. Hu, and Y. Chang, *Chem. Phys. Lett.* **402**, 335 (2005).

[29] D. Y. Kondakov, J. R. Sandifer, C. W. Tang, R. H. Young, *J. Appl. Phys.* **93**, 1108 (2003).

[30] T-Y. Chu, and O.-K. Song, *Appl. Phys. Lett.* **90**, 203512 (2007).

[31] H. Aziz, Z. D. Popovic, N.-X. Hu, A.-M. Hor, and G. Xu, *Science* **283**, 1900 (1999).

[32] S. T. Lee, Z. Q. Gao, and L. S. Hung, *Appl. Phys. Lett.* **75**, 1404 (1999).

[33] Z. H. Huang, X. T. Zeng, X. Y. Sun, E. T. Kang, J. Y. H. Fuh, and L. Lu, *Org. Electron.* **9**, 51 (2008).

[34] J. S. Kim, R. H. Friend, and F. Cacialli, *J. Appl. Phys.* **86**, 2774 (1999).

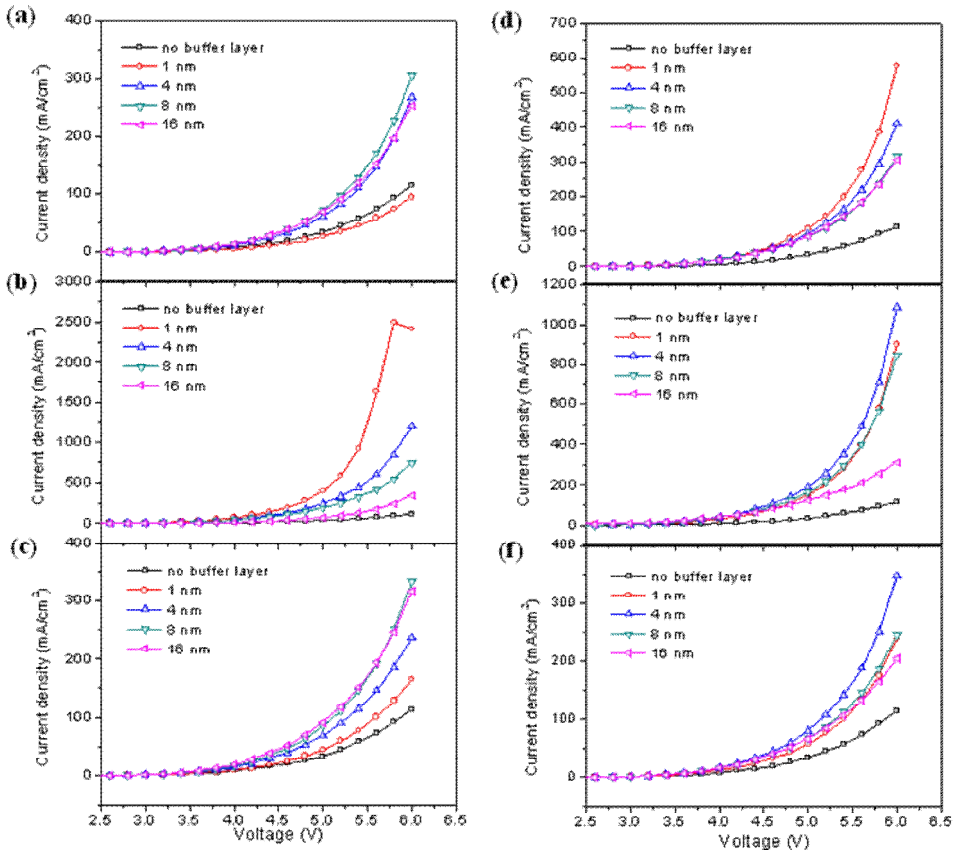

FIG. 3-1. Current density (J)-voltage (V) characteristics of OLEDs with different NPB:NaCl compositions [1:y wt %, y's of 0.5 (a), 2 (b), 8 (c), 15 (d), 30 (e), and 45 (f)] and various thicknesses of the composite buffer layer.

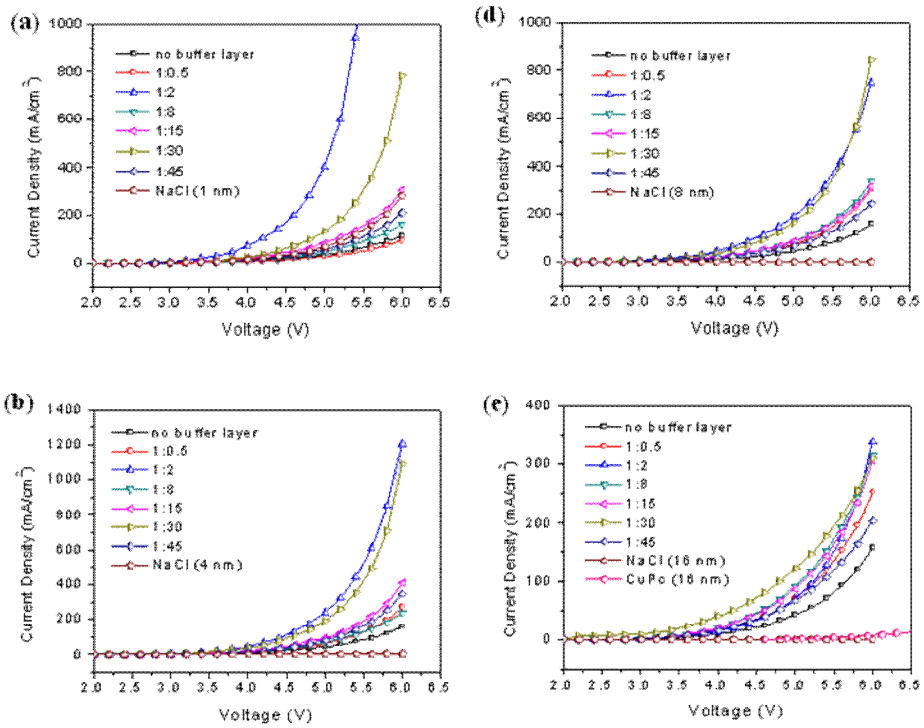

FIG. 3-2. Each *J-V* curve displayed along with different NPB:NaCl compositions from *J-V* characteristics of Fig. 3-1 for the different buffer layer thicknesses, 1 nm (a), 4 nm (b), 8 nm (c) and 16 (d).

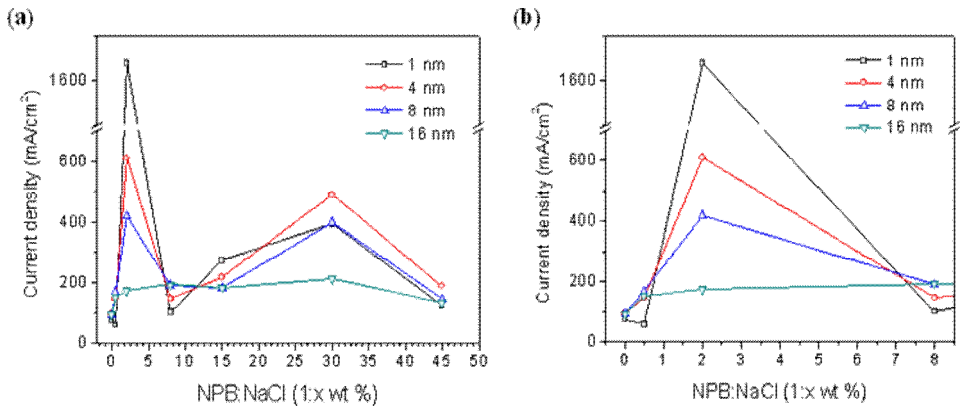

FIG. 3-3. Current density versus NPB:NaCl concentration ratio at 5.6 V in the *J-V* curves of OLEDs for four different buffer layer thicknesses (a), of which the first peak is magnified in a corresponding *x*-axis for clear view (b).

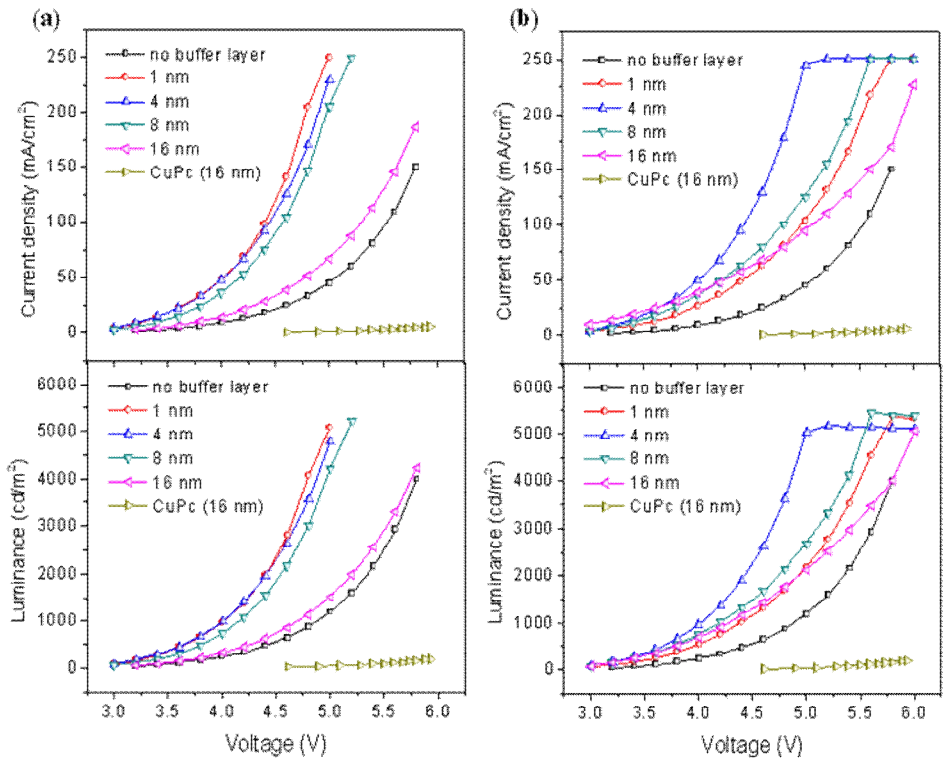

FIG. 3-4. Current density (J)-voltage (V)-Luminance (L) characteristics for ITO/NPB:NaCl [1:y wt %, y = 2 (a) and y = 30 (b)] with various thickness values. Reference device architectures are ITO/NPB/Alq_3/LiF/Al (no-buffer layer) and ITO/CuPc (16 nm)/NPB/Alq_3/LiF/Al.

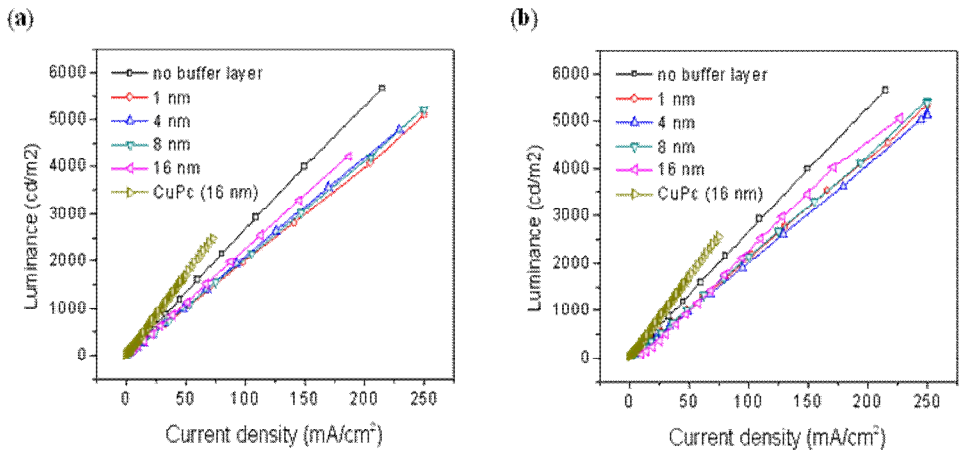

FIG. 3-5. Luminance-current density characteristics of OLEDs with NPB:NaCl [1:*y* wt %, *y* = 2 (a) and *y* = 30 (b)] anodic buffer layers in various thickness values. Reference device architectures are ITO/NPB/Alq_3/LiF/Al (no-buffer layer) and ITO/CuPc (16 nm)/NPB/Alq_3/LiF/Al.

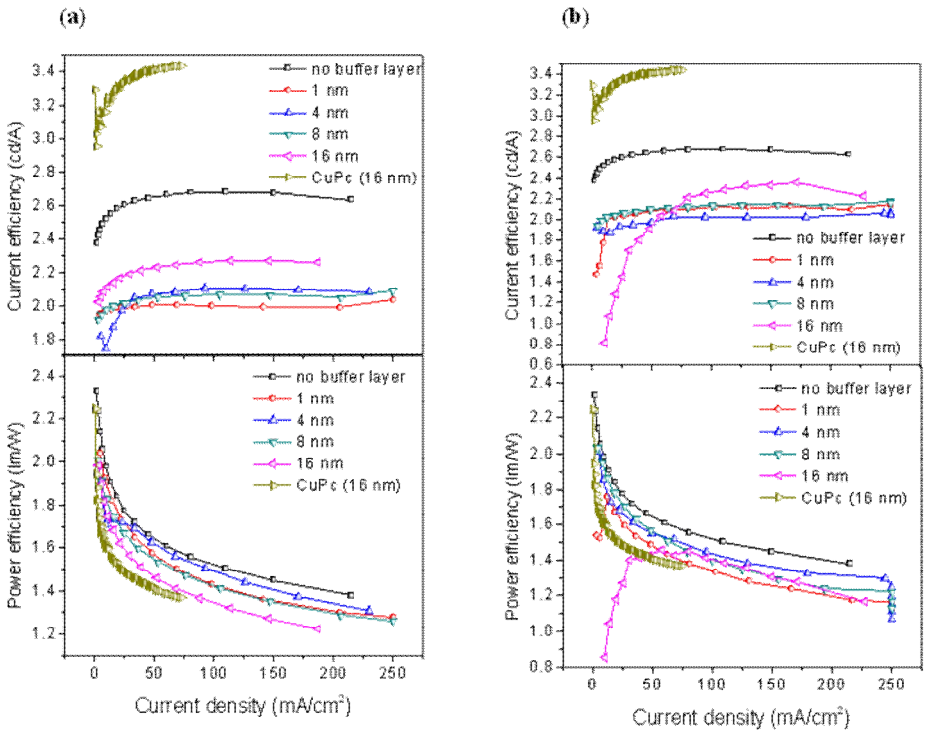

FIG. 3-6. Current and power efficiency vs. current density for OLEDs with NPB:NaCl [1:*y* wt %, *y* = 2 (a) and *y* = 30 (b)] anodic buffer layers in various thickness values. Reference device architectures are ITO/NPB/Alq_3/LiF/Al (no-buffer layer) and ITO/CuPc (16 nm)/NPB/Alq_3/LiF/Al.

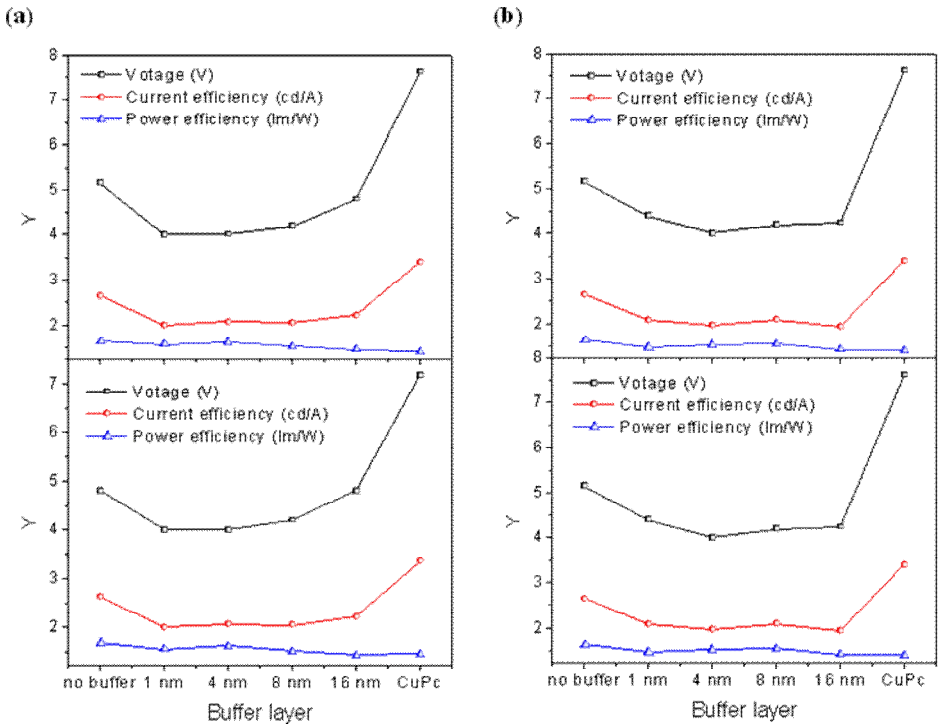

FIG. 3-7. Driving voltage, current efficiency, and power efficiency for OLEDs with different thicknesses of NPB:NaCl [1:y wt %, y = 2 (a) and y = 30 (b)] anodic buffer layers. Reference device architectures are ITO/NPB/Alq_3/LiF/Al (no-buffer) and ITO/CuPc (16 nm)/NPB/Alq_3/LiF/Al (CuPc). The data in the upper- and lower-panels were obtained at a current density of 50 mA/cm^2 and at a luminance of 1000 nit, respectively.

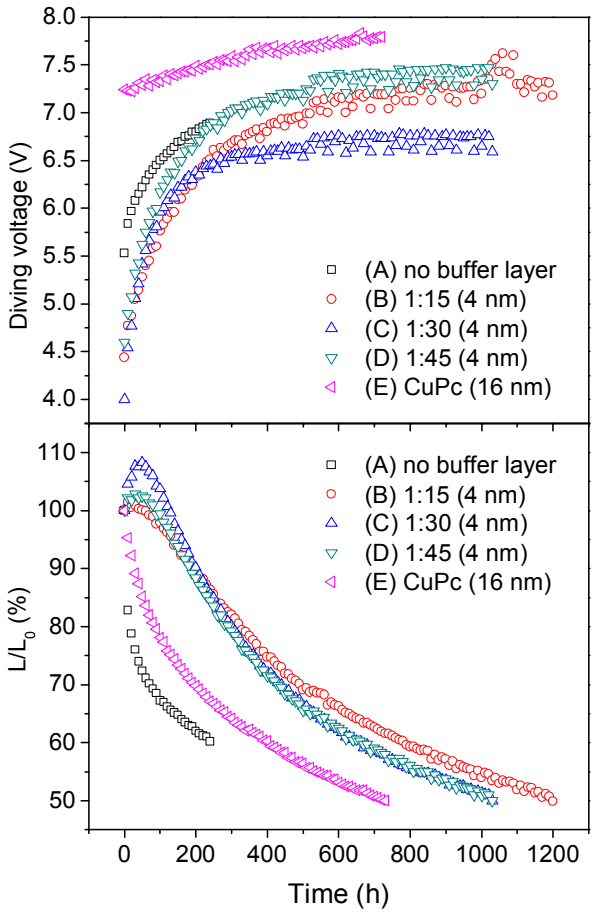

FIG. 3-8. Driving voltage and luminance changes measured in time at a constant current density of 50 mA/cm^2, as a reflection of operational stabilities for OLED devices with 4 nm thickness of NPB:NaCl (1:y wt %, y = 15, 30, and 45) buffer layers. Reference device architectures are ITO/NPB/Alq_3/LiF/Al (no-buffer layer) and ITO/CuPc (16 nm)/NPB/Alq_3/LiF/Al.

TABLE III-1. Summary of the driving voltages, luminance, current efficiencies, power efficiencies, and 70% lifetimes of devices A, B, C, D), and E shown in Fig. 8, operated at a constant current density of 50 mA/cm^2. The life time values in parentheses are calculated at an initial luminance of 1000 nit by assuming the scalable law of Coulombic degradation ($L_0\tau$ = constant, where τ is lifetime).

Device	Driving voltage (V)	Initial luminance (L_0, cd/m^2)	Current efficiency (cd/A)	Power efficiency (lm/W)	70 % life-time (h)
A	5.15	1324	2.65	1.64	70 (93)
B	4.60	1298	2.60	1.80	490 (636)
C	4.15	1015	2.03	1.55	440 (447)
D	4.86	1360	2.68	1.73	415 (564)
E	7.62	1706	3.41	1.43	190 (324)

Chapter IV

Interfacial energetics of NaCl:NPB composite layer at OLED anodes

Abstract

Although low work-function alkaline halides are widely used as a cathode interlayer for organic light-emitting diodes (OLEDs), NaCl-organic composites are shown to play an efficient anodic buffer. Here we suggest a mechanistic origin of the improved OLED performance upon the use of a NaCl-containing organic buffer layer between indium tin oxide (ITO) anode and *N,N'*-bis(naphthalene-1-yl)-*N,N'*-bis(phenyl)benzidine (NPB), based on the studies with ultraviolet photoelectron spectroscopy and atomic force microscopy. While a pure NaCl interlayer has a high hole-injection barrier (1.40 eV), the NPB:NaCl composite layer exhibits a substantially lower barrier (0.84 eV), which is comparable to the value at bare ITO/NPB interface. Furthermore, the wettability of the composite onto ITO is enhanced due to significant adhesive interactions of NaCl with both ITO and NPB, leading to effective electrical contacts. The two key factors of the plausible hole-injection barrier and the better wettability of the NPB:NaCl composite contribute to the improved hole injection efficiency and lifetime.

VI-1. Introduction

Interface engineering between electrodes and organic layers in organic light-emitting diodes (OLEDs) has been one of main technological approaches because the charge injection and device stability are strongly dependent on their interface formation [1,2]. This is why much effort has been made to improve the interface properties and understand their mechanism governing the charge injection and transport. In general, to reduce charge injection barriers, the anodic side consists of high work-function materials while the cathodic side of low work-function materials. In addition, surface or interface free energy is another important factor to be counted in terms of interfacial compatibility between inorganic and organic materials.

Various approaches have been tried to modify both the work function and surface energy of indium tin oxide (ITO), the most common transparent anode. Physical surface treatments such as oxygen plasma and ultraviolet ozone (UVO) have been widely used to enhance hole injection [3,4]. These treatments are effective in removing residual surface contaminants and inducing oxygen-rich surface at the ITO surface, leading to increase in work function through surface band bending of the ITO or interfacial dipole formation [5.6]. However, the surface treatments are not enough to obtain interfacial compatibility between the ITO and organic hole transport layer (HTL) because the plasma or UVO treatment makes the ITO surface more hydrophilic [7,8], possibly exhibiting adverse interfacial properties to most organic HTL materials with high hydrophobicity [9]. Another or additional important approach for modifying the anodic interfacial region is to

introduce metals or metal oxides with high work function [10-15], organic materials such as a star-burst amine [16] and fluorocarbon plasma polymers [17-19], and even insulators [20-23] between the ITO and organic HTL. The hole injection enhancement has been ascribed to the various mechanisms such as energy level realignment through interface dipole or surface band bending [14,24-26], interfacial stability induced from mechanical adhesion [10,21-23], or high tunnelling probability from reduced effective barrier [20].

On the other hand, metal halides which are usually applied at cathode/organic interfaces, have also been tried for better anode/organic interface property [27,28]. The application of metal halides on the anodic side can allow simpler fabrication of highly efficient OLEDs by introducing the same metal halide for both electron and hole injection enhancement. Further, metal halides are usually cheap and easy to handle, compared to transition metal oxides [14,15] or other organic molecules like buckminsterfullerene (an n-type organic semiconductor) [29,30]. LiF, the most common electron injection material on the cathode surface, was demonstrated to be effective in hole injection enhancement on hydrogen plasma treated ITO anodes but not on the ones with more practical treatments like oxygen plasma or UVO, based on the tunnelling model [31]. A composite form of metal halides such as LiF and MgF_2 with the hole transport materials improves the thermal stability of OLEDs through enhanced gradual interface energy matching [28,32]. Furthermore, we showed that a NaCl-incorporated interlayer at ITO and HTL interface improves not only the anodic interface stability but also hole injection efficiency with implication of multiple mechanistic origins for the

improved performance in the previous chapter [33]. The reasons of hole injection and device lifespan enhancement are investigated here.

To tackle the underlying mechanism of the OLED performance enhancement using the NaCl composite, the interfacial electronic and thermodynamic properties have been studied. Here, we prepared ITO/NaCl-containing buffer/*N,N'*-bis(naphthalene-1-yl)-*N,N'*-bis(phenyl)benzidine (NPB) interfaces, and measured ultraviolet photoelectron spectroscopy (UPS) and the wettability of the thin films by morphological study with atomic force microscopy (AFM). First, the hole injection barrier at the interface of ITO and NPB:NaCl composite layer was comparable to that at ITO/NPB interface, showing that NPB at the interface is kept chemically and electronically intact even in the presence of NaCl. Second, the wettability of NPB in the composite onto ITO was enhanced by the significant adhesive interactions of NaCl with both ITO and NPB, leading to effective electrical contacts across the anode side. This was supported by the calculation of interface free energies, work-of-adhesions, and spreading coefficients. These studies reveal the importance of concomitant consideration of both electronic charge injection barrier and morphological adhesion property for rational design of organic/inorganic interfaces in organic electronic devices.

VI-2. Experiments

Both the growth of thin solid layers and the UPS measurements were performed in ultrahigh vacuum system (UHV, base pressure of 10^{-9} Torr) composed of three interconnected chambers equipped for surface pretreatment, film growth and

analysis, shown in Fig. 1; the working pressure of UPS measurements was 1.5 – ~7 × 10^{-8} Torr (He-gas initially ignited under a pressure range of ~4 × 10^{-8} to 4 × 10^{-7} Torr), whereas the discharge pressure of He was about 8 × 10^{-8}. ITO-coated glass substrate with a sheet resistance of 50 Ω/cm^2 was used and UVO treatment (quartz mercury vapor lamp: UV of 185 and 254 nm) was employed to clean the substrate in the surface pretreatment chamber under a pressure of 3 Torr for 10 min.

Prior to deposition, the source materials were carefully degassed for more than 24 h after loading the organic and NaCl sources into the UHV chamber. Especially, NaCl was preheated at a temperature of lower than its evaporation temperature during the degassing to minimize the amount of adsorbed water molecules. NPB and NaCl films were deposited onto the ITO substrate by resistive heating in the film growth chamber under a working pressure of 1.3 × 10^{-8} Torr. The deposition rate was 0.01 nm/s for both NPB and NaCl layers. The mixed films of NPB:NaCl (1:3 wt %) were prepared by co-evaporation of NaCl and NPB. The composition was adjusted by changing the ratio of the deposition rates of each component, which gives directly the volume ratio of the composite film, 1:1.5 v/v. Thus, the weight ratio was obtained by considering density (d) of each component under the assumption that the density of each component in the composite is equal to that of its pure bulk: d_{NaCl} = 2.16 g/cc and d_{NPB} ~1 g/cc. In principle, acoustic impedances (Z's) of a deposited thin film (Z_f) and quartz of QCM (Z_{quartz} = 8.83) might be considered as Z-factor (i.e., Z_{quartz}/Z_f, e.g., Z-factor of NaCl = Z_{quartz}/Z_{NaCl} = 1.57) for more accurate thickness measurement of the thin film with QCM. However, when the thin film deposited on the quartz surface of the QCM is very

thin (i.e., crystal life larger than 90%), the acoustic impedance variation of QCM due to thin film deposition is negligible: when the thickness of deposited thin film is larger than a few thousand nm (i.e., crystal life less than ~50%), the acoustic variation becomes significant to affect the accuracy of thickness measurement with QCM. The prepared thin films deposited onto the ITO substrates were transferred into the analysis chamber by using the loading bar without breaking the vacuum condition of the deposition chamber.

UPS spectra acquisition was performed in the analysis chamber using the unfiltered He I (21.2 eV) radiation lines of the gas discharge lamp and hemispherical electron energy analyzer (VG ESCALAB 220i system). At each step of interface formation, the valence band and the onset of photoemission were recorded. The secondary electron cutoff, which represented the vacuum level, was measured with a bias of –10 V on the sample to clear the vacuum level of the detector, whereas the valence band edge was obtained under a bias of –5 V. Vacuum level shifts and HOMO level changes induced by the NPB or NPB:NaCl composite over-layers were thus measured.

Surface morphologies were investigated by using AFM (Dimension 3100, Veeco Digital Instruments). Tetrahedral Si tip (8 nm tip radius) was used in tapping mode. Scan area, scan rate, and image resolution are 2 × 2 μm^2, 1.5 Hz, and 256 points per line, respectively.

VI-3. Results and discussion

The evolutions of secondary electron cut-off and valence region spectra for NPB/ITO with increasing coverage are shown in Fig. 2. The shape of the UPS spectrum agrees well with the previous report along the measured whole energy range, showing the characteristic features of the highest occupied molecular orbital (HOMO) corresponding to the central biphenyl unit of NPB [3,34]. All spectra were plotted with respect to the Fermi level (E_F). The normalized secondary cutoff edges of NPB are shown on the left panel of the UPS data in Fig. 2. The vacuum levels of the samples were determined by linear extrapolation of secondary electron cutoffs on the high-binding-energy side of the UPS spectra (15 – 19 eV). The vacuum level shifts abruptly toward higher binding energy for the first sub-monolayer deposition (nominal thickness of 0.2 nm) by 0.24 eV, thus indicating the presence of interface dipole as previously reported [35,36]. As the NPB layer becomes thicker after the second step of deposition, the vacuum levels shift gradually toward higher binding energies. The final secondary cutoff edge is assigned to the 4 nm thickness NPB spectrum. The right panel of figure 2 shows HOMO onsets for NPB. The HOMO onset was determined by linear-extrapolation of the leading edge (closer to the Fermi level) in the spectrum and is found at 0.84 eV for NPB (0.2 nm)/ITO below E_F, followed by gradual higher-binding-energy shift with the further increase in NPB thickness.

To investigate the electronic effect of NaCl-containing interlayer between ITO and NPB, NaCl was deposited on the ITO surface in the forms of both pure NaCl layers and NPB:NaCl mixed layers. Figure 3(a) shows the secondary electron cutoffs and HOMO regions of UPS spectra for the samples

containing pure NaCl interlayer between NPB and ITO. The secondary cutoff shifts abruptly toward higher binding energy at low coverages under 0.5 nm thickness by 0.26 eV, and then saturates at the thickness of 1.0 nm. As soon as the NPB was deposited on the pre-deposited NaCl surface, the secondary cutoff shifts abruptly again in the same direction by ca. 0.3 eV, and then moves gradually toward higher binding energies with the further deposition of NPB. Thus interface dipoles are expected to be present at the both sides of NaCl interlayer between NPB and ITO. In the right panel of figure 3(a), HOMO features are well observed on the NaCl surface, showing that the onset of HOMO at the low coverage of 0.2 nm thickness is 1.40 eV and then shifts slowly toward higher binding energy with the increase in NPB coverage. Features above the HOMO level or in the energy gap are replica of the valence state due to the weak He I-line from the unfiltered He I discharge lamp. Differently from the pure NaCl interlayer, the mixed film type of NPB:NaCl shows relatively pronounced gradual shift of the secondary cutoff toward higher binding energy during the deposition of the composite by 0.59 eV rather than sudden shift(s)shown on the left part of the figure 3(b). The HOMO features of NPB in NPB:NaCl mixed phase are well observed even though the intensities are relatively weak at lower coverages of the composite, shown in the right panel of figure 3(b). The shapes and widths of the NPB HOMO features in the mixed phase are found to be similar to those of the HOMO features of pure NPB over-layer, implying that NPB in the mixed phase with NaCl is kept chemically intact. Although the HOMO cutoff position of NPB:NaCl with 0.2 nm thickness is hard to be assigned because of weak signal from NPB, we could extract the position to be 0.84 eV by

considering the lower binding energy shift of the observed HOMO maximum by 0.16 eV from that of NPB:NaCl with 0.5 nm thickness as marked on the right panel of figure 3(b).

Work-functions or vacuum levels, and HOMO onsets with different NPB coverages were extracted and summarized for each sample, shown in Fig. 4: since the Fermi level is fixed, the change of the secondary cutoff corresponds directly to the work-function or vacuum level change. The HOMO onset corresponds to the position of the lowest energy hole-state (namely, the HOMO of the molecular cation in the bulk). The hole energy shifts to lower energy due to the polarization energy induced on the surrounding medium by the photo-induced hole, compared to the adiabatic system like gas-phase molecule, shown in Fig. 5 (a) and (b). For more collective understanding, the HOMO-LUMO gap measured by using UPS and IPES (inverse photoemission spectroscopy) and the expected polaron levels are displayed in Fig. 5. The polarization includes an electronic response of the electron charge density (~10^{-16} s), and a vibronic response of the molecular cation (~10^{-15}–10^{-14} s). Since the kinetic energy of the photoemission electron is about 15 eV, the electron moves distances of 1–2 nm in 1–5 × 10^{-15} s hence both polarization responses affects on the UPS spectrum. However, the lattice relaxation response of lattice phonons (~10^{-13} s) is considered to be too slow to contribute to photoemission (namely, small corrections ~10%) [37,38]. The surface transport gap (Φ^{S}_{t}) might be evaluated from the HOMO-LUMO gap ($\Phi^{UPS/IPES}$: a distance between the centroids of the HOMO and LUMO peaks) measured with the surface sensitive UPS/IPES (the escape depth of UPS is from sum-monolayer to ~10 nm

and that of IPES is more limited.) via correction for a vibrational contribution: the vibrational excitation in UPS and IPES tends to shift both the measured HOMO and LUMO peaks away from the Fermi level (~0.1 eV for each peak) [37]. The (bulk) transport gap (Φ_t) and its corresponding polaron levels (E_P^- and E_P^+), which are related to the minimum energy of formation of a separated free electron and hole, and very close to the onset of optical absorption (Φ_{opt}: Frenkel exciton with the electron and hole on the same molecule), would be evaluated from further correction for bulk polarization; Φ^S_t is larger than Φ_t because vacuum is not polarizable (namely, the polaron levels in bulk are more stabilized by ~0.3 eV) [37,39]. This transport gap is used for accurate modeling of charge carrier injection at the interfaces. The difference between polaron level gaps obtained from the adiabatic system and the condensed phase is the polarization energy ($P_- + P_+$), and $\Phi_t - \Phi_{opt}$ is considered as exciton binding energy [37]. However, short of informative accurate correction values, especially, in amorphous organic semiconductors, the measured polaron levels from the UPS/IPES have been generally evaluated from HOMO or LUMO onset (not the centroids of HOMO and LUMO peaks). Another polarization source originates from the interface of the organic semiconductor and electrode substrate through image charges of the adjacent electrode surface. Plausible positions of the energy levels of the organic layer on the metallic substrate from interface to film surface are given in Fig. 6. When only the polarization effect of the substrate is considered, the polarons identified at the onsets of HOMO and LUMO ($HOMO^{(UPS)}$ and $LUMO^{(IPES)}$) from UPS/IPES will be more stabilized near the interface, showing nearly symmetric

curves each other from interface to the film surface (Fig. 6(a)). However, when LUMO or HOMO-derived level of ground state (N electrons) of the film is pinned near the Fermi level of the metallic electrode at the interface through charge transfer, the energy levels (HOMO, LUMO, and vacuum level) of the ground state will be bended, shown in Fig. 6(b) and (c) with dashed lines, except for the Fermi levels which are not bendable. Thus, $HOMO^{(UPS)}$ and $LUMO^{(IPES)}$ levels, which represent the final states of N–1 and N+1 electrons, respectively, are bended by collective effects from the polarization of substrate and the intrinsic band-bending caused by the E_F level pinning. Fig. 6 (b) shows that the $LUMO^{(IPES)}$ level bended by the polarization of substrate is further bended by the E_F level pinning near the LUMO level while the $HOMO^{(UPS)}$ level bending caused by the substrate polarization effect is compensated by the E_F level pinning. Fig. 6 (c) corresponds to the opposite case of Fig. 6 (b). Here, it is noticeable that the vacuum level is not affected by the final state effect of UPS measurement (i.e., N–1 electrons) because the vacuum level (E_{vac}) is obtained from the difference between the Fermi and secondary cut-off levels, hence the final state effect is nullified, and E_{vac} (for ground state of N electrons) is measured as well as the HOMO level for $N - 1$ electrons with UPS [40]. Therefore, if the polarization effect of substrate is significant, the difference between $HOMO^{(UPS)}$ and E_{vac} (i. e., ionization energy) would increase from the interface to the film surface.

In the present investigation, the screening effect for the $N - 1$ electrons' final state will be caused by polarization of not only adjacent NPB molecules, but also ITO substrate image charges. For all samples, both surface work-functions and

HOMO onsets shift downward in almost the same degree with increase in NPB or NPB:NaCl thickness. Thus the polarization effect on the inorganic substrate (ITO) could be considered as negligible, maybe due to fewer free electrons (~10^{20}/cm^2) of the ITO than the metal (~10^{22}/cm^2) [41]. Otherwise, a difference in the HOMO and vacuum level shifts from interface to film surface would be observed by the substrate polarization effect upon photo-ionization [40]. Thus, the overall downward shifts are mainly attributed to the space charge redistribution [36,42], compensating the interface dipole formation.

Combining the changes of HOMO cutoffs and vacuum levels based on the data in Fig. 4, we draw the schematic energy level diagrams of NPB/ITO, NPB/NaCl/ITO, and NPB/NPB:NaCl/ITO interfaces as shown in Fig. 7. The band bending (i. e., an indicative of the presence of space charge region) and interface dipole were evaluated from the shifts of HOMO onsets and vacuum level changes, respectively. Pure NaCl interlayer raises the hole injection barrier from ITO to NPB by 0.56 eV compared to the direct contact of ITO/NPB. The specific mechanisms related to the charge injection efficiency might be extremely complex, but it is clear that the higher hole injection barrier contributes to the higher turn-on voltage of OLEDs with a pure NaCl thin film buffer in the previous report [27]. Meanwhile, the injection barrier of NPB:NaCl on ITO is comparable to that of pure NPB on ITO, implying that the NPB maintains its intrinsic injection property even in the composite phase on the ITO surface. Further, the pure NaCl interlayer between ITO and NPB shows two stepwise decreases of the vacuum level by the interface dipoles formed at both sides of the interlayer, whereas the NPB:NaCl

composite layer shows a gradual decrease throughout the mixed phase. Total vacuum level change from ITO to the NPB:NaCl/NPB interface is 0.59 eV in figure 7(c), which is similar to that of 0.60 eV from ITO to the NaCl/NPB interface in figure 7(b). Thus, the vacuum level suppressing character of NaCl observed in the pure NaCl interlayer between the NPB and ITO through interface dipole formation is expressed as a large band bending in the mixed phase of the NPB:NaCl composite interlayer, even though the origin of the large band bending is not clearly revealed yet. Due to the large band bending in the mixed phase, the HOMO level is relatively far from the Fermi level at a thickness of 4 nm (1.28 eV) compared to that of pure NPB at the same nominal thickness (1.09 eV).

Based on the above energy level alignment diagrams, the schematic energy level changes for pure NPB and NPB:NaCl composite layers on ITO under a bias condition are compared in Fig. 8(a) and (b), respectively. When the forward bias is applied, NPB:NaCl creates higher electric field due to its large resistivity induced by the insulating property of NaCl compared to the pure NPB. Thus a larger energy level gradient in the mixed buffer layer reduces the tunnelling barrier, which is approximately displayed by the shaded areas in Fig. 8(b) [31,43-45]. Compared to the barrier of the pure NPB layer in Fig. 8(a), this reduced effective tunnelling barrier may lead to the easier hole injection into HTL through the NPB:NaCl buffer layer. Therefore, the hole injection enhancement could be partially attributed to the tunnelling mechanism [1,43,46].

Since the wettability of the charge injection or transport layer onto the electrode has been another factor counting charge injection efficiency [47],

affecting orbital overlap distance, the surface morphologies of pure NPB and NPB:NaCl composite (1:7 wt %) films were compared by AFM images. ITO surface is hydrophilic mainly due to its hydroxyl functional groups while the arylamine is hydrophobic. The surface energy mismatch at the ITO/NPB interface introduces a micro-structural instability, weakening interfacial affinity and possibly leading to interfacial decohesion at or near the glass transition temperature of NPB. Therefore, the NPB:NaCl mixed phase is considered to alleviate the interfacial instability from hydrophilic nature of the ionic compound, NaCl.

In generally, higher surface energy of substrate is beneficial to a smooth growth of films (i.e., layer growth mode) and a strong adhesion of the film, whereas island growth mode corresponds to a relatively low surface energy of the substrate where arrived species tend to migrate to active sites and finally add to pre-existing stable nuclei. On the other hand, a useful estimate for film growth modes is based on a uniform surface free energy of the substrate and macroscopic surface tensions as follows [48]:

$$\gamma_{O/S} + \gamma_O - \gamma_S = \Delta\gamma, \quad (1)$$

where $\gamma_{O/S}$, γ_O, and γ_S are the interface free energy at the overlayer/substrate interface, overlayer/vacuum interface, and substrate/vacuum interface, respectively. Here, the growth mode is expected to be complete wetting (Frank-Van der Merwe type, i.e., layer growth mode) when $\Delta\gamma < 0$, Stranski-Krastanov type when $\Delta\gamma \cong 0$, and Volmer-Weber (V-W) type when $\Delta\gamma > 0$, shown in Fig. 9(a). Thus, the surface roughness of the film on the substrate decreases with the decrease of surface free energy of the film, which means that strong adhesion of the film does not always

reflect a smooth surface (lowered surface roughness) because the adhesion increases with the surface free energy of the film. Furthermore, in most thin film deposition processes, nucleation occurs at some preferential sites on the substrate (i.e., imperfect surface), such as (sub-) grain boundaries [49], dislocations or other surface defects [50,51], where the surface energy is remarkably higher than the rest of the surface. Thus, the adsorbed molecules or particles are locked or irreversibly trapped on to the surface defects and grow into stable nuclei, because the energy barrier for nucleation is significantly lower at high surface energy areas. As shown in Fig. 10(a), the polycrystalline ITO surface is characterized with a submicron-scaled (sub-) grain structure. Thus, from micro-point of view, surface energy of the ITO surface should be accordingly varied from place to place, leading to the island growth mode of NPB film as shown in Fig. 10(b), which consists with previous results [7]. While the NPB film (4 nm) forms large aggregates, showing numerous dewetting spots on the revealed ITO grain pattern with a root mean square (RMS) roughness value of 5.13 nm, the pure NaCl thin film (4 nm) shows very uniform grain growth with of a lower roughness value of 4.09 nm [Fig. 10(c)]. Indeed in Fig. 10(d), the surface morphology of NPB:NaCl composite film follows that of the pure NaCl film with a lowered RMS roughness of 4.17 nm, compared to the pure NPB film. The NPB aggregates are no longer observed from the morphology of the composite film, implicating that NPB and NaCl are well intermixed and more wettable on the ITO surface. With the increase in the film thickness, the surface roughness of the composite film increases more rapidly and surpasses that of the pure NPB. The RMS roughness values at 8 nm thickness for pure NPB and

NPB:NaCl composite films are 6.06 and 6.86 nm, respectively, shown in figure 10(e) and (f). Therefore, NaCl affects significantly the film growth mode in the NaCl:NPB mixed film. The film wetting and growth behavior can be more precisely described by work-of-adhesion and spreading coefficient rather than only by surface roughness values (Fig. 9(b). The interfacial free energy, work of adhesion (W^A), and spreading coefficient (S) were calculated, according to the Equations (1), (2), and (3) [52,53]:

$$W^A_{A/B} = \gamma_A + \gamma_B - \gamma_{A/B}, \quad (2)$$

$$S_{A/B} = \gamma_B - \gamma_A - \gamma_{A/B}, \quad (3)$$

and

$$\gamma_{A/B} = (\gamma_A^{1/2} - \gamma_B^{1/2})^2, \quad (4)$$

where $\gamma_{A/B}$ is the interfacial free energy of A/B interface, γ_A is the surface free energy of A, $W^A_{A/B}$ is the work of adhesion between A and B, and $S_{A/B}$ is the spreading coefficient of A on the surface B. The Eq. (2) and (3) could be conceptually defined or understood as follows: (2) work-of-adhesion increases when the A/B interface formation is favorable (hence less A/B interfacial free energy) and the surface formation of A and B is unfavorable (hence higher surface free energy of A and B), and (3) the spreading of A on the surface B increases when both A/B interface formation and surface formation of A is favorable (hence less A/B interfacial free energy and less surface free energy of A) and the surface formation of B is unfavorable (hence higher surface free energy of B). The Eq. (4) is based on the geometric mean method by Berthelot. The surface free energies of NPB, NaCl, and ITO were referenced from the reported values, 31.1, 227, and 70.1

mJ/m^2, respectively [54-56]. Table 1 exhibits the summarized values of $\gamma_{A/B}$, $W^A_{A/B}$, and $S_{A/B}$ where A/B is NPB/ITO, NaCl/ITO, or NPB/NaCl. Although the interface free energy of NPB/ITO interface is less than that of NaCl/ITO interface, NaCl shows higher work of adhesion (252 mJ/m^2) onto the ITO surface than that of NPB (93.4 mJ/m^2) due to the high surface free energy of NaCl, but its spreading coefficient is less and even negative (–202 mJ/m^2). It means that the NaCl is strongly adhesive to the ITO surface but not so wettable on it – reminiscent of V-W film growth mode in which three-dimensional crystallites nucleate immediately upon contact [48]. As indeed mentioned in the above AFM results (namely, rapid increase in surface roughness of the composite film), NaCl in NPB:NaCl mixed film makes the composite film growth mode close to the V-W type, preventing the NPB aggregation observed in pure NPB film. Furthermore, NPB is expected to be significantly adhesive to NaCl from the high W^A of NPB:NaCl (168 mJm/^{2}), as confirmed by AFM images showing well-intermixed uniform morphologies in figure 10(d) and (f). NaCl, thus anchoring to the ITO surface with its relatively high W^A, seems to facilitate the contact between ITO electrode and NPB by suppressing the cohesive interactions between NPB molecules and simultaneously inducing moderate adhesive interactions between NPB and NaCl, shown in Fig. 11. The charge injection rate increases exponentially with decrease in orbital overlap distance [57,58]. Therefore, such a morphological effect caused by NaCl incorporation into the NPB film contributes to the previous report of hole injection enhancement by the better mechanical adhesion, leading to the "effective" electrical contacts and prolonged lifetime. Additionally, the negative effect

observed on the *J-V* curve for an OLED device with small amount of NaCl in the composite buffer is attributed not to the decrease of electric contact area between NPB and ITO but to NPBs.

On the other hand, the NPB, of which glass transition temperature (Tg) is 98 °C [59], in NPB:NaCl composite film may be more susceptible to micro- or nano-scale crystallization on the ITO substrate due to the adjacent hot NaCl clusters originated from the NaCl source material with higher melting point (MP) of 801 °C during the co-deposition. An enhanced device storage stability in air was reported by inducing partial crystallization of NPB via elevating the deposition temperature through heating the sample substrate up to 140 °C [60,61], in contrast to the common belief that crystallization of the organic layers is among the most reported degradation mechanisms [62]. Although the mechanistic relationship between the enhanced stability and the incorporation of a crystalline hole transport material is still unclear, the local crystallization might be contributable to the increase in hole mobility. The proposed mechanistic origin based on the local crystallization by hot source materials would be also expandable to the cathode side which adopted electron injection materials with high melting temperature like LiF (MP 845 °C) by inducing partial crystallization of the pre-deposited electron transport materials like Alq3 with Tg of 175 °C [63].

Thus, to investigate the crystallinity of the thin films, Raman spectra were obtained using a Renishaw Raman system Model 2000 spectrometer equipped with an integral microscope (Olympus BH2-UMA) and the excitation source of 632.8 nm line from 17 mW He/Ne laser. The laser beam was focused onto a spot of

approximately 1 μm diameter by using an objective microscope with a magnification of 50×. The data acquisition time was 20 s in the spectral resolution of 1 cm^{-1}. The Raman band of a silicon wafer at 520 cm^{-1} was used with an estimated measurement accuracy of better than 1 cm^{-1}. Pure NPB (50 nm) films, and mixed films of NPB:NaCl (100 nm, 1:x v/v, x = 1, 2, and 3) on ITO substrates were prepared in the deposition chamber, transferred to the other site for Raman spectroscopic analyses under vacuum-packaging of the samples, and then exposed to air for the measurement of Raman spectroscopy. According to the previous report, only crystalline NPB shows characteristic features while as-deposited NPB (amorphous) does not show any peaks [60]. In this work, however, even pure NPB films, which would be amorphous and were expected not to show any Raman peaks, shows the same characteristic peaks of NPB as the other NPB:NaCl composite films shown in Fig. 12; the peaks, which were referenced from the previous reports [61,64], decrease with decrease in the nominal amount of NPB in films. Crystallization temperature of a material can be very sensitive to its purity and NPB, especially, was reported to be crystallized more easily through up-taking water vapor, even below 45°C [65]. Heat source of the crystallization might be the laser beam from Raman spectrometer. Although we could not find a low power condition of the spectrometer to rule out the possibility of laser-induced crystallization of NPB, more careful handling of samples would be also necessary especially to inhibit the intake of ambient moisture: the organic materials such as NPB and Alq3 were reported to be accelerated by moisture [49,65].

VI-4. Conclusions

We investigated the role of NaCl thin film and NPB:NaCl composite layer as anodic buffer between ITO anode and NPB transport layer by using UPS and AFM measurements. The hole injection barrier increased with the insertion of the pure NaCl layer compared to the interface without buffer layer. NPB:NaCl composite, however, shows nearly identical injection barrier to that of the NPB/ITO interface. Furthermore, the NaCl in NPB:NaCl mixed film assists the mechanical adhesion and resultant electrical contact between ITO and NPB through better wettability of the mixed film on ITO surface. As a whole the tunnelling through the highly resistive composite layer with a comparable injection barrier height and enhanced electrical contact are associated with the improved performance of the OLEDs using NPB:NaCl composite anodic buffer. To achieve high-end OLEDs, the interface control in terms of both electronic charge injection barrier and mechanical adhesion is necessary.

References

[1] I. D. Parker, *J. Appl. Phys*. **75**, 1656 (1994).

[2] G. G. Malliaras and J. C. Scott, *J. Appl. Phys*.**83**, 5399 (1998).

[3] X. M. Ding, L. M. Hung, L. F. Cheng, Z. B. Deng, X. Y. Hou, C. S. Lee, and S. T. Lee, *Appl. Phys. Lett.* **76**, 2704 (2000).

[4] K. Sugiyama, H. Ishii, Y. Ouchi, and K. Seki, *J. Appl. Phys.* **87**, 295 (2000).

[5] D. J. Milliron, I. G. Hill, C. Shen, A. Kahn, and J. Schwartz, *J. Appl. Phys.* **87**, 572 (2000).

[6] S. Y. Kim, J. –L. Lee, K. –B. Kim, and Y. –H. Tak, *J. Appl. Phys.* **95**, 2560 (2004).

[7] Z. H. Huang, X. T. Zeng, X. Y. Sun, E. T. Kang, J. Y. H. Fuh, and L. Lu, *Org. Electron.* **9**, 51 (2008).

[8] J. S. Kim, R. H. Friend, and F. Cacialli, *J. Appl. Phys.* **86**, 2774 (1999).

[9] J. Cui, Q. L. Huang, J. C. G. Veinot, H. Yan, Q. Wang, G. R. Hutchison, A. G. Richter, G. Evmenenko, P. Dutta, and T. J. Marks, *Langmuir* **18**, 9958 (2002).

[10] Y. Shen, D. B. Jacobs, G. G. Malliaras, G. Koley, M. G. Spencer, and A. Ioannidis, *Adv. Mater.* **13**, 1234 (2001).

[11] I. –M. Chan, and F. C. Hong, *Thin Solid Films* **450**, 304 (2004).

[12] J. –M. Moon, J. –H. Bae, J. –A. Jeong, S. –W. Jeong, N. –J. Park, H. –K. Kim, J. –W. Kang, J. –J. Kim, and M. –S. Yi, *Appl. Phys. Lett.* **90**, 163516 (2007).

[13] W. Hu, K. Manabe, T. Furukawa, and M. Matsumura, *Appl. Phys. Lett.* **80**, 2640 (2002).

[14] H. M. Zhang, and W. C. H. Choy, *IEEE Trans. Electron Devices* **55**, 2517 (2008).

[15] H. You, Y. Dai, Z. Zhang, and D. Ma, *J. Appl. Phys.* **101**, 026105 (2007).

[16] S. –F. Chen, and C. –W. Wang, *Appl. Phys. Lett.* **85**, 765 (2004).

[17] S. W. Tong, C. S. Lee, Y. Lifshitz, D. Q. Gao, and S. T. Lee, *Appl. Phys. Lett.* **84**, 4032 (2004).

[18] L. S. Hung, L. R. Zheng, and M. G. Mason, *Appl. Phys. Lett.* **78**, 673 (2001).

[19] C. –C. Hsiao, C. –H. Chang, H. –H. Lu, and S. –A. Chen, *Org. Electron.* **8**, 343 (2007).

[20] C. Qiu, Z. Xie, H. Chen, M. Wong, and H. S. Kwok, *J. Appl. Phys.* **93**, 3253 (2003).

[21] C. O. Poon, F. L. Wong, S. W. Tong, R. Q. Zhang, C. S. Lee, and S. T. Lee, *Appl. Phys. Lett.* **83**, 1038 (2003).

[22] Z. B. Deng, X. M. Ding, S. T. Lee, and W. A. Gambling, *Appl. Phys. Lett.* **74**, 2227 (1999).

[23] A. Gyoutoku, S. Hara, T. Komatsu, M. Shirinashihama, H. Iwanaga, and K. Sakanoue, *Synth. Met.* **91**, 73 (1997).

[24] S. Y. Kim, K. Hong, and J. –L. Lee, *Appl. Phys. Lett.* **90**, 183508 (2007).

[25] H. Lee, S. W. Cho, K. Han, P. E. Jeon, C. –N. Whang, K. Jeong, K. Cho, and Y. Yi, *Appl. Phys. Lett.* **93**, 043308 (2008).

[26] S. W. Tong, K. M. Lau, H. Y. Sun, M. K. Fung, C. S. Lee, Y. Lifshitz, and S. T. Lee, *Appl. Surf. Sci.* **252**, 3806 (2006).

[27] S. W. Shi, D. G. Ma, and J. B. Peng, *Eur. Phys. J. Appl. Phys.* **40**, 141 (2007).

[28] S. Tokito, and Y. Taga, *Appl. Phys. Lett.* **66**, 673 (1995).

[29] Y. Y. Yuan, S. Han, D. Grozea, and Z. H. Lu, *Appl. Phys. Lett.* **88**, 093503 (2006).

[30] Y. Yuan, D. Grozea, and Z. H. Lu, *Appl. Phys. Lett.* **86**, 143509 (2005).

[31] J. M. Zhao, S. T. Zhang, X. J. Wang, Y. Q. Zhan, X. Z. Wang, G. Y. Zhong, Z. J. Wang, X. M. Ding, W. Huang, and X. Y. Hou, *Appl. Phys. Lett.* **84**, 2913 (2004).

[32] D. Grozea, A. Turak, Y. Yuan, S. Han, Z. H. Lu, and W. Y. Kim, *J. Appl. Phys.* **101**, 033522 (2007).

[33] J. Kim, M. Kim, J. W. Kim, Y. Yi, and H. Kang, *J. Appl. Phys.* **108**, 103703 (2010).

[34] R. Q. Zhang, C. S. Lee, and S. T. Lee, *J. Chem. Phys.* **112**, 8614 (2000).

[35] P. He, S. D. Wang, W. K. Wong, C. S. Lee, and S. T. Lee, *Appl. Phys. Lett.* **79**, 1561 (2001).

[36] H. Ishii, K. Sugiyama, E. Ito, and K. Seki, *Adv. Mater.* **11**, 605 (1999).

[37] I. G. Hill, A. Kahn, Z. G. Soos, and R. A. Pascal, Jr. *Chem. Phys. Lett.* **327**, 181 (2000).

[38] E. A. Silinsh and V. Capek, *Oragnic Molecular Crystals: Interaction, Localization and Transport Phenomena* (American Institute of Physics, New York, 1994).

[39] W. R. Salaneck, *Rhys. Rev. Lett.* **40**, 60 (1978).

[40] W. Gao, and A. Kahn, *J. Appl. Phys.* **94**, 359 (2003).

[41] Z. Qiao, R. Latz, and D. Mergel, *Thin Solid Films* **466**, 250 (2004).

[42] L. Yan, M. G. Mason, C. W. Tang, and Y. Gao, *Appl. Surf. Sci.* **175**, 412 (2001).

[43] S. T. Zhang, X. M. Ding, J. M. Zhao, H. Z. Shi, J. He, Z. H. Xiong, H. J. Ding, E. G. Obbard, Y. Q. Zhan, W. Huang, and X. Y. Hou, *Appl. Phys. Lett.* **84**, 425 (2004).

[44] J. M. Zhao, Y. Q. Zhan, S. T. Zhang, X. J. Wang, Y. C. Zhou, Y. Wu, Z, J. Wang, X. M. Ding, and X. Y. Hou, *Appl. Phys. Lett.* **84**, 5377 (2004).

[45] X. J. Wang, J. M. Zhao, Y. C. Zhou, X. Z. Wang, S. T. Zhang, Y. Q. Zhan, Z. Xu, H. J. Ding, G. Y. Zhong, H. Z. Shi, Z. H. Xiong, Y. Liu, Z, J. Wang, E. G. Obbard, X. M. Ding, W. Huang, and X. Y. Hou, *J. Appl. Phys.* **95**, 3828 (2004).

[46] Y. –E. Kim, H. Park, J. –J. Kim, *Appl. Phys. Lett.* **69**, 599 (1996).

[47] J. Cui, Q. Huang, J. C. G. Veinot, H. Yan, Q. Wang, G. R. Hutchison, A. G. Richter, G. Evmenenko, P. Dutta, and T. J. Marks, *Langmuir* **18**, 9958 (2002).

[48] A. Zangwill, *Physics at Surfaces* (Cambridge University Press, 1988).

[49] T. Furuhara, and T. Maki, *Mater. Sci. Eng. A* **312**, 145 (2001).

[50] Y. Han, D. Kim, J.-S. Cho, Y.-W. Beag, and S.-K. Koh, *Thin Solid Films* **46**, 58 (2006).

[51] C. Ratsch, and J. A. Venables, *J. Vac. Sci. Technol. A* **21**, S96 (2003).

[52] T. Murakami, S. –i. Kuroda, and Z. Osawa, *J. Colloid Interface Sci.* **202**, 37 (1998).

[53] A. W. Adamson, *Physical Chemistry of Surfaces* (A Wiley-Interscience publication, 1990).

[54] J. K. Kim, J. W. Park, H. Yang, M. Choi, J. H. Choi, and K. Y. Suh, *Nanotechnology* **17**, 940 (2006).

[55] G. A. Somorjai, *Introduction to Surface Chemistry and Catalysis* (A Wiley-Interscience publication, 1994).

[56] Z. Z. You, and J. Y. Dong, *J. Colloid Interface Sci*. **300**, 697 (2006).

[57] J. R. Sheats, H. Antoniadis, and M. Hueschen, *Science* **273**, 884 (1996).

[58] J. R. Sheats, and D. B. Roitman, *Synth. Met.* **95**, 79 (1998).

[59] C. H. Chen, J. Shi, and C. W. Tang, *Macromol. Symp.* **125**, 1 (1997).

[60] Z. Q. Gao, W. Y. Lai, T. C. Wong, C. S. Lee, I. Bello, and S. T. Lee, *Appl. Phys. Lett.* **74**, 3269 (1999).

[61] Z. Q. Gao, W. Y. Lai, T. C. Wong, C. S. Lee, I. Bello, and S. T. Lee, *Appl. Phys. Lett.* **77**, 3115 (2000).

[62] T. Mori, S. Miyake, and T. Mizutani, *Jpn. J. Appl. Phys.* Part 2, **34**, L845 (1995).

[63] K. Naito and A. Miura, *J. Phys. Chem*. **97**, 6240 (1993).

[64] M. D. Halls, C. P. Tripp, and H. B. Schlegel, *Phys. Chem. Chem. Phys*. **3**. 2131 (2001).

[65] M. S. Xu, J. B. Xu, and J. An, *Appl. Phys. A* **81**, 1151 (2005).

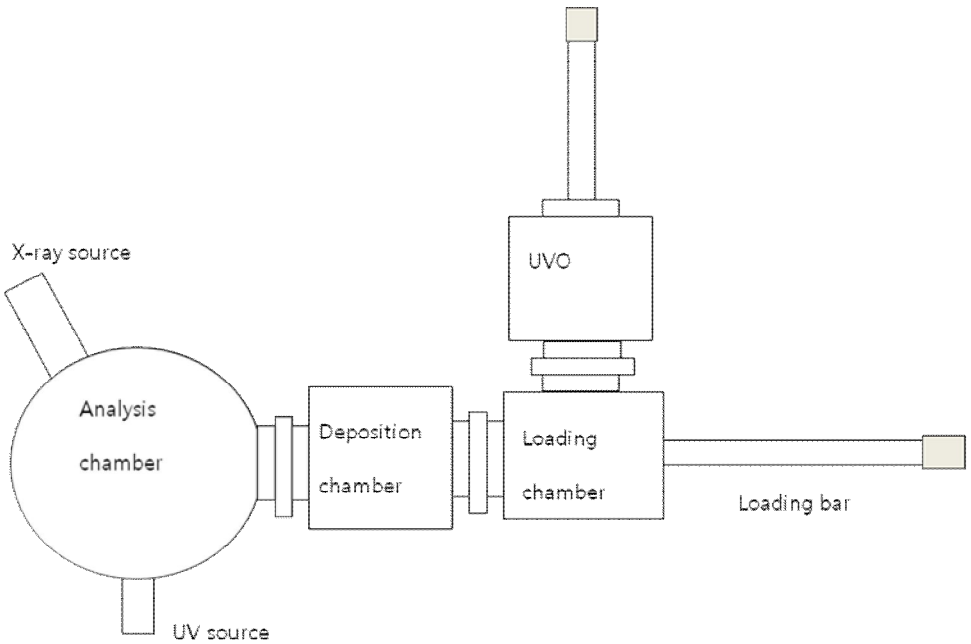

FIG. 4-1. Schematic diagram of the photoelectron measurement system. The deposition chamber is attached to the analysis chamber for in-situ interface analysis and UVO surface treatment apparatus connected to the loading chamber for cleaning the sample surfaces.

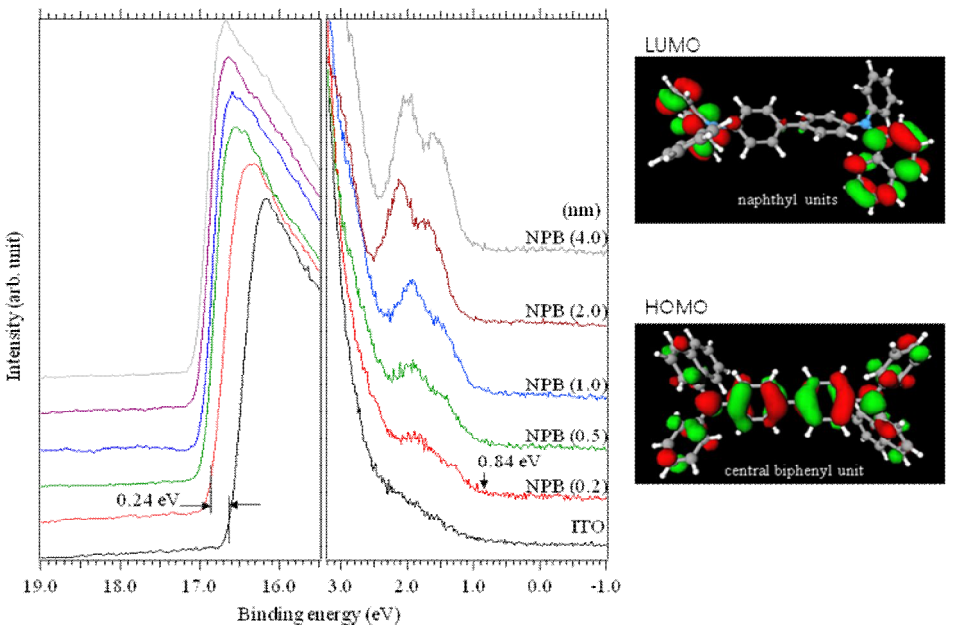

FIG. 4-2. UPS spectra collected near the Fermi level and secondary cutoff region during the step-by-step layer deposition of NPB on the ITO substrate. The HOMO features correspond mainly to the central biphenyl unit shown through the molecular orbital simulation shown in the right side of the UPS data whereas the LUMO levels are attributed to the naphthyl units of NPB (NPB was optimized using B3LYP density functional and 6-31G* basis set in DFT level)

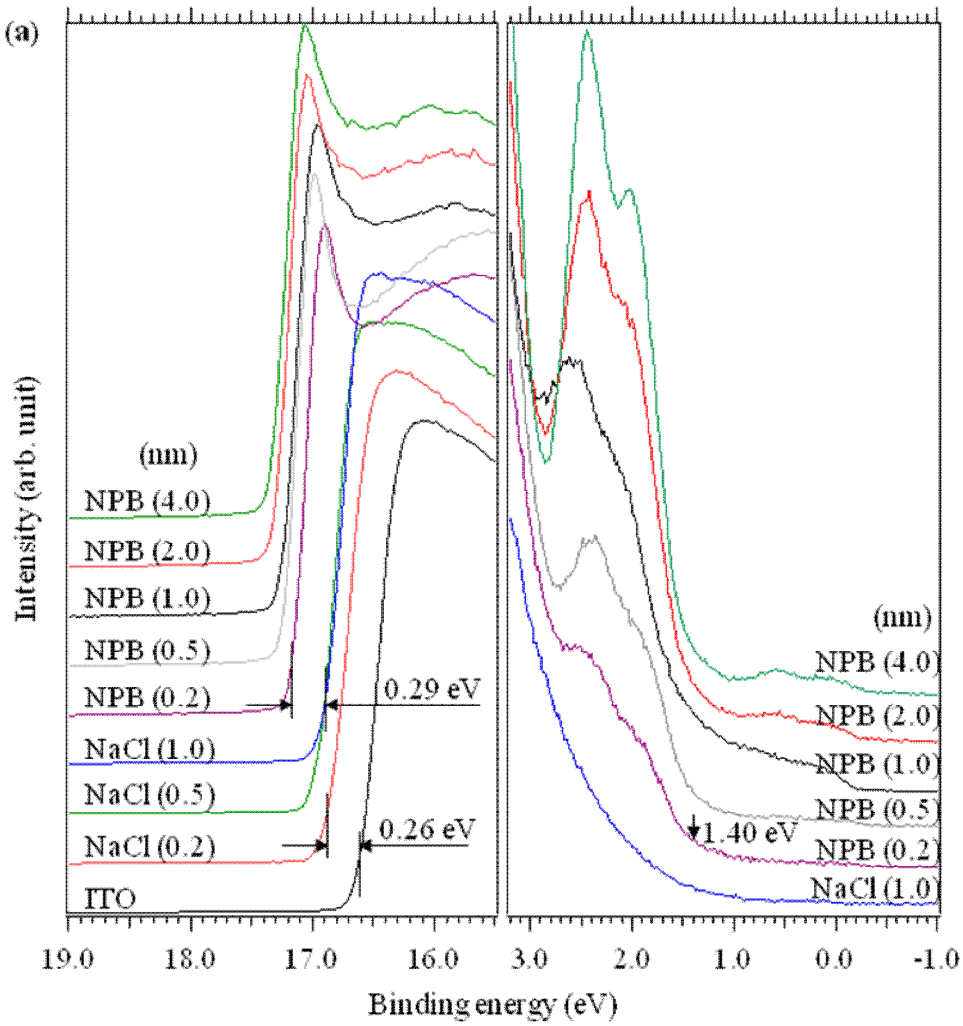

FIG. 4-3(a). UPS spectra collected near the Fermi level and secondary cutoff region during the step-by-step layer deposition of NaCl, followed by NPB, on the ITO substrate.

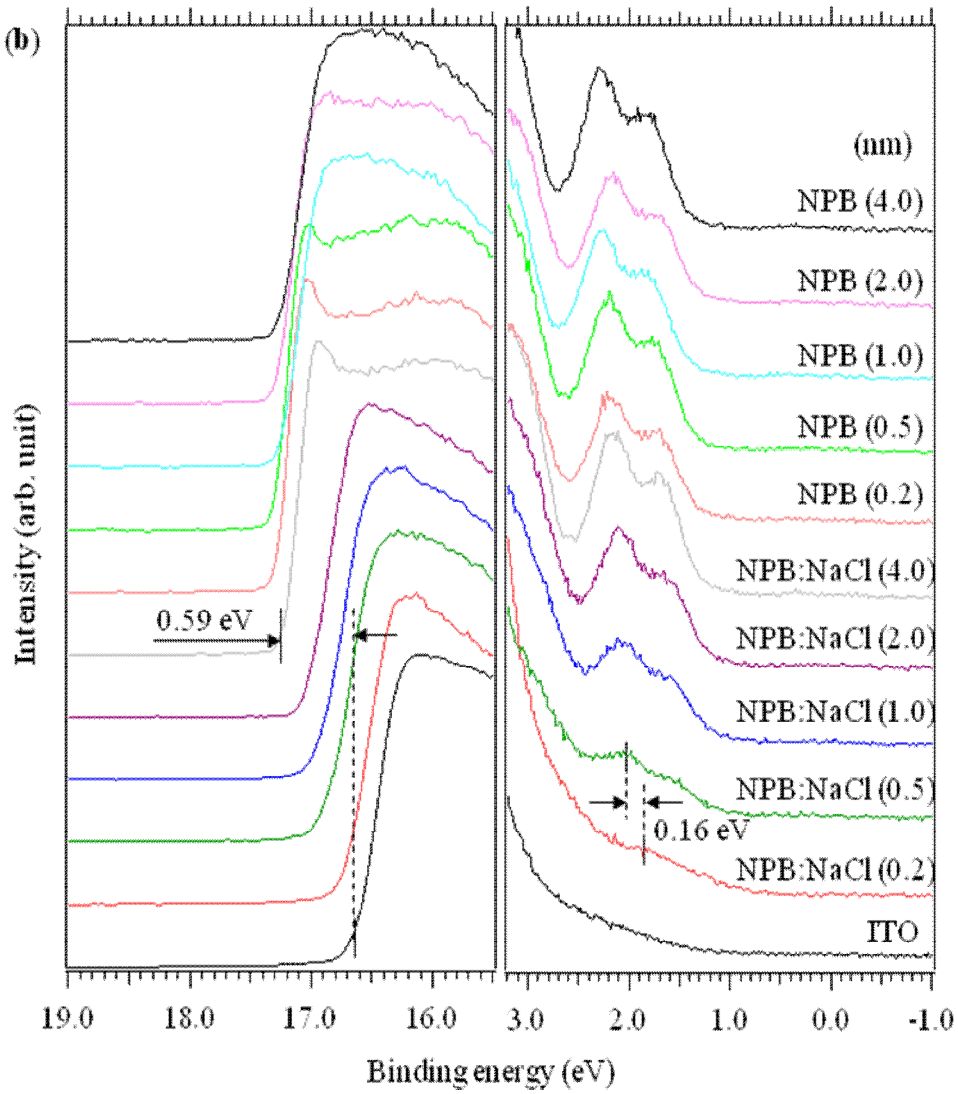

FIG. 4-3(b). UPS spectra collected near the Fermi level and secondary cutoff region during the step-by-step layer deposition of NPB:NaCl, followed by NPB, on the ITO substrate.

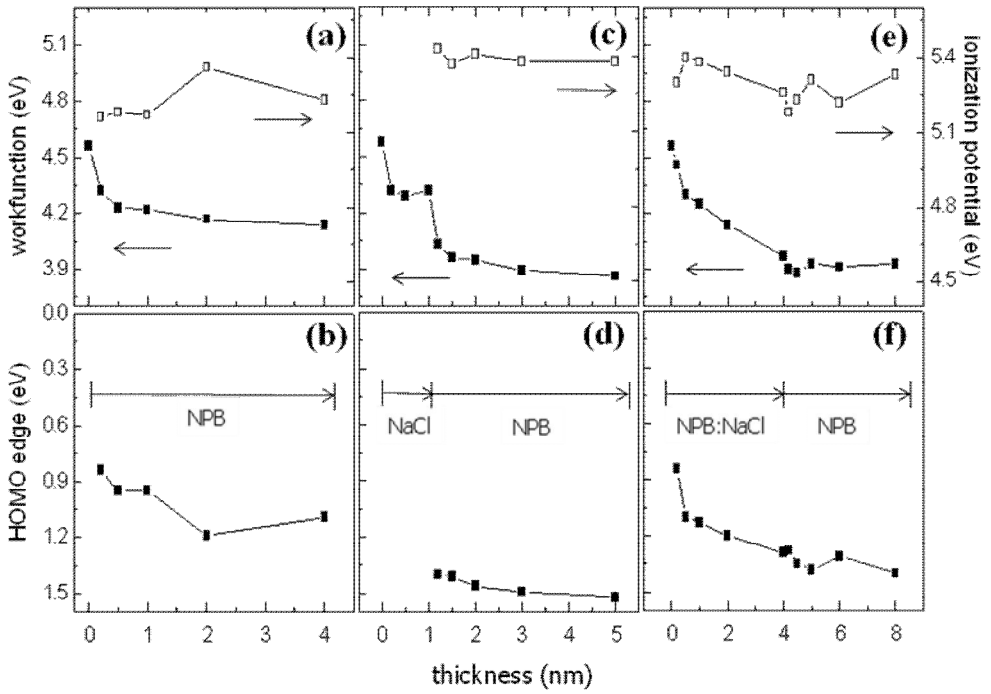

FIG. 4-4. Changes of workfunction and ionization potential versus NPB (a), NPB/NaCl (b), and NPB:NaCl composite (c) layer thickness, respectively. HOMO edge shifts in the NPB (b), NPB/NaCl (d), and NPB:NaCl composite, respectively.

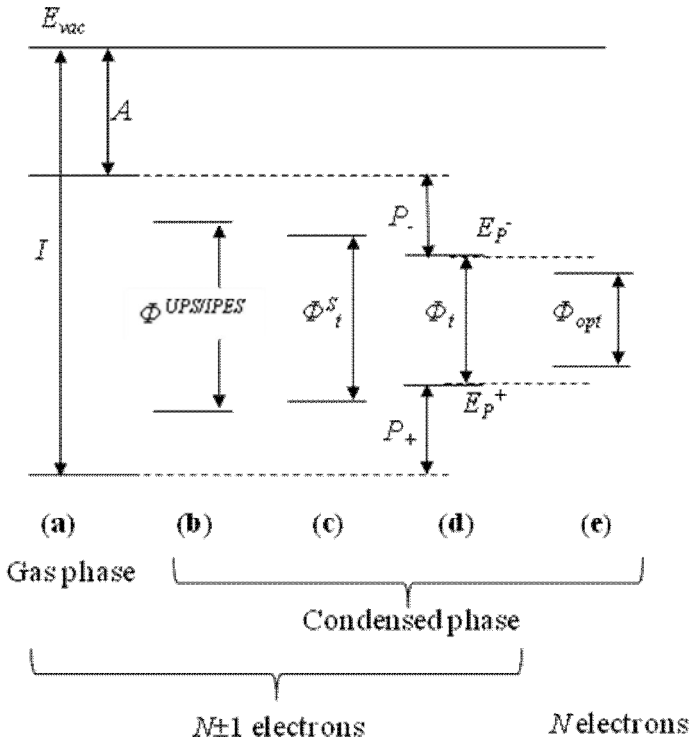

FIG. 4-5. Schematic energy diagram of (a) the adiabatic ionization energy and electron affinity (possible in the gas-phase molecule), (b) HOMO-LUMO gap measured with UPS/IPES (a distance between the centroids of the HOMO and LUMO peaks), (c) surface transport gap, (d) (bulk) transport gap, and (e) optical gap for the neutral excited molecule. P_- and P_+ denote the polarization energy during the generation of negative and positive polarons, respectively. E_{vac}, E_p^- and E_p^+ correspond to the vacuum level, negative polaron level, and positive polaron level, respectively.

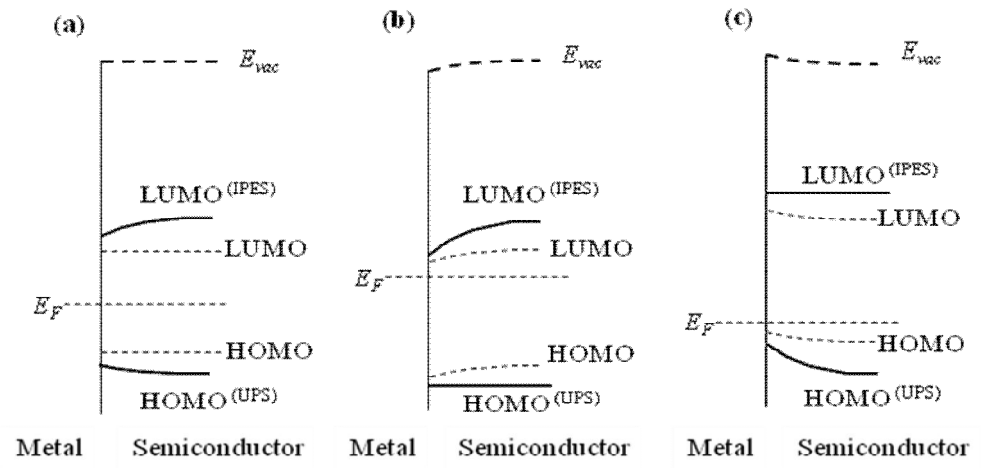

FIG. 4-6. Variation of the polarization from the interface of metal/semiconductor to the film surface because of image charges of the metallic substrate during the photoionization process; (a) when only the image charge is effective, and when the ground-state (b) LUMO- and (c) HOMO-derived levels are pinned near the Fermi level of the metal by charge transfer. E_{vac} and E_F correspond to the vacuum level, and Fermi level, respectively. Measurable energy levels by UPS/IPES are represented by broad solid lines, and broad dashed lines (vacuum levels). HOMO$^{(UPS)}$ and LUMO$^{(IPES)}$ represent final states of N–1 and N+1 electrons, respectively, which would be achieved from onsets of the obtained spectra. HOMO and LUMO levels represent ground states of N electrons (dashed lines).

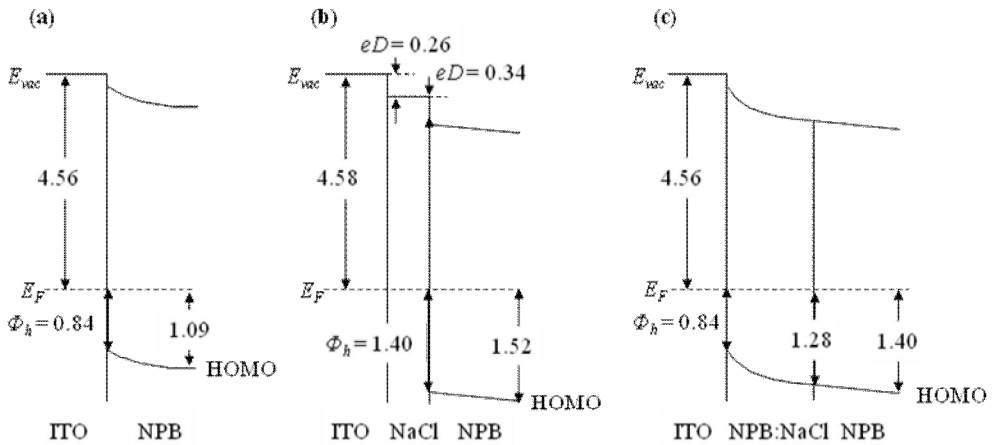

FIG. 4-7. Energy level diagram of the (a) NPB/ITO, (b) NPB/NaCl/ITO, and (c) NPB/NPB:NaCl/ITO. E_{vac}, E_F, eD, and Φ_h correspond to the vacuum level, Fermi level, interface dipole, and hole injection barrier, respectively.

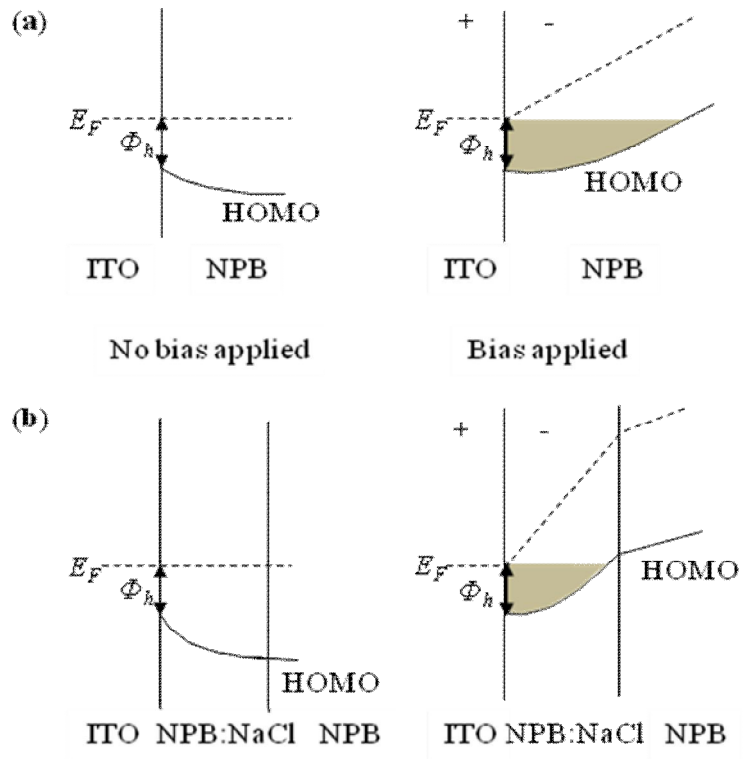

FIG. 4-8. Schematic band diagram: (a) without and (b) with the NPB:NaCl buffer layer. Energy level changes with an applied bias are shown in the left part of the diagram. The shaded area denotes the approximate tunnelling barriers under the bias voltage.

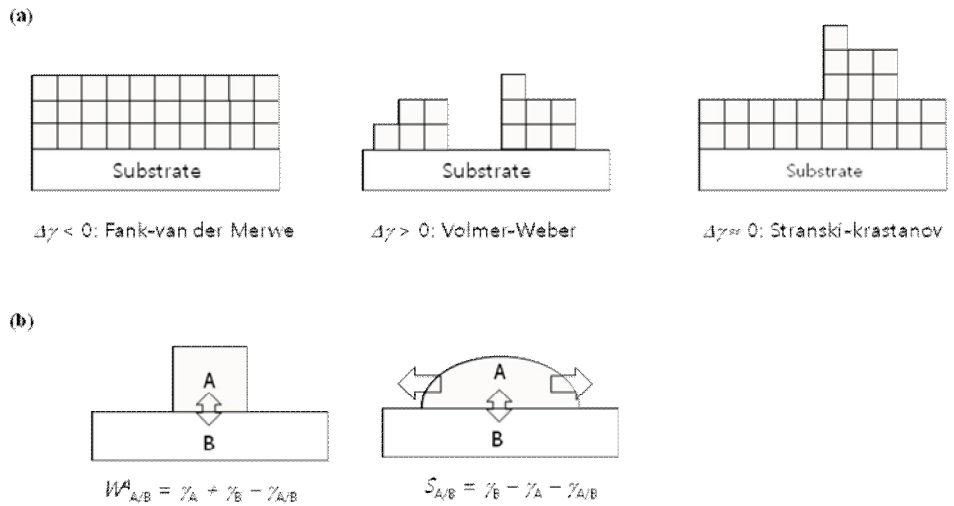

FIG. 4-9. Schematic illustrations of (a) the film growth modes on the uniform surface free energy. A qualitative criterion for the growth modes is denoted with $\Delta\gamma$ ($\Delta\gamma = \gamma_{AB} + \gamma_A - \gamma_B$, where $\gamma_{A/B}$ is the interfacial free energy of A/B interface, γ_A is the surface free energy of adsorbate A, and γ_B is the surface free energy of substrate surface B), and (b) the work of adhesion ($W^A_{A/B}$) and spreading coefficient ($S_{A/B}$) of A on surface B.

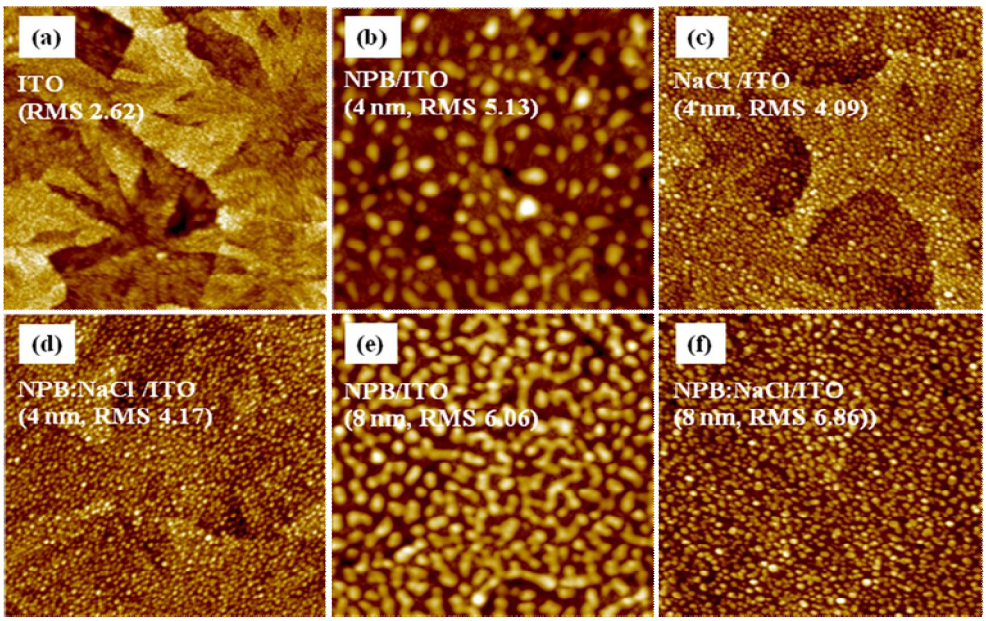

FIG. 4-10. AFM images ($2 \times 2\ \mu m^2$) of (a) the bare ITO, and the 4 nm thickness of (b) NPB, (c) NaCl, and (d) NPB:NaCl , and the 8 nm thickness of (e) NPB, and (f) NPB:NaCl. The thin films were deposited on the O_2 plasma pretreated-ITO surfaces. Root-mean-square roughness (RMS) values in nm are 2.62, 5.13, 4.09, 4.17, 6.06, and 6.86 for (a), (b), (c), (d), (e), and (f), respectively.

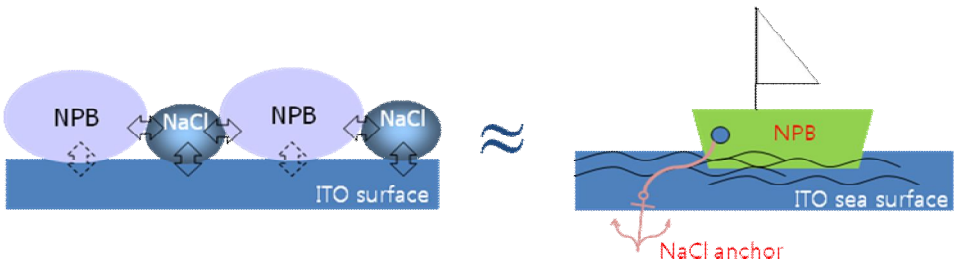

FIG. 4-11. Schematic diagram of the wetting mechanism, and its analogy with an anchored boat.

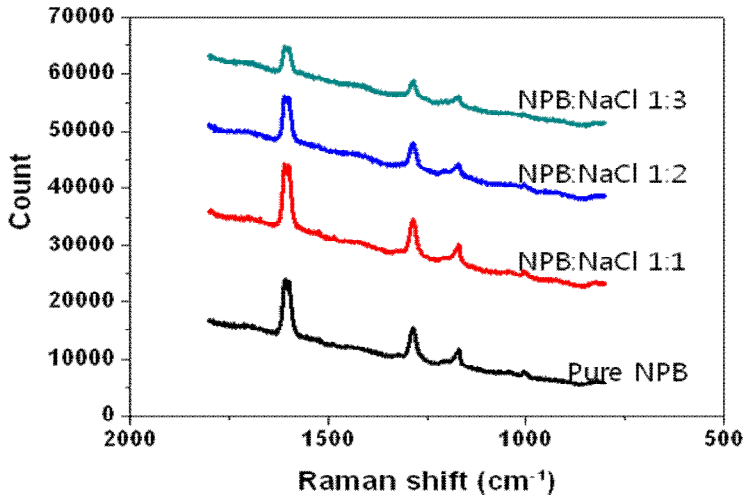

FIG. 4-12. Raman spectra of the pure NPB film (50 nm) and NPB:NaCl composite thin films (100 nm, 1:x v/v, x = 1, 2, and 3) on the ITO substrates.

TABLE IV-1. Calculated values of the interfacial free energy ($\gamma_{A/B}$), work of adhesion ($W^A_{A/B}$), and spreading coefficient ($S_{A/B}$) in mJ/m^2. Each surface free energy of NPB, NaCl, and ITO is referenced from literature, 31.1, 227, and 70.1 mJ/m^2, respectively [54-56].

A/B	$\gamma_{A/B}$	$W^A_{A/B}$	$S_{A/B}$
NPB/ITO	7.82	93.4	31.2
NaCl/IT	44.9	252	–202
NPB/Na	90.1	168	106

Bibliography

Papers

1. Walsdorff, C.; Park, S.; Kim, J.; Heo, J.; Park, K.; Oh, J.; Kim, K.*, Co-ordination chemistry of Cu^{I} with 1,3,5-tris[bis(pyridine-2-ylmethyl)aminomethyl]-2,4,6-triethylbenzene, a conformationally constrained trinucleating ligand, *J. Chem. Soc., Dalton Trans.*, **1999**, 923.
2. Jon, S. Y.; Kim, J.; Kim, M.; Park, S.-H.; Jeon, W. S.; Heo, J.; Kim, K.*; A Rational Designed NH_4^+ Receptor Based on Cation-π Interaction and Hydrogen Bonding, *Angew. Chem. Int. Ed.* **2001**, *40*, 2116.
3. Kim, K. J.*; Kim, H. K.; Moon, D.W.; Hong, T. E.; Jung, C. S.; Kim, L. K.; Kim, J. N.; Lim, C. H.; J. Kim, RRT Study for the Quantitative Analysis of Boron in Silicon, *J. Kor. Vac. Soc.* **2002**, *11*, 218.
4. Kwon, S-K*; Kim, J.; Moon, S.-K.; Kim, H.-H.; Park, K.-H.; Cho, Y.-J.; Kim, S.-T.; Lee, K.-R., Reconstruction characteristics of MgO (111) textured protective layer by over-frequency accelerated discharge in AC plasma display panel, *IDW '07 - Proceedings of the 14th International Display Workshops*, **2007**, *2*, 791.
5. Kwon, S.-K.*; Kim, J.; Moon, S.-K.; Park, K.-H.; Han, S.-S.; Choi, J.-K.; Kim, H.-H.; Kim, S.-T., Reconstruction characteristics of MgO (111) textured protective layer by over-frequency accelerated discharge in ACPDPs, *Digest of Technical Papers - SID International Symposium*, **2008**, *39*, 279.

6. Kwon, S-K*; Kim, J.; Moon, S-K; Choi, J-K; Park, K-H; Han, S-S, Influence of silicon and seed particles on the reconstruction characteristics and exaggerated grain growth of MgO protective layer by over-frequency accelerated discharge in ACPDPs, *Proceedings of International Meeting on Information Display*, **2008**, *8*, 957.
7. Kim, J.*; Kim, T.-H.; Oh, J.-G.; Noh, S. H.; Lee, J.-S.; Park, K.-H.; Ha, S.; Kang, H., Characterization of Acetylene Plasma-Polymer Films: Recovery of Surface Hydrophobicity by Aging, *Bull. Korean Chem. Soc.* **2009**, *30*, 2589.
8. Kim, J.*; Kim, M.; Kim, J. W.*; Yi, Y.; Kang, H., Organic light emitting diodes using NaCl:NPB composite as a hole injection buffer layer, *J. Appl. Phys.* **2010**, *108*, 103703.
9. Kim, J.*; Yi, Y.; Kim, J. W.*; Noh, S. H.; Kang, H., Interfacial energetics of NaCl-organic composite layer at OLED anode, *J. Phys. D: Appl. Phys.* **2012**, *45*, 455304.
10. Kim, J.; Kang, H.; Huh, S. H.*; Choi, S.-H.; Hong, Y. W.; Riu, D.-H., Scalable Energetic Impact Deposition for CNT-Ag Nanocomposite Film, *J. Korean Phys. Soc.* **2013**, *62*, 980.

Patents

1. Moon, S.-J.; Kim, J.; Kim, H.-H.; Lee, J.-S., Wire Bonding Method, KR 2003-0015110 (0587296).

2. Kim, J.; Lee, J.-S.; Kim, T.-H.; Kwon, H.-J.; Kim, M.; Oh, H.-Y., Method for thin film thickness gauge using Atomic Force Microscope tip-scratch in organic Electro-Luminescence device, KR 2003-0017489 (2004-0082805).
3. Yoon, S.-S.; Son, J.-H.; Kim, J.; Choi, J.-H.; Choi, Y.-H., Method for manufacturing organic thin film transistor and Method for manufacturing source/drain electrode of transistor, KR 2004-0059862 (0632525).
4. Yoon, S.-S.; Son, J.-H.; Kim, J.; Choi, J.-H.; Choi, Y.-H., Organic Thin Film Transistor for Gate Oxide using HfAlO, KR 2004-0069662 (2006-0020934).
5. Kim, J.; Yoon, S.-S.; Son, J.-H., Organic Thin Film Transistor element manufacturing method using dip-pen, KR 2005-0009169 (0656998).
6. Choi, J.-H.; Yoon, S.-S.; Son, J.-H.; Kim, J.; Choi, Y.-H., Organic Thin Film Transistor Having 3D Active Layer and Fabrication Method thereof, KR 2005-0010848 (2006-0090020).
7. Kim, J.; Choi, J.-H.; Choi, Y.-H., Organic Thin Film Transistor having a surface modifying layer and manufacturing method thereof, KR 2005-0015435 (0668615).
8. Choi, Y.-H.; Kim, J.; Lee, B.-S.; Yoon, S.-S., Method for fabricating light emitting device, KR 2005-0059423 (0692089).
9. Kim, J.; Yoon, S.-S.; Son, J.-H.; Choi, J.-H., Stamp for contact printing and contact printing method using the same, KR 2005-0060946 (2007-0005421).
10. Yoon, S.-S.; Son, J.-H.; Kim, J.; Choi, J.-H.; Seong, M.-C.; Kim, C.-N.; Kim, S.-T., Organic Thin Film Transistor and method for preparing the same, KR 2005-0063933 (0718960).

11. Kim, J.; Yoon, S.-S.; Choi, J.-H.; Son, J.-H.; Kim, H.-J., Method for Fabricating Organic Thin Film Transistor, KR 2005-0094267 (0652339).
12. Kim, J.; Yoon, S.-S.; Kim, H.-J.; Son, J.-H.; Choi, Flexible display device, KR 2005-0096306 (0667569).
13. Kim, J.; Yoon, S.-S.; Jo, W.-K., Flexible display device and method for preparing the same (II), KR 2005-0096307 (1187755).
14. Kim, J.; Yoon, S.-S.; Jo, W.-K., Flexible display device and method for preparing the same (I), KR 2005-0096308 (1158817).
15. Kim, J.; Yoon, S.-S.; Son, J.-H.; Choi, J.-H.; Kim, H.-J., Method for carrying out fine pattern, KR 2005-0113770 (2007-0055260).
16. Kim, J.; Yoon, S.-S.; Kim, H.-J.; Son, J.-H.; Choi, J.-H., Organic Thin Film Transistor and production method of Organic Thin Film Transistor, KR 2006-0054121 (2007-0119766).
17. Kim, J.; Park, K.-H., Passivation method of organic semiconductor, KR 2006-0080303 (1245421).
18. Kim, J.; Jang, S., Display and control method for display, KR 2010-0052613 (2011-0133082).
19. Kim, J.; Jang, S., Organic electroluminescent device and portable terminal having the same, KR 2011-0023064 (2012-0105319).
20. Kim, J.; Yoo, A.; Jang, S., Mobile terminal and method for manufacturing the same, KR 2011-0023704 (2012-0105953).
21. Kim, J.; Yoo, A.; Jang, S., Mobile terminal and method for manufacturing the same, EP 2500126.

22. Kim, J.; Yoo, A.; Jang, S., Mobile terminal and method for manufacturing the same, US 2012-0236587.

23. Kim, J. et al. Mobile terminal, KR 2011-0027756 (2012-0109913).

24. Kim, J. et al. Mobile terminal, US 8504113.

25. Kim, J.; Jang. S.; Yoo, K., Display mobile and mobile terminal having the same, KR 2011-0049183 (1279515).

26. Kim, J.; Jang. S.; Yoo, K., Display mobile and mobile terminal having the same, US 2012-0300142.

27. Kim, J.; Jang. S.; Yoo, A., Mobile terminal, KR 2011-0066632 (1221921).

28. Kim, J.; Jang. S.; Yoo, A., Mobile terminal, EP 2544032.

29. Kim, J.; Jang. S.; Yoo, A., Mobile terminal, US 2013-0009180.

요약 (국문초록)

유기 발광 소자의 실질적 응용을 위해서는 다른 전자 소자와 마찬가지로, 소비전력 절감과 수명향상이 매우 중요하다. 소비전력은 수명향상과 밀접한 관계를 갖고 있다. 본 학위 논문은, 인듐주석 산화물 산화전극 (“+” 전극)과 유기물 계면에서 생기는 정공 주입 퍼텐셜 장벽을 낮추어 유기 발광 소자의 구동 전압을 낮추고, 수명을 향상할 수 있는 새로운 정공 주입층의 도입과 그 메커니즘에 대하여 다루었다. 주로 환원전극에 도입되고 있는 전자 주입 물질인 금속할로겐 화합물을 산화전극에 도입하여 효율과 수명을 동시에 향상시킨 연구로서, 소자 설계 및 제작의 간소화와 함께 다양한 할로겐 화합물의 사용으로 확대될 수 있다.

1 장에서는 유기발광소자에 대한 기본적인 소자물리학을 기술하여, 이후 유기발광소자의 전기적 특성에 대한 이해를 돕고 있다. 또한 유기발광소자의 다양한 응용에 걸림돌이 되고 있는 전력효율과 소자열화에 대하여 언급하고, 전극/유기물 계면 엔지니어링을 통한 전력효율과 수명 개선에 대하여, 기존 연구결과를 기술함으로써, 본 연구의 중요성을 밝힌다.

2 장에서는 유기발광소자의 산화전극인 인듐주석 산화물 전극의 표면처리에서 가장 많이 사용되고 있는 자외선-오존법과 산소 플라즈마법에 대하여, 각각의 표면처리에 따른 유기발광소자의 특성 차이를 비교하였다. 인듐주석 산화물을 자외선-오존법으로 표면 처리하였을 때, 산소 플라즈마로

표면 처리할 때와는 달리, 인듐주석 산화물의 성분인 주석의 이탈이 관찰된다. 주석의 이탈은 인듐주석 산화물 전극 표면의 일함수와 표면저항의 증가를 암시하며, 유기발광소자의 구동전압을 낮추는 효과로 귀결된다. 일반적으로 구동전압 저하는 소자 수명을 향상시키는 경향이 있지만, 본 실험에서는, 구동전압이 높은 소자 (산소 플라즈마 처리를 처리한 인듐주석 산화물 산화전극) 의 수명이 더 길었다. 이는 본 실험의 유기발광 소자가 정공 과다 소자로서, 발광층에서 전하 균형이 심하게 깨어진다는 것이 하나의 요인으로 판단된다.

3 장에서는 정공주입층으로 염화나트륨과 유기물의 복합체를 도입함으로써, 유기발광소자의 구동전압이 낮아 지고, 수명도 향상됨을 보이고 있다. 상기 복합체의 특정 두께 및 특정 구동 전압 조건에서, 조성에 대한 구동 전류 변화를 관찰해 보면, 두 군데 조성에서 전류의 상승 (봉우리)이 나타나는 데, 이는 정공 주입 퍼텐셜 장벽이 낮아 지는 요인이 두 가지 이상임을 암시하고 있다.

4 장에서는 정공 전달 (또는 정공주입) 유기물질과 염화나트륨의 복합체 완충층이 정공 주입 효율과 소자 수명향상을 시킬 수 있는 근거를 자외선 광전자 분광분석과 원자력 탐침 현미경을 이용하여 밝히고 있다. 순수한 염화나트륨 완충층은 높은 정공 주입 퍼텐셜 장벽 (1.40 eV)을 보이는 반면, 정공전달 (또는 정공주입) 유기물과 염화나트륨의 복합체로 구성된 완충층은, 퍼텐셜 장벽이 완충층을 도입하지 않았을 때의 수준인 0.84 eV 까지 낮아졌다. 염화나트륨의 절연특성을 고려할 때, 소자 구동 시 걸리는

정 방향 전압에 대하여, 정공 주입 터널링 장벽이 완충층을 도입하지 않은 경우에 비하여, 더 낮아 짐을 유추할 수 있다. 또한, 정공주입층의 박막성장과정에서, 염화나트륨이 도입됨으로써 유기물간의 응집에 의한 전극/유기물 계면 접착력 약화를 방지하는 것이 관찰되었다. 접착력과 퍼짐 계수를 계산해 본 결과, 염화나트륨은 인듐주석 산화물 산화전극과 매우 강하게 접착하면서 (252 mJ/m^2) 퍼짐성은 매우 낮았고, 인접한 정공주입유기물과 상당한 접착력(168 mJ/m^2)을 갖고 있음을 알 수 있었다. 이는 염화나트륨이, 덩치가 비교적 큰 정공주입 유기물 분자가 상기 산화전극에 잘 접착할 수 있도록 일종의 닻 (앵커)과 같은 역할을 하는 것으로 사료된다. 이러한 유기물/전극 계면 접착력 향상이 정공 주입 효율과 소자 수명향상의 또 다른 원인임을 알 수 있다.

주요어: 유기발광다이오드, 염화나트륨:유기물 복합체, 정공 주입 효율, 소자 수명, 광전자 분광분석, 젖음성

학 번: 2007-30765

Acknowledge (감사의 글)

기나긴 많은 시간이 지난 것 같은 데, 돌아 보니, 이 학위 과정을 시작하던 때가 엊그제처럼 다가옵니다. 배움의 기회가 다시는 오지 않겠지 하던 때에, 가까운 사람들의 격려와 함께 주경야독의 길을 시작하게 되었습니다. 지금까지의 과정에서, 많은 분이 베풀어 주신 관심과 사랑과 도움이 얼마나 큰 힘이 되었는지 모릅니다.

지도교수님이신 강헌 교수님께서는 저의 여러 여건을 잘 포용해 주셨고, 찾아 뵐 때면, 언제나 충분한 시간을 할애하시며, 조언을 아끼지 않으셨습니다. 처음 학술지 논문원고를 섰을 때, 세 번에 걸친 세세한 교정과 논문지도를 해주셨는데, 그때의 귀한 가르침은, 제가 이후의 학술 논문원고를 작성하는 데, 시금석이 되었습니다. 본 학위논문의 원고를 검토하시고 발표 내용을 경청하시며, 다양한 질문으로 심사를 해 주신 김관 교수님, 서정쌍 교수님, 장두전 교수님, 김정원 박사님께 감사를 드립니다. 심사가 통과된 후에는 진심 어린 축하와 격려로 반겨 주셨습니다. 공의와 사랑의 하나님께서 함께 하신 것을 경험하는 감사의 시간이었습니다.

본 논문의 실험 결과물들 중, OLED 소자 제작과 전기적 특성 실험 결과는, LG Display Co.의 김명섭 박사님의 도움이 있었기에 가능하였습니다. 회사의 제약된 여건 속에서도 물심양면으로 애써주신 김명섭 박사님께 감사 드립니다. PES 실험은 KRISS 의 김정원 박사님의 전폭적인 지원으로 이루어

졌습니다. 특히, 김정원 박사님께서는 본 학위 과정 속의 오랜 시간을 함께 하시면서, 제가 편하게 실험할 수 있도록 제반 여건을 조성해 주셨고, 논문지도를 해 주셨습니다. 특별한 감사의 마음을 전하고 싶습니다. PES data 처리와 해석에 관한 자유로운 토론으로 많은 가르침을 주신 이연진 박사님께 또한 감사 드립니다.

회사에 몸 담고 있으면서 이 학위 과정을 밟을 수 있도록, 허락해 주신 당시의 팀장이셨던 박규호 수석님께 감사 드립니다. 그분의 배려가 있었기에, 시간적으로 부담이 많이 될 수 있는 course work 을 잘 마칠 수 있었습니다.

기도가운데 시작하였던 이 과정에서, 작고 보잘것없는 자를 오래 기다리시고, 풍성히 채우시며, 인도해 주신 하나님아버지께 감사 드립니다. 많은 믿음의 형제님들의 기도가 함께 하였습니다. 김명섭 형제님, 주차흠 형제님, 김설섭 형제님, 이영민 형제님, 김현성 형제님, 유용택 형제님을 비롯한 네비게이토 선교회의 많은 형제님들의 기도가 있었음을 알고 있습니다. 이 기도가 저를 지탱시켜 주었습니다.

싸늘한 고독 속에서도 크고 작은 기쁨과 잔잔한 평안을 누리게 해 준 사랑하는 아내와 아들 유찬에게 고마움을 전합니다. 수업 받으러 또는 논문 쓰러 다니던 중, 캠퍼스의 푸른 잔디와 하얀 눈을 바라보며, 아내가 싸준 도시락을 먹던 시절이 아름다운 기억으로 남았습니다. 시골에 계신 아버지의 사랑이 늘 생각납니다. 학위 심사 통과 소식을 들으시고, “고맙다” 라는 한 마디의 말씀이 마음을 저리게 합니다.

연로하신 아버지를 생각하고, 어린 아들을 바라보며, 하나님아버지의 사랑을 다시 생각하게 됩니다.

“하나님이 세상을 이처럼 사랑하사 독생자를 주셨으니 이는 저를 믿는 자마다 멸망치 않고 영생을 얻게 하려 하심이니라.”

(요한복음 3 장 16 절)

도움을 주신 모든 분들께 다시 한번 감사 드리며, 하나님의 사랑과 예수그리스도의 은혜가 함께 하시고, 주님의 평강이 가득하길 기도 드립니다.